

Clemson University

**TigerPrints**

---

All Dissertations

Dissertations

---

8-2022

## Subwavelength Engineering of Silicon Photonic Waveguides

Farhan Bin Tarik  
fbintar@clemson.edu

Follow this and additional works at: [https://tigerprints.clemson.edu/all\\_dissertations](https://tigerprints.clemson.edu/all_dissertations)



Part of the [Electromagnetics and Photonics Commons](#), [Nanoscience and Nanotechnology Commons](#), [Nanotechnology Fabrication Commons](#), [Optics Commons](#), and the [Semiconductor and Optical Materials Commons](#)

---

### Recommended Citation

Bin Tarik, Farhan, "Subwavelength Engineering of Silicon Photonic Waveguides" (2022). *All Dissertations*. 3137.

[https://tigerprints.clemson.edu/all\\_dissertations/3137](https://tigerprints.clemson.edu/all_dissertations/3137)

This Dissertation is brought to you for free and open access by the Dissertations at TigerPrints. It has been accepted for inclusion in All Dissertations by an authorized administrator of TigerPrints. For more information, please contact [kokeefe@clemson.edu](mailto:kokeefe@clemson.edu).

# SUBWAVELENGTH ENGINEERING OF SILICON PHOTONIC WAVEGUIDES

---

A Dissertation  
Presented to  
The Graduate School of  
Clemson University

---

In Partial Fulfillment  
of the Requirements for the Degree  
Doctor of Philosophy  
Photonic Sciences and Technology

---

By  
Farhan Bin Tarik  
August 2022

---

Accepted by:  
Dr. Judson Douglas Ryckman, Committee Chair  
Dr. Hai Xiao  
Dr. William Rod Harrell  
Dr. Apparao Rao

## ABSTRACT

The dissertation demonstrates subwavelength engineering of silicon photonic waveguides in the form of two different structures or avenues: (i) a novel ultra-low mode area v-groove waveguide to enhance light-matter interaction; and (ii) a nanoscale sidewall crystalline grating performed as physical unclonable function to achieve hardware and information security.

With the advancement of modern technology and modern supply chain throughout the globe, silicon photonics is set to lead the global semiconductor foundries, thanks to its abundance in nature and a mature and well-established industry. Since, the silicon waveguide is the heart of silicon photonics, it can be considered as the core building block of modern integrated photonic systems. Subwavelength structuring of silicon waveguides shows immense promise in a variety of field of study, such as, tailoring electromagnetic near fields, enhancing light-matter interactions, engineering anisotropy and effective medium effects, modal and dispersion engineering, nanoscale sensitivity etc. In this work, we are going to exploit the boundary conditions of modern silicon photonics through subwavelength engineering by means of novel ultra-low mode area v-groove waveguide to answer long-lasting challenges, such as, fabrication of such sophisticated structure while ensuring efficient coupling of light between dissimilar modes. Moreover, physical unclonable function derived from our nanoscale sidewall crystalline gratings should give us a fast and reliable optical security solution with improved information density. This research should enable new avenues of subwavelength engineered silicon photonic waveguide and answer to many unsolved questions of silicon photonics foundries.

*To*

*Ammu, Pappa, Tultul and Mitul*

## ACKNOWLEDGEMENTS

I am thankful to Almighty for giving me the opportunity, capability and patience to perform and complete my Ph.D. research and my parents for all the love and inspiration. My mom, my dad, and my sister have always believed in me and constantly supported and motivated me throughout the way to navigate me where I am right now.

This dissertation would not be complete without expressing my sincere gratitude to Dr. Judson Douglas Ryckman, my committee chair and graduate advisor. Ph.D. advisers probably plays the most important role on their graduate students' lives. I am so lucky to have an adviser who cares about our mental health even more than that he cares about ourselves. From the bottom of my heart, I express my utmost gratefulness to Dr. Ryckman for seeing something in me, taking me in his vibrant research group and supporting with all the necessary resources. It will not be an exaggeration to state that without his generous supervision, meticulous scrutiny, scholarly advice and continuous encouragement, this body of work would not exist.

My colleagues at Ryckman group have been phenomenal over-the-years. I would like to show my appreciation to my colleagues Tahmid Hassan Talukdar, Nazmus Sakib, Saddam Gafsi, Cody Nelson, Anna Hardison, Derrick Joyce Jr., Nithesh Kumar and Matthew Panipinto for their invaluable insight, collaboration and assistance. Tahmid has always been a good friend of mine and helped with his expertise whenever I needed him with anything. Nazmus performed the initial research on v-groove waveguides which I carried later to give it a final shape. The mask design of the anapole structures was done by Cody and Saddam ran most of the simulations using my experimental data. Anna assisted me a lot in testing the v-groove

waveguides. Derrick built the initial setup for testing the active PUFs. I am extremely blessed to be a part of this extra-ordinary research group.

I would like to thank my co-authors Azadeh Family and Dr. Yingjie Lao for their kind collaboration in the silicon photonic physical unclonable function project. Azadeh evaluated the one of the analysis techniques with inputs from Dr. Lao and Dr. Ryckman. While talking about this particular project, I should also acknowledge the edX UBCx Phot1x Silicon Photonics Design, Fabrication and Data Analysis course organized and operated by Dr. Lucas Chrostowski and Iman Taghavi, which is supported by the Natural Sciences and Engineering Research Council of Canada (NSERC) Silicon Electronic-Photonic Integrated Circuits (SiEPIC) Program. The devices were fabricated by Richard Bojko at the University of Washington Nanofabrication Facility (WNF) part of the National Science Foundation's National Nanotechnology Infrastructure Network (NNIN), and C. Horvath at Applied Nanotools, Inc. Semi-automated measurements were done by Hosham Shoman at the University of British Columbia (UBC). My whole Ph.D. research was supported by the Air Force Office of Scientific Research (AFOSR) Young Investigator Research Program (Award # FA9550-19-1-0057, program officer: G. Pomrenke) and start-up funds from Clemson University.

I never ever felt out of my comfort zone at any point of my stay at Clemson University, and the credit goes to a highly jovial and friendly Bangladeshi Community that I am lucky to be a part of. I am really grateful to every single community member, especially, Dr. Abdullah Al Mamun, Esrat Jabin Oni, Tangia Alam Tammi and Dr. Shirajul Arefin Shibly, for making my graduate student life experience such a pleasant and memorable one. I would also like to mention the name of Mahabubur Rahman for once assisting me with Matlab when I needed.

Another individual to whom I owe a debt of gratitude is my friend Farzana Siddique Mitul. She has encouraged and supported me mentally and financially at so many occasions during my graduate studies. I am lucky to have astonishingly wonderful friends and relatives who keep cheering and inspiring me all the time.

Finally, I profusely thank my committee members Dr. Hai Xiao, Dr. William Harrell and Dr. Apparao Rao for their valuable insights and suggestions. My sincere gratitude to all the faculty members and staffs of Holcombe Department of Electrical and Computer Engineering and International Services at Clemson University for their kind support and co-operation throughout the study period.

## TABLE OF CONTENTS

	Page
TITLE PAGE .....	i
ABSTRACT.....	ii
DEDICATION .....	iii
ACKNOWLEDGMENTS .....	iv
LIST OF TABLES .....	ix
LIST OF FIGURES .....	x
 CHAPTER	
I. INTRODUCTION .....	1
1.1 Introduction to Silicon Photonic Waveguides .....	2
1.2 Introduction to Subwavelength Engineering .....	3
1.3 Motivation and Scope of Work.....	7
II. ENABLING NOVEL SUBDIFFRACTION V-GROOVE WAVEGUIDE	13
2.1 Introduction.....	13
2.2 Design Methodology.....	15
2.3 Performance Evaluation.....	19
2.4 Fabrication of V-groove Waveguide .....	24
2.5 Experimental Verification of V-groove Waveguides .....	27
2.6 Summary .....	28
III. REALIZING ROBUST OPTICAL PHYSICAL UNCLONABLE FUNCTION FROM QUASICRYSTAL INTERFEROMETER .....	33
3.1 Introduction.....	33
3.2 Approach Towards Robust Optical PUF .....	35
3.3 Modeling, Fabrication and Measurement .....	44
3.4 The QCI PUF .....	45
3.5 Results and Discussion .....	50
3.6 Simulation/Analysis of a QCI PUF Over Temperature .....	59
3.7 Summary .....	62



Table of Contents (Continued)	Page
IV. SCALABLE AND CMOS COMPATIBLE HARDWARE AUTHENTICATION OF 56 QCI PUFs .....	71
4.1 Introduction.....	71
4.2 Foreground.....	72
4.3 Approach.....	73
4.4 Methods.....	75
4.5 Results and Analysis .....	77
4.6 Conclusion .....	86
V. ELECTRICALLY RECONFIGURABLE PUF BASED ON MOIRÉ QCI	90
5.1 Introduction.....	90
5.2 Approach.....	90
5.3 Device Fabrication .....	91
5.4 Instrumentation and Measurement Technique.....	92
5.5 Results and Analysis .....	94
5.6 Outlook .....	97
VI. SUMMARY AND OUTLOOK.....	99
APPENDICES .....	105
A: V-groove Design and Modelling .....	105
B: QCI PUF Design.....	107

References are added at the end of each chapter

## LIST OF TABLES

Table	Page
3.1 Example PUF features extracted from a five-level Fejer-Korovkin wavelet decomposition.....	59
3.2 Results of feature extraction and correlation analysis to device identification. The “unclonable” QCI PUFs achieve substantial inter-chip variations and are stable across different environmental conditions, while the inter-chip variations of the “clonable” design are not sufficient to identify the enrolled device .....	59
3.3 The variance of “sim1” PUF’s output signals for each decomposition level.....	62
3.4 Mean squared error between enrolled signals and the other signals.....	62

## LIST OF FIGURES

Figure		Page
1.1	Schematic of slab (left), strip (middle), and rib (right) waveguides .....	2
1.2	TE mode in rib waveguide (left) and strip waveguide (right) .....	3
1.3	Schematic diagrams of various subwavelength structured strip and slab waveguides. (a) SWG waveguide, (b) 90° waveguide bend, and (c) multimode crossing based on the subwavelength metamaterial. The red, pink, and gray colors represent silicon, partially etched silicon, and silica, respectively. ‘b’ is reprinted from Wu et al. The structure in ‘c’ was reported in Xu and Shi .....	4
1.4	Schematic diagram of the fabrication process of subwavelength structured silicon photonic device .....	6
1.5	Avenues of this research: two different versions of subwavelength structuring of silicon photonic waveguides; (1) enabling novel ultra-low mode area v-groove waveguide, (2) developing physical unclonable function from silicon photonic quasicrystal interferometer ..	8
2.1	(a) Electric field mode profile of a silicon strip waveguide (350 nm x 220 nm) and (b) silicon V-groove waveguide with $h = 14$ nm cladded by SiO <sub>2</sub> (fundamental quasi-TE modes). (c) electric field energy density, $u_e = \frac{1}{2} \epsilon  E ^2$ , for the strip waveguide and (d) silicon V-groove waveguide normalized to the same color scale. Values above $1/6^{\text{th}}$ the max value, $u_{e,max}$ , are saturated to show detail. (e) Schematic of the evanescent coupling architecture and two prospective approaches: (f) non-adiabatic directional coupling, and (g) adiabatic mode evolution.....	15
2.2	Effective indices as a function of waveguide width for: (a) the strip waveguide, (b) centered V-groove waveguide, and (c) off-centered V-groove waveguide (centered only at $w_{\text{out}} = 600$ nm). Purple markers indicate phase matching design points, while green/red markers indicate taper start/end points. Dashed lines indicate higher order modes .....	16

## List of Figures (Continued)

Figure	Page
2.3 Visualization of the supermodes' electric field intensity and effective indices in the adiabatic mode evolution design, where: $w_{in} = 350$ nm, $w_{tip} = 200$ nm, $w_s = 500$ nm, $w_{out} = 600$ nm, and $g = 200$ nm. The strip waveguide supermode evolves into a V-groove waveguide supermode as the taper passes through an anticrossing. Higher order supermodes exhibit polarization rotation effects .....	18
2.4 Evaluation of the adiabatic mode evolution based design: coupling efficiency vs. coupler length for varying gaps.....	19
2.5 Simulated electric field $ E $ for: (a) directional coupler and (b) adiabatic mode evolution based example designs. The field profiles are taken at the plane $y = 15$ nm above the $\text{SiO}_2/\text{Si}$ interface Evaluation of the adiabatic mode evolution based design: coupling efficiency vs. coupler length for varying gaps .....	20
2.6 Simulated coupling efficiencies of adiabatic and directional coupler (DC) type devices vs. three key parameters: (a) silicon device layer thickness, (b) error in waveguide width $\Delta w$ and (b) error in V-groove bridge height $\Delta h$ (as depicted in Fig. 2.1(c)).....	22
2.7 Simulated wavelength dependence of nominal adiabatic and directional coupler (DC) type devices, and two illustrative examples of DCs with CD errors .....	23
2.8 Single layer process flow of “Diabolo” (left) and “V-groove” (right) structures.....	25
2.9 SEM Images of all-dielectric V-groove waveguides with different groove widths and heights attained from single layer fabrication process .....	27
2.10 SEM image of the waveguide in Fig. 2.9(c) from the other side.....	27
2.11 Experimental verification of waveguiding (top view and side view) for the v-groove waveguides shown in Fig. 2.9.....	28

## List of Figures (Continued)

Figure	Page
3.1	Conventional optical PUF structures: realized from random multiple-scattering and multimode fiber speckle.....35
3.2	High level overview. (A) A typical PUF authentication scheme, and overview of: (B) a conventional optical PUF, and (C) a robust optical PUF (the type introduced and demonstrated in this work). Here robustness refers to achieving immunity against probing and environmental variations .....37
3.3	Overview of photonic circuitry and quasicrystal interferometry. (A) Optical microscope image of the integrated silicon photonic QCI PUF architecture. Input/output grating couplers (GC1/GC2), single mode waveguides, and a 50:50 directional coupler (DC) enable pure mode filtering and stable QCI device measurement in transmission. A compact y-branch (YB) splits light into two symmetric arms, (1) and (2), routed to the spiral quasicrystal (QC) arms and loop mirrors (LM1/LM2). (B) Zoomed view of design and (C) SEM image of the curved QC and illustration of the $m$ th segment considered in device modelling (scale bar = 1 $\mu$ m). (D) Nominal QC effective index profile @ 1550 nm. (E) Example effective index profiles with random errors introduced, and (F) corresponding phase differences between the two arms. (G) Simulated QCI spectra (YB port reflectance) for nominal and random QCIs with varying disorder parameters, and (H) zoomed view of the same .....47
3.4	Experimental transmission spectra for triplicated silicon photonic (A) QCI PUFs, and (B) single etalon DBR integrated MGTIs. Black curve corresponds to single pass directional coupler (DC) transmission. Probing of QCIs and MGTIs adds ~3 dB insertion loss owing to double pass loss through the DC. Device 2/3 spectra are shifted on the y-axis for clarity. (C) Zoomed view of QCI PUF spectra showing device uniqueness. (D) Zoomed view of QCII spectra at both temperature settings, revealing a deterministic spectral shift .....52
3.5	(a) Spiral and (b) straight waveguide loss determination via the cutback method .....54
3.6	Hamming distance authentication analysis for each silicon photonic

	QCI PUF at two temperature settings .....	55
3.7	Five-level decomposition of an output signal analyzed by Fejer-Korovkin wavelets. After decomposition, the devices can be distinguished effectively .....	57
3.8	(a) Simulated PUF spectra over +/- 30 °C temperature variation, (b) zoomed view which clearly shows all spectral features in wavelength shift together thereby retaining the overall PUF signature. Spectra are off-set on y-axis by 40 dB for clarity. (c) Simple Hamming analysis of binarized PUF spectra as a function of binary key shift. While not as robust as our signature analysis (Table 3.1), this Hamming analysis is able support device authentication.....	61
4.1	QCI PUF architecture and authentication framework: post-processing technique is shown involving conversion of spectral response to binary sequence, followed by binary cross correlation analysis to achieve proper authentication .....	74
4.2	Digital keys and cross-correlation analysis. Visualization of a 150 bit subset of the binary keys generated from all 56 PUFs extracted from measurements at (a) 25°C and (b) 30°C; the red arrow indicates the 70 bit lag observed due to the spectral shift over temperature. (c) Cross-correlation analysis depicting the normalized correlation coefficient between the enrolled PUF at 30°C and test PUF at 25°C vs. lag for selected PUFs 1-3. (d) Example cross-correlation analysis of enrolled PUF 14 vs. all 56 test PUFs verifying the uniqueness and authenticity of the enrolled device .....	78
4.3	Measured spectra shown after baseline correction for all 56 PUFs. (PUF1 in top left corner and PUF 56 in bottom right corner) .....	81
4.4	(a) Correlation-based authentication with $k = 5$ , (b) HD based authentication with $k = 5$ , (c) correlation-based authentication with $k = 3$ , (d) HD based authentication with $k = 3$ . Cumulative distribution functions indicating the probabilities of false authentication (FA) or authentication error (AE) as a function of decision threshold for (e) correlation based and (f) HD based authentication .....	82
4.5	Cross-fab analysis: (a) QCI PUF spectra for a selected subset of 9 out of 28 PUFs from each Fab; (b) summary of cross-correlation	

	based authentication results ( $k = 3$ ) for all 56 PUFs; and (c) intra-chip and inter-chip distributions obtained when comparing PUF keys across or within each Fab .....	84
4.6	(Top) Correlation vs. HD results for (a) $k = 5$ , (b) $k = 4$ , (c) $k = 3$ , and (d) $k = 2$ . The correlation coefficient approaches 1 (or 0) as HD approaches 0 (or 0.5). A clear decision threshold cannot be drawn for HD method with $k = 5$ , whereas one can be drawn using the correlation method. (Bottom) summary table of measured means and standard deviations .....	85
5.1	(a) Microscope image of a silicon photonic moiré quasicrystal interferometer (QCI) with two grating couplers (GC1/GC2) and two integrated Ti/W micro-heaters. [Right] Experimentally measured QCI spectra in response to tuning micro-heater $I_2$ from 0 to 25 mA (5mA steps shown) while: (b) $I_1 = 10$ mA, and (c) $I_1 = 20$ mA .....	91
5.2	Instrumentation diagram. (Left) Tunable semiconductor laser connected to a polarization controller, optical circulator, fiber focuser, and power meter. (Right) Image of electrical probes contacting electrical pads to the PUF.....	93
5.3	Measured device spectra. (Top) Channel B is fixed at 10 mA, Channel A is swept from 0 mA to 30 mA. (Bottom) Channel B is fixed at 20 mA, Channel A is swept from 0 mA to 30 mA.....	95
5.4	Correlation analysis results of the electrically reconfigurable PUFs for 1 mA (left), 0.2 mA (top right) and 0.1 mA (bottom right) sweeps .....	96
5.5	Optical spectra at both arms of each PUF: confirms visible periodicity, yielding to electrically reconfigurable nature of QCI PUF.....	97
6.1	(a) SEM image of a typical fabricated sub-wavelength engineered silicon nanodisk (top view). (b) Electrical field profile of the resonant nanodisk. (c) Simulated and measured reflection spectra by the nanodisk arrays at normal incidence. The resonance is visible at $\sim 1074$ nm wavelength. (d) Corresponding enhancement of the incident electric field $E_0$ as measured in silicon at the center of the nanodisk with different disk heights.....	101

## CHAPTER 1

# INTRODUCTION

In recent times, silicon photonics has emerged as a revolutionary technology for producing opto-electronic devices and systems [1]. Silicon photonic waveguides are much smaller in size compared to traditional optical fibers and can easily be co-integrated with microelectronics using standard CMOS fabrication process on a single chip or chip stack. This results in cost effectiveness in transferring data both on-chip and through fiber under very broad bandwidth region. Silicon allows us to achieve countless photonic operations at a reasonably competitive performance level. Several practical approaches are ongoing to making cheap light sources and carrier at various levels of integration with the silicon platform. The silicon waveguide is a core building block in the modern integrated photonic systems thanks to its relatively high refractive index and lower direct bandgap. Among the wide range of applications of silicon waveguides, some of the highlighted sectors are resonant and non-resonant devices, data communications, sensing, nanomanipulation, non-linear quantum optics and much more [2]. To cope with the ever-increasing requirement of high data transfer rate and expanding bandwidth, subwavelength engineering of silicon photonic waveguides has shown extreme promise. Recent advancements in nanofabrication techniques have made it possible to implement subwavelength structures and hence, opened new doors to groundbreaking innovations in silicon photonics arena.



## 1.1 Introduction to Silicon Photonic Waveguides

An optical waveguide has the general property that there is always a material with high refractive index ( $n_{core}$ ) surrounded by a material with lower refractive index ( $n_{clad}$ ). Various types of waveguides are used in on-chip circuitry. A few of the basic ones are strip waveguides, rib waveguides, slot waveguides, subwavelength grating (SWG) waveguides, hybrid plasmonic-photonic waveguides, and plasmonic nanowires.

The geometrical features of these waveguides are generally sub-micron and as such they need to be fabricated with high spatial resolution and critical dimension (CD) accuracy typically  $<10$  nm. The applications of nanophotonic waveguide not only fall as active components in integrated opto-electronic circuits such as: phase shifters for modulators, as sensors for optical trapping or manipulation, but also as simple passive components including multiplexers, demultiplexers, filters and optical interconnects like bends, couplers and splitters [1,2].



Figure 1.1: Schematic of slab (left), strip (middle), and rib (right) waveguides

While evaluating the performance of any kind of waveguide, it is imperative to consider both its size and propagation loss. There are two fundamental types of propagation loss, intrinsic loss and extrinsic loss. For example, we can consider loss due to free carrier absorption as intrinsic loss, and scattering loss from side-wall roughness, or radiation leakage into the substrate, as extrinsic

loss. For doped waveguides used in active phase shifters for example, intrinsic loss often dominates. However, extrinsic loss is significant especially for nanophotonic silicon-on-insulator waveguides, owing to the high index contrast of Si/SiO<sub>2</sub>, the high field intensity at the waveguide sidewalls, and the non-negligible sidewall roughness introduced by dry etching.

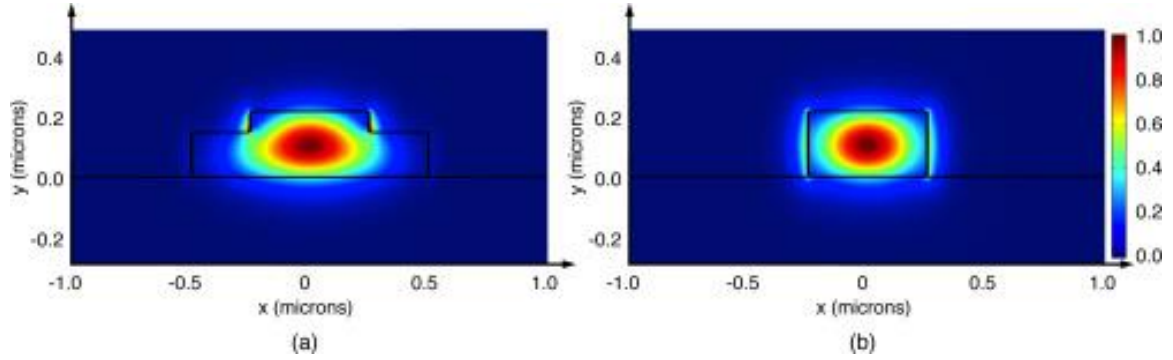


Fig. 1.2: TE mode in rib waveguide (left) and strip waveguide (right) [1,2]

Nowadays, applications for silicon photonics such as high bandwidth parallel, multiplexed, and coherent communications are becoming widespread and silicon photonic waveguides are the heart of it. But the prospects of silicon photonic waveguides are not limited only to data communications. Both commercial and research institutions involved in photonic technology are exploring numerous emerging applications. Areas of particular promise include: biosensing [3], imaging [4], LIDAR systems [5], inertial sensing [6], integrated photonics and opto-electronics [7][8], coherent communication [9], laser noise reduction [10], hybrid photonic-RFICs [11], and signal processing including quantum and all optical information processing [12].

## 1.2 Introduction to Subwavelength Engineering

Subwavelength engineering is an effective way to vary the refractive index of a waveguide. It was first proposed to realize light coupling and mode conversion in one-dimensional (1D) subwavelength grating (SWG) waveguides [13]. In general, “subwavelength” refers to a structural

period with which the Bragg reflection and diffraction effects are suppressed in the structure. By changing the period and duty cycle of an SWG, the effective index, dispersion, and optical field confinement can be flexibly adjusted over a wide range. Subwavelength structures such as subwavelength gratings (SWGs) and subwavelength metamaterials are capable of tailoring the optical properties of materials and controlling the flow of light at the nanoscale. The effective indices of the subwavelength structured strip and slab waveguides can be changed in a wide range by choosing an appropriate duty cycle or a filling factor of silicon, which provides an effective method to manipulate the optical field and achieve effective index matching for functional devices.

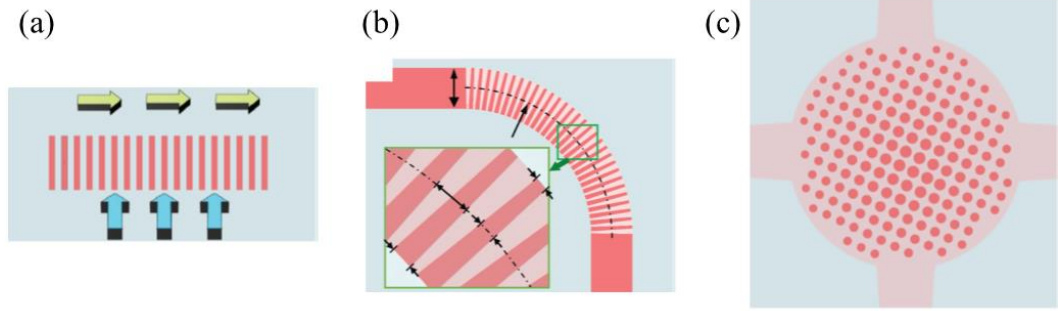


Fig. 1.3: Schematic diagrams of various subwavelength structured strip and slab waveguides. (a) SWG waveguide, (b) 90° waveguide bend, and (c) multimode crossing based on the subwavelength metamaterial. The red, pink, and gray colors represent silicon, partially etched silicon, and silica, respectively. ‘b’ is reprinted from Wu et al. [13]. The structure in ‘c’ was reported in Xu and Shi [14].

Silicon photonics has recently witnessed significant growth in academic research and industrial applications, mainly due to its compatibility with the complementary metal oxide semiconductor (CMOS) fabrication process. The high refractive index of silicon ( $\sim 3.45$ ) enables a high contrast relative to the surrounding cladding of a silicon waveguide and thus high confinement of the optical field. These properties are desirable for achieving densely integrated photonic circuits. A number of well-known silicon waveguides based on different structures have been demonstrated, including strip waveguide, slab waveguide, slot waveguide, and photonic crystal waveguide [15]. However, unlike other III–V materials whose refractive indices can be flexibly varied by using different

constituent proportions, the refractive index of silicon is usually fixed, thus limiting the design freedom. Modal effective index matching and engineering are often needed in many devices, for example, couplers, polarization handling devices, and mode multiplexers. Therefore, it is highly desirable to find a methodology to change the effective refractive indices of silicon waveguides over a wide range through proper structural designs. In the subwavelength regime where the pitch is short enough, light propagates through subwavelength structured waveguides without radiation and Bragg reflection losses despite multiple discontinuities along the propagation direction. The subwavelength segments behave like an equivalent waveguide made of an artificial material, which can be fully described by the effective medium theory (EMT) [16]. A variety of devices with unprecedented performance have been demonstrated based on different design principles of subwavelength engineering. Among them, polarization handling devices (such as, polarizers, polarization rotators, beam splitters), mode manipulators, couplers and splitters, waveguide crossing and bend etc are some of the highly motivated research avenues. Therefore, it works as building blocks for optical as well as fiber-chip interconnects [17]. More details about the optical properties of subwavelength structured waveguides and example devices can be found here [18].

It is important to note that, the fabrication of such waveguides should be considered carefully as the resolution and fabrication errors may greatly affect the device performance. With the improvement of high-resolution lithography techniques, structures with feature sizes of  $\sim 100$  nm can be routinely fabricated on the SOI platform. In Figure 2, we illustrate the fabrication process of the subwavelength structured silicon devices, which is widely used in the silicon photonics field. It starts with an SOI wafer, which has a 220-nm-thick silicon layer on top, a 3- $\mu\text{m}$ -thick buried oxide layer in the middle, and a silicon substrate. Then EBL can be used to define the subwavelength structures and grating couplers on the photoresist, followed by the inductively

coupled plasma (ICP) dry etching to transfer the pattern onto the silicon wafer. After obtaining the partially etched subwavelength structures and grating couplers, the EBL and ICP etching procedures are repeated to form the fully etched silicon waveguides. Finally, plasma enhanced chemical vapor deposition (PECVD) is used to deposit a 2- $\mu\text{m}$  thick layer of silica on the whole wafer. The silica fills in the gap between the silicon segments. In this way, one can fabricate a silicon subwavelength structured waveguide embedded in the silica cladding material with CMOS-compatible processing.

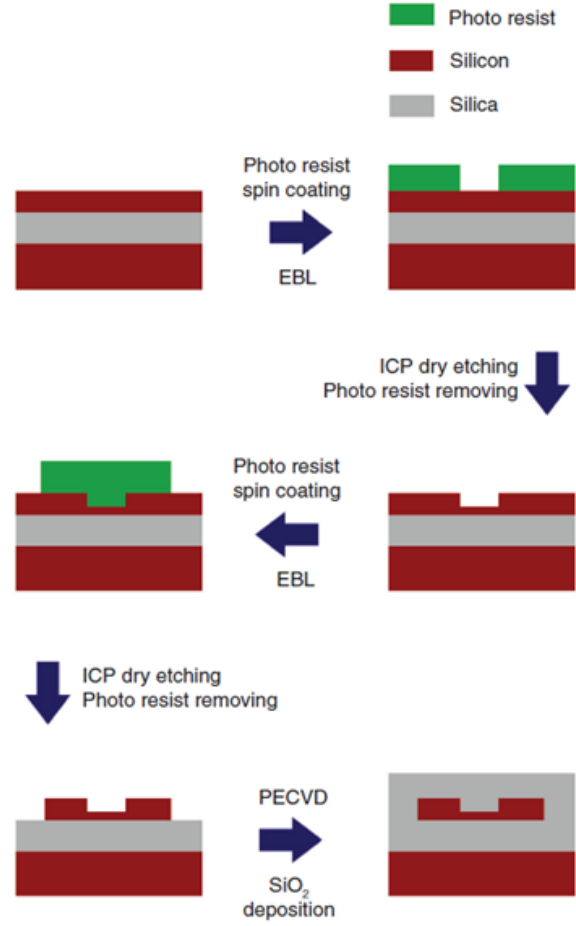


Fig. 1.4: Schematic diagram of the fabrication process of subwavelength structured silicon photonic device [19]

Subwavelength engineered waveguides exhibit exotic optical properties that cannot be realized with conventional waveguides. Therefore, several new areas of research are being conducted on the basis of this. Tailoring electromagnetic near fields, enhancing light-matter interactions, engineering anisotropy and effective medium effects, modal and dispersion engineering, nanoscale sensitivity etc are some of the highlighted topics that are being studied through subwavelength structuring of silicon photonic waveguides.

### 1.3 Motivation and Scope of Work

Modern fabrication technologies are getting advanced rapidly and hence recent years have seen a massive boom in subwavelength research not only in 1D SWG devices but also extending to two-dimensional (2D) index control in waveguides. This provides more freedom in optical field manipulation in the space domain, enabling new functional devices (e.g. mode converters) or improving the performances of integrated devices. Inspiring from this, in this research, we are going to introduce two new variants of silicon photonic waveguides as shown in Fig. 1.5.

1. Ultra-small mode area novel silicon V-groove waveguides
2. Moiré quasicrystals, i.e., nanoscale sidewall quasicrystalline gratings

Recently, we have theoretically demonstrated the novel nanoscale v-groove waveguide which can achieve ultra-small mode area and prove to be an excellent platform for enhancing light matter interactions [20]. On the other hand, quasicrystals oriented photonic architectures have been found to be promising primitive to achieve hardware and information security. The theory of these structures is based on optical interference. The two crucial phenomena addressed above can be optically solved by exploiting silicon photonics. Attractively, both structures are amenable through subwavelength engineering on standard CMOS platform. With the immense potential in the near-infrared wavelength regime, subwavelength engineered silicon photonic waveguides or nanowires can perform critically to overcome these challenges.

#### 1.3.1 Subwavelength Engineered Silicon Photonic Waveguide for Enhancing Light-Matter Interactions

We reported a novel silicon V-groove waveguide structure with deeply sub-wavelength field confinement. It is a special strip waveguide with a “V” shape groove in it. Our waveguide exploits

boundary conditions of Maxwell's equations to locally enhance the electric field while preserving confinement in the high index medium. It obtains ultra-low mode areas,  $A_{eff} \sim 0.003 \mu m^2$  [2] on par with plasmonic nanowires, in an all-dielectric platform. However, fabrication process of this structure hasn't been developed. Moreover, coupling light from a significantly bigger mode area (fiber, strip waveguide) to this ultra-low mode area waveguide is a challenge which hasn't yet been solved, especially, within a broadband regime. Accessing light efficiently to this ultra-small mode area V-groove should enable new avenues of subwavelength engineered silicon photonic waveguide and answer to the unsolved questions of silicon photonics foundries.

- In Chapter 2, we discuss detailed fabrication process of ultra-low mode area V-groove waveguide followed by demonstrating an efficient and broadband coupling technique to access light into it.

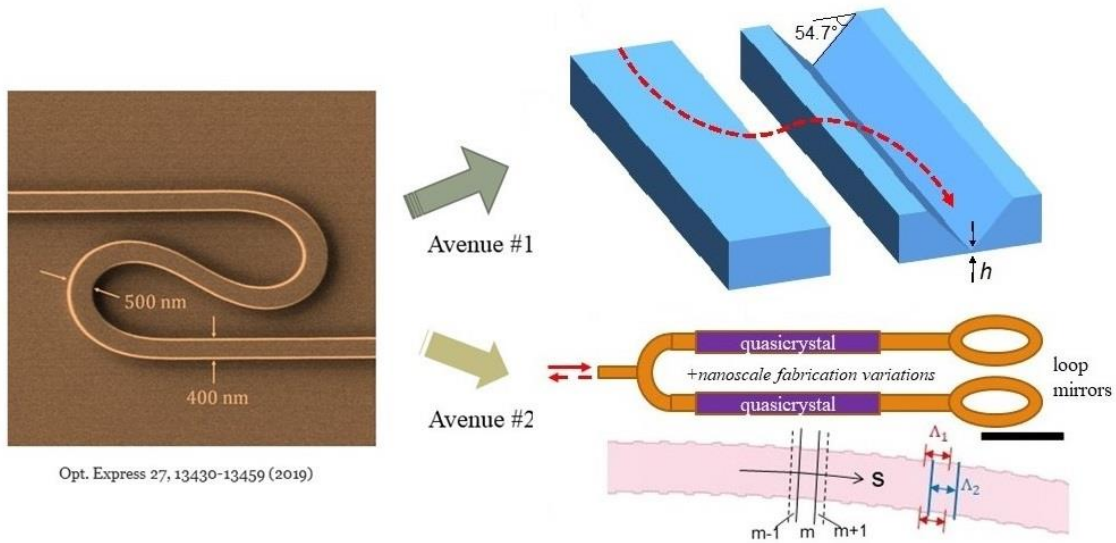


Fig. 1.5. Avenues of this research: two different versions of subwavelength structuring of silicon photonic waveguides; (1) enabling novel ultra-low mode area v-groove waveguide, (2) developing physical unclonable function from silicon photonic quasicrystal interferometer

### 1.3.2 Subwavelength Engineered Silicon Photonic Waveguide for Hardware and Information Security

The worldwide modern supply chain exposes our devices to potential adversaries. Ensuring the authenticity of a device or chip has been a matter of concern in real world. The current technology utilizes digital fingerprint technique, where the chip information is stored and then compared later to other chips decide if they are authentic or fake. However, this technique is not always accurate and these fingerprints can be easily cloned. Evidently, complexity does not guarantee security, therefore, demanding to the necessity of unclonability. On this note, physical unclonable functions or so-called PUFs have emerged as promising security primitive. In this work, we intend to establish a silicon photonic architecture, specifically, a PUF architecture and verify its secure authentication.

- In Chapter 3, we introduced a proof-of-concept silicon photonic physical unclonable function (PUF) realized from moiré quasicrystals and establish proper authentication.
- In Chapter 4, we expand the above-mentioned research to 56 identically designed distinct PUFs and verify their uniqueness and unclonability. To our knowledge, this is the largest sample size of physically distinct optical PUFs till date.
- In Chapter 5, we demonstrate an active as well as reconfigurable PUF architecture.
- Chapter 6 states the concluding remarks and directs towards the emerging and future applications.



## References

- [1] M. Li, W. H. P. Pernice, C. Xiong, T. Baehr-Jones, M. Hochberg, and H. X. Tang. “Harnessing optical forces in integrated photonic circuits”. *Nature* 456.27 (2008), pp. 480–484 (cit. on p. 7).
- [2] R. Soref. “Mid-infrared photonics in silicon and germanium”. *Nature Photonics* 4.8 (2010), pp. 495–497 (cit. on p. 7).
- [3] J. Hu, X. Sun, A. Agarwal, and L. Kimerling. “Design guidelines for optical resonator biochemical sensors”. *Journal Optics Society America B* 26 (2009), pp. 1032–1041 (cit. on p. 7).
- [4] Muzammil Iqbal, Martin A Gleeson, Bradley Spaugh, *et al.* “Label-free biosensor arrays based on silicon ring resonators and high-speed optical scanning instrumentation”. *IEEE Journal of Selected Topics in Quantum Electronics* 16.3 (2010), pp. 654–661 (cit. on p. 7).
- [5] J. K. Doylend, M. J. R. Heck, J. T. Bovington, *et al.* “Two-dimensional free-space beam steering with an optical phased array on silicon-on-insulator”. *Optics Express* 19.22 (2011), pp. 21 595–21 604 (cit. on p. 7).
- [6] R. B. Wehrspohn, S. L. Schweizer, T. Geppert, *et al.* “Chapter 12. Application of Photonic Crystals for Gas Detection and Sensing”. *Advances in Design, Fabrication, and Characterization*, K. Busch, S. Lalkes, R. B. Wehrspohn, and H. Fall (eds.), in *Photonic Crystals*: Wiley-VCH Verlag GmbH, 2006 (cit. on p. 7).
- [7] J. Capmany and D. Novak. “Microwave photonics combines two words”. *Nature Photonics* 1.6 (2007), pp. 319–330 (cit. on p. 7).
- [8] Maurizio Burla, Luis Romero Cortés, Ming Li, *et al.* “Integrated waveguide Bragg gratings for microwave photonics signal processing”. *Optics Express* 21.21 (2013), pp. 25 120–25 147. doi: 10.1364/OE.21.025120 (cit. on pp. 7, 8).

[9] C. R. Doerr, L. L. Buhl, Y. Baeyens, *et al.* “Packaged monolithic silicon 112-Gb/s coherent receiver”. *IEEE Photonics Technology Letters* 23.12 (2011), pp. 762–764 (cit. on p. 7).

[10] Firooz Aflatouni and Hossein Hashemi. “Wideband tunable laser phase noise reduction using single sideband modulation in an electro-optical feed-forward scheme”. *Optics Letters* 37.2 (2012), pp. 196–198 (cit. on p. 7).

[11] M. Ko, J. Youn, M. Lee, *et al.* “Silicon photonics-wireless interface IC for 60-GHz wireless link”. *IEEE Photonics Technology Letters* 24.13 (2012), pp. 1112–1114 (cit. on p. 7).

[12] C. R. Doerr, L. L. Buhl, Y. Baeyens, *et al.* “Packaged monolithic silicon 112-Gb/s coherent receiver”. *IEEE Photonics Technology Letters* 23.12 (2011), pp. 762–764 (cit. on p. 7).

[13] Wu H, Li C, Song L, et al. Ultra-sharp multimode waveguide bends with subwavelength gratings. *Laser Photon Rev* 2019;13:1800119.10.1002/lpor.201800119

[14] Xu H, Shi Y. Metamaterial-based Maxwell’s fisheye lens for multimode waveguide crossing. *Laser Photon Rev* 2018;12:1800094.

[15] Wim Bogaerts, Pieter Dumon, Bert Luyssaert, Peter Bienstman, “Nanophotonic Waveguides in Silicon-on-Insulator Fabricated with CMOS Technology,” *Journal of Lightwave Technology*, Vol. 23, NO. 1, January 2005

[16] Wissem Sfar Zaoui, “Efficient Coupling between Optical Fibers and Photonic Integrated Circuits,” PhD Dissertation, Institut für Elektrische und Optische Nachrichtentechnik der Universität Stuttgart, 2014

[17] R. Takei, M. Suzuki, E. Omoda, S. Manako, T. Kamei, M. Mori, and Y. Sakakibara, “Silicon knife-edge taper waveguide for ultralow-loss spot-size converter fabricated by photolithography,” *Applied Physics Letters* 102, 101108 (2013).

- [18] N. Fang, Z. Yang, A. Wu, J. Chen, M. Zhang, S. Zou, and X. Wang, “Three-dimensional tapered spot-size converter based on (111) silicon-on-insulator,” *IEEE Photonics Technology Letters*, Vol. 21, No. 12, 820-822 (2009).
- [19] P. J. Bock et al., “Subwavelength grating periodic structures in silicon-on-insulator: A new type of microphotonic waveguide,” *Optics express*. 18. 20251-62. 10.1364/OE.18.020251 (2010).
- [20] N. Sakib and J. D. Ryckman, “Extreme sub-wavelength optical confinement in nanostructured all-dielectric silicon waveguides,” Conference on Laser and Electro-Optics (2019).

# ENABLING NOVEL SUBDIFFRACTION V-GROOVE WAVEGUIDE

### 2.1 Introduction

The optical waveguide is an important building block which is heavily relied upon to enable photonic applications in data communications [1], biosensing [2], 3D imaging and light detection and ranging systems [3,4], inertial sensing [5], nanoparticle manipulation [6], hardware security [7,8], photonic circuits for classical or quantum information processing [9,10] and more. Attractively, silicon offers a high refractive index alongside its infrared transparency, which promotes small mode dimensions, compact device size, and the opportunity to enhance light-matter interactions. However, the mode dimensions and field enhancement of conventional waveguides, such as the silicon strip waveguide depicted in Fig. 2.1a, are generally restricted by the diffraction limit. This limit can be broken by exploiting subdiffraction phenomena that locally enhance the near-field, on the subwavelength scale, through mechanisms that are distinct from interference phenomena, as exemplified in slot waveguides [11], hybrid dielectric-plasmonic waveguides [12], and anisotropy-engineered waveguides [13] excited under the appropriate polarization.

Recently, we have designed and introduced novel silicon based subdiffraction waveguides [14], such as the silicon V-groove waveguide depicted in Fig. 2.1b. This waveguide design exploits two boundary conditions of Maxwell's equations to constrain the eigenmode solution, enhance the

electric field *within silicon*, and achieve ultra-small mode areas,  $A_n \approx 10^{-3} \lambda_0^2$ , on par with plasmonic nanowires but in an all-dielectric platform. Reductions in mode area correspond to enhancements in the maximum electric field energy density,  $u_e = \frac{1}{2} \epsilon |E|^2$ , as observed in Fig. 2.1d for the silicon V-groove waveguide when compared to the silicon strip waveguide depicted in Fig. 2.1c. The silicon V-groove waveguide is amenable to fabrication by wet etching of crystalline (100) silicon, an approach which fosters low surface roughness and precisely controlled critical dimensions [15]. However, to harness the prospective benefits of this ultra-small mode area waveguide in enhancing light-matter interactions, it is necessary to first identify a solution for efficient input/output coupling. While prior works have studied and developed optical couplers for interfacing with slot waveguides [16,17] and plasmonic waveguides [18,19], no such coupler has been introduced for all-dielectric subdiffraction waveguides such as the silicon V-groove or diabolito type waveguides as described in Ref. [14]. The motivation of this work is to develop and investigate an efficient, broadband, and fabrication tolerant optical coupling solution for interfacing with subdiffraction all-dielectric waveguides with ultra-low mode area, using the silicon V-groove waveguide as a prototypical example.

The ultra-small mode area of the silicon V-groove waveguide coincides with a significant mode and phase mismatch relative to conventional silicon strip waveguides. Moreover, the propagation constant of the silicon V-groove waveguide exhibits amplified sensitivity to certain geometric parameters, such as the bridge height,  $h$ , of silicon remaining below the groove, where the electric field energy density is strongly enhanced, as visualized in Fig. 2.1d,e [14]. To overcome these

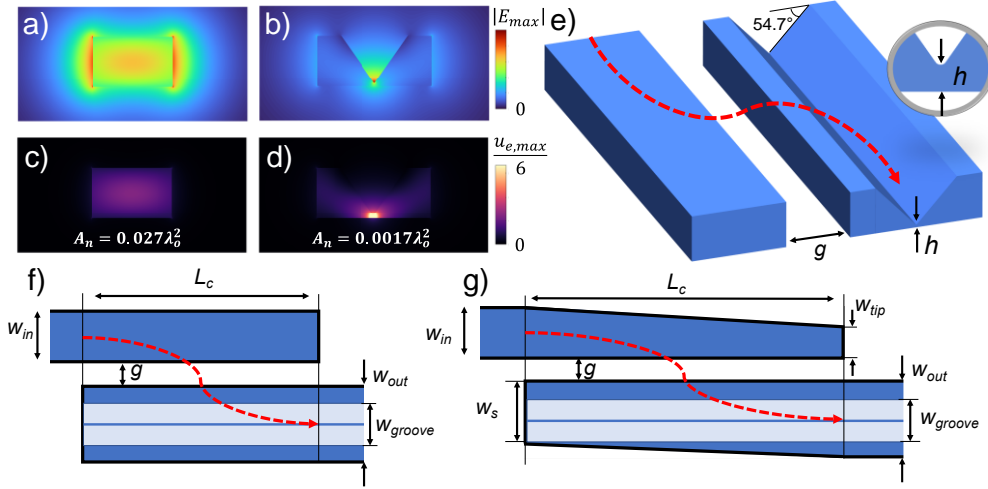


Fig. 2.1. (a) Electric field mode profile of a silicon strip waveguide (350 nm x 220 nm) and (b) silicon V-groove waveguide with  $h = 14$  nm cladded by  $\text{SiO}_2$  (fundamental quasi-TE modes). (c) electric field energy density,  $u_e = \frac{1}{2} \epsilon |E|^2$ , for the strip waveguide and (d) silicon V-groove waveguide normalized to the same color scale. Values above  $1/6^{\text{th}}$  the max value,  $u_{e,max}$ , are saturated to show detail. (e) Schematic of the evanescent coupling architecture and two prospective approaches: (f) non-adiabatic directional coupling, and (g) adiabatic mode evolution.

issues and facilitate efficient coupling, we consider two prospective coupling strategies: (1) non-adiabatic directional coupling as illustrated in Fig. 2.1f, and (2) adiabatic mode evolution as illustrated in Fig. 2.1g. We then perform a rigorous theoretical comparison between these techniques to identify their respective benefits and/or limitations.

## 2.2 Design Methodology

### 2.2.1 Non-adiabatic directional coupling

As detailed by Yariv [20] and later refined by Hardy and Streifer [21], the directional coupler allows for complete power transfer between any two waveguides, regardless of their cross-sectional

design, so long as they can be phase-matched and placed in proximity to one another. Here, we employ coupled mode theory to design and predict the properties of a directional coupler formed by the evanescent interaction between a conventional strip waveguide and an ultra-low mode area V-groove waveguide (Fig. 2.1f). Although the appropriate choice of gap and coupler length naturally leads to a prospective design solution, the overall coupling performance must then be evaluated by also considering both fabrication tolerances and optical bandwidth.

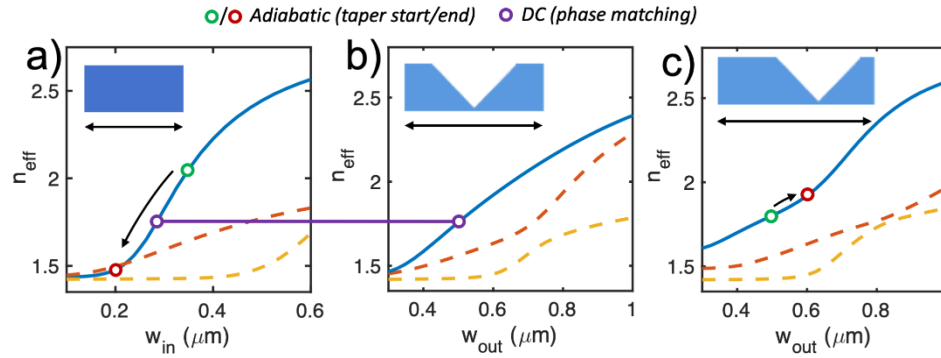


Fig. 2.2. Effective indices as a function of waveguide width for: (a) the strip waveguide, (b) centered V-groove waveguide, and (c) off-centered V-groove waveguide (centered only at  $w_{\text{out}} = 600 \text{ nm}$ ). Purple markers indicate phase matching design points, while green/red markers indicate taper start/end points. Dashed lines indicate higher order modes.

Fig. 2.2 presents the effective index vs. waveguide width for isolated silicon strip and V-groove waveguides, evaluated at  $\lambda_0 = 1550 \text{ nm}$ . The design is targeted for fundamental mode quasi-transverse-electric ( $\text{TE}_0$ ) coupling into a nominal silicon V-groove waveguide in 220 nm silicon-on-insulator (SOI), e.g. Fig. 2.1b, where  $w_{\text{out}} = 500 \text{ nm}$  and  $h = 14 \text{ nm}$ . The value of  $w_{\text{groove}}$  is parametrically defined alongside our choice of  $h$  according to  $w_{\text{groove}} = 2(220 \text{ nm} - h)/\tan(54.7^\circ)$  since we consider a fixed 220 nm silicon thickness and a  $54.7^\circ$  groove angle consistent with wet etching of (100) silicon. For this V-groove waveguide, phase matching is achieved with a strip width  $w_{\text{in}} = 283 \text{ nm}$  as indicated by the purple marker in Fig. 2.2a and 2.2b.

For a given choice of gap,  $g$ , the coupling coefficient  $\kappa$  and required coupler length  $L_c$  can be

derived from the effective indices  $n_1$  and  $n_2$  of the coupled waveguide system's first two eigenmodes – i.e., the symmetric and anti-symmetric supermodes of the directional coupler. Where  $\Delta n$  is the difference  $n_1 - n_2$  between the effective indices, at an operating wavelength  $\lambda_0$ , the fractional power coupling is described according to  $\kappa^2 = \sin^2(z(\pi\Delta n)/\lambda_0)$ . Complete power transfer and localization in one waveguide requires accumulating a  $\pi$  phase difference between the supermodes, which occurs at the cross-over length,  $z = L_c = \lambda_0/2\Delta n$ . Choosing  $g = 300$  nm alongside our nominal waveguide designs as an example, yields  $\kappa^2 > 0.99$  for a coupler length  $L_c = 9.5$   $\mu\text{m}$ .

### 2.2.2 Adiabatic mode evolution

Operation of our adiabatic coupler based on mode evolution is distinct from phase matched directional coupling, in that it does not excite multiple supermodes but rather preserves light in the lowest order (highest effective index) supermode. Unlike adiabatic 2x2 couplers which rely on the same general concept [22], our device functions as a mode convertor which localizes light in one input (strip waveguide) and one output (V-groove waveguide). The design problem is then two-fold: (1) modulate the waveguide cross-sectional design along the optical axis to control where the lowest order eigenmode resides, e.g., employing tapering to localize the fundamental mode in either the strip or V-groove waveguide; and (2) ensure the tapering is sufficiently gradual such that high order modes and/or radiation modes are not excited. In our designs, we employ linear tapers on both the strip and V-groove waveguides. We further assume the dimensions of the V-groove to be constrained by wet etching and constant vs. length, so that we only taper the outer width of the V-groove waveguide. In principle, adiabatic mode evolution can be achieved by tapering solely the strip waveguide. Here, we prefer to employ dual tapering of both waveguides since it leads to reasonably compact design solution with a modest strip waveguide tip size,  $w_{tip} = 200$  nm. The widths of the waveguide taper start and end points are illustrated in Fig. 2.2(a,c) via the green and



red markers respectively. Our nominal adiabatic design utilizes:  $w_{in} = 350$  nm,  $w_{tip} = 200$  nm,  $w_s = 500$  nm, and  $w_{out} = 600$  nm.

Figure 2.3 depicts the effective indices and mode profiles of the three lowest order supermodes in the adiabatic taper design. At the start of the taper the fundamental supermode confines light to the strip waveguide, whereas at the end of the taper light is localized in the ultra-small mode area V-groove waveguide. For a sufficiently long or adiabatic taper, light will be preserved in the fundamental supermode and higher order supermodes should not be excited to any significant degree. Interestingly, the higher order supermodes exhibit polarization rotation, an effect which is

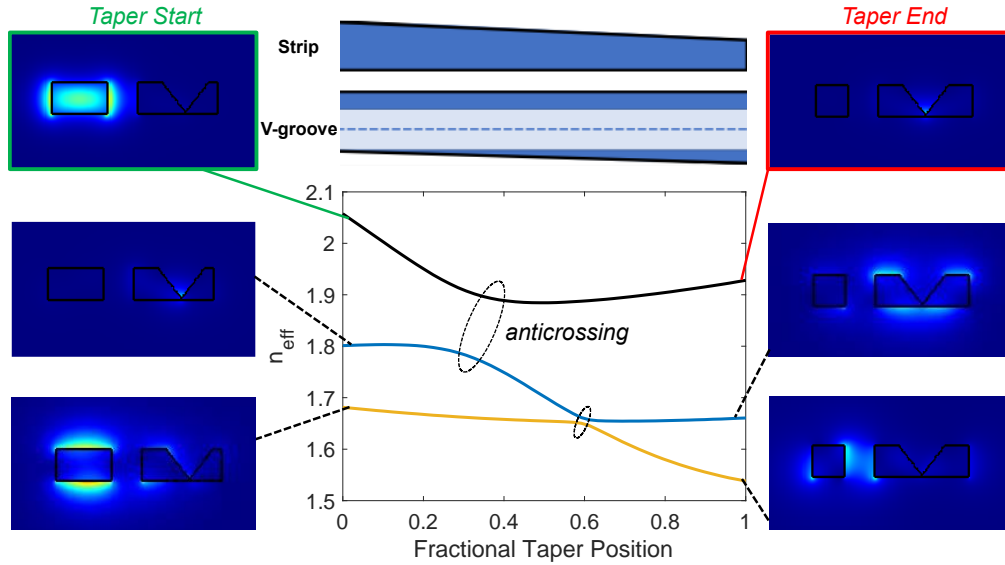


Fig. 2.3. Visualization of the supermodes' electric field intensity and effective indices in the adiabatic mode evolution design, where:  $w_{in} = 350$  nm,  $w_{tip} = 200$  nm,  $w_s = 500$  nm,  $w_{out} = 600$  nm, and  $g = 200$  nm. The strip waveguide supermode evolves into a V-groove waveguide supermode as the taper passes through an anticrossing. Higher order supermodes exhibit polarization rotation effects.

aided by the broken vertical symmetry of the V-groove structure. This suggests the V-groove geometry could prove useful in polarization diverse applications, such as in the design of on-chip polarization rotators [23,24]. This is however not the focus of the present study, as we are focused on efficiently coupling light into the fundamental quasi-TE mode of the V-groove waveguide from the fundamental quasi-TE mode of a strip waveguide.

The coupling efficiency was evaluated vs. taper length for various gaps, using a commercially available 3D eigenmode expansion (EME) solver (Lumerical Inc.) with results depicted in Fig. 2.4. The coupling efficiency is defined as  $P_{out}/P_{in} \times 100\%$  which describes the ratio of power in the desired output V-groove mode,  $P_{out}$ , normalized to the input power launched into the strip waveguide,  $P_{in}$ . For gaps  $g = 200$  nm or  $300$  nm,  $>99\%$  efficiency is observed for  $L_c > 100$   $\mu\text{m}$  and  $200$   $\mu\text{m}$  respectively. To provide manufacturing margin and ensure broadband operation, we select lengths  $L_c = 124$   $\mu\text{m}$  and  $250$   $\mu\text{m}$  for our respective  $g = 200$  nm and  $300$  nm adiabatic coupler designs. We've also independently quantified the worst case substrate leakage loss [25] for two buried oxide (BOX) thicknesses. For a BOX thickness of  $1$   $\mu\text{m}$  the substrate leakage is  $\sim 5.5$  dB/cm at the mid-point of the taper; whereas a BOX thickness of  $2$   $\mu\text{m}$  is adequate to suppress this value to  $<0.001$  dB/cm, making it is negligible compared to typical propagation losses.

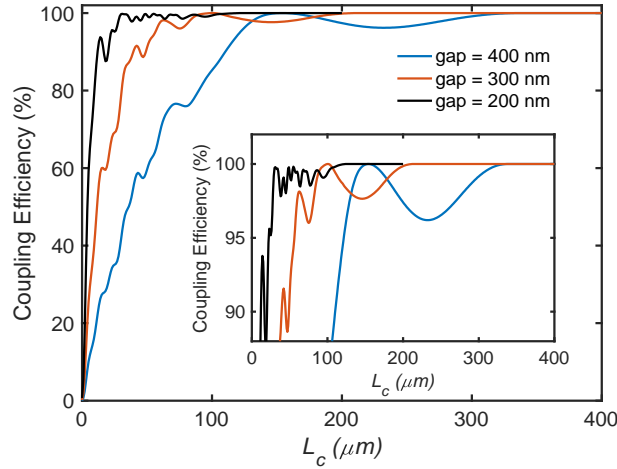


Fig. 2.4. Evaluation of the adiabatic mode evolution based design: coupling efficiency vs. coupler length for varying gaps.

### 2.3 Performance Evaluation

Fig. 2.5 presents a visualization of the simulated electric field  $|E|$  profile for both the directional coupler and adiabatic mode evolution based designs, where light is injected into the strip waveguide

before the coupling region. Both structures successfully achieve high  $>99\%$  coupling efficiency from a silicon strip waveguide into an ultra-small mode area V-groove waveguide. At a glance, it might appear as though both devices perform equivalently, except for the more compact footprint of the directional coupler. These results, however, are for the nominally ideal case which assumes zero fabrication errors and operation at exactly 1550 nm. In practice, these devices must achieve high coupling efficiency amidst non-zero errors in critical dimensions (CD), and ideally over a broad wavelength window.

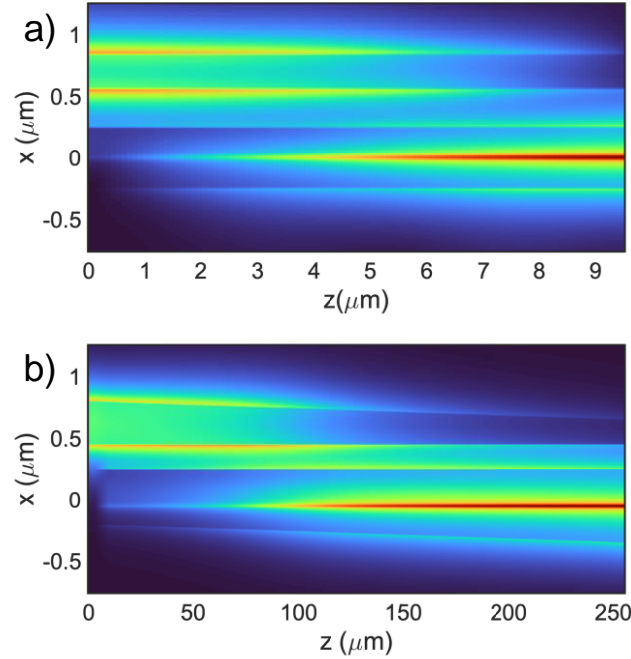


Fig. 2.5. Simulated electric field  $|E|$  for: (a) directional coupler and (b) adiabatic mode evolution based example designs. The field profiles are taken at the plane  $y = 15$  nm above the  $\text{SiO}_2/\text{Si}$  interface.

Next, we investigate the fabrication tolerance of both designs by skewing three critical dimensions: (1) silicon device layer thickness (nominal = 220 nm), (2) global variations in waveguide width  $\Delta w$ , and (3) variations in the V-groove dimension. Here we assume the V-groove angle is held constant at  $54.7^\circ$  and consider nanoscale errors in the silicon bridge height  $\Delta h$  remaining beneath the groove (see Fig. 2.1(c)). Given the strong field concentration near the tip of

the V-groove, the effective index is especially sensitive to both the silicon device layer thickness and the V-groove etch depth which control  $h$  [14]. As observed in Fig. 2.6(a), the directional coupler design is very sensitive to device layer thickness, falling to ~50% efficiency for a 10 nm thickness deviation. Meanwhile the adiabatic design shows negligible impact from silicon thickness variations.

Fig. 2.6(b) reports the coupling efficiency as a function of the CD error in waveguide width,  $\Delta w$ . Here the nominal designs are biased according to  $w_{\text{actual}} = w_{\text{design}} + \Delta w$  to mimic the effect of CD bias errors that may occur after lithography and/or etching. We observe the directional coupler based design to suffer a strong coupling loss penalty as a function of  $\Delta w$ , whereas the adiabatic design shows no measurable impact to coupling efficiency. The observed penalty in the directional coupler case arises due to two closely related effects. First, the perfectly phase matched condition of the ideal structure breaks in the presence of width bias because, unlike a conventional directional coupler formed from an equivalent waveguide pair, the strip waveguide and V-groove waveguide are not symmetric structures. As visible in curves of Fig. 2.2(a,b), the strip waveguide and V-groove waveguide exhibit different effective index sensitivities to waveguide width,  $dn_{\text{eff}}/dw$ , resulting in a phase mismatch which grows with CD error. Secondly, for non-zero  $\Delta w$  the beat length deviates from the nominal design value, as in a traditional directional coupler, and therefore the maximum coupling occurs at a different design point. Neither of these two challenges exist in the adiabatic coupler design and thus it can perform equally well for any CD error  $\Delta w$  considered in the range from -30 nm to +30 nm.

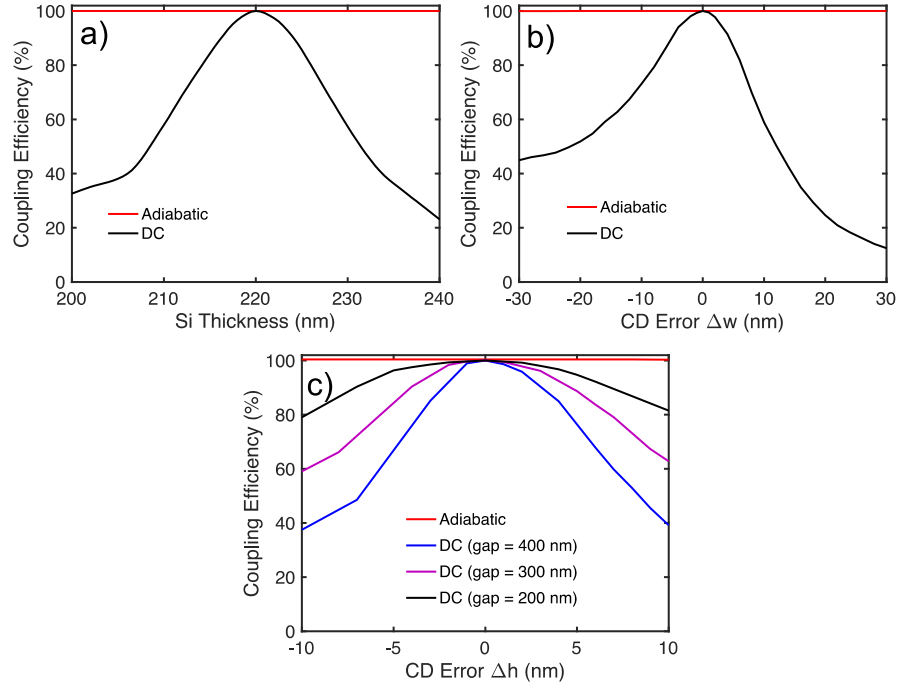


Fig. 2.6. Simulated coupling efficiencies of adiabatic and directional coupler (DC) type devices vs. three key parameters: (a) silicon device layer thickness, (b) error in waveguide width  $\Delta w$  and (b) error in V-groove bridge height  $\Delta h$  (as depicted in Fig. 2.1(c)).

Fig. 2.6(c) reports the coupling efficiency as a function of the CD error  $\Delta h$ , where we assume  $h_{\text{actual}} = h_{\text{design}} + \Delta h$  and evaluate device performance for the case  $h_{\text{design}} = 14$  nm. As was found for CD errors in waveguide width, we observe that the directional coupler based design suffers a significant coupling loss penalty with increasing CD error  $\Delta h$ . We further explore how this penalty is affected by the choice of coupler gap. Notably, we observe that larger gap designs suffer a stronger penalty vs. CD error, with the coupling efficiency falling to  $\sim 40\%$  for the  $g = 400$  nm design and  $\sim 82\%$  for the  $g = 200$  nm design for a CD error  $\Delta h = +10$  nm. The adiabatic design again shows robust tolerance to CD errors. In this case, the adiabatic design benefits from the fact that the strip waveguide taper spans a large range of  $n_{\text{eff}}$  from  $\sim 1.5$  to  $\sim 2.1$ , while the corner case effective indices of the V-groove waveguide are always contained well within this range. Hence,

the CD errors considered here are not large enough to impact the localization of the lowest order eigenmode or to substantially alter the device efficiency.

Lastly, we evaluated the wavelength dependence of both coupler types over the range  $\lambda_0 = 1550 \text{ nm} \pm 100 \text{ nm}$ . Consistent with expectations, we find the adiabatic mode evolution based design exhibits superior bandwidth as compared to the directional coupler based design as illustrated in Fig. 2.7. Specifically, these two design types are found to exhibit  $>95\%$  coupling efficiency over wavelength ranges of  $>200 \text{ nm}$  and  $\sim 50 \text{ nm}$  respectively. To provide additional insight into the CD error penalties associated with the directional coupler in particular, we also illustrate wavelength dependence of devices where  $h_{\text{actual}}$  is set to  $10 \text{ nm}$  or  $19 \text{ nm}$ , equivalent to  $\Delta h = -4 \text{ nm}$  and  $+5 \text{ nm}$  respectively. A clear shift in wavelength is seen for changing heights. Here, these small nanoscale variations in bridge height shift the peak coupling wavelength of the directional coupler based design by  $\pm 50 \text{ nm}$ . This highlights the difficult task of operating with a directional coupler, especially when the coupled waveguides are dissimilar in nature and asymmetrically sensitive to fabrication variations.

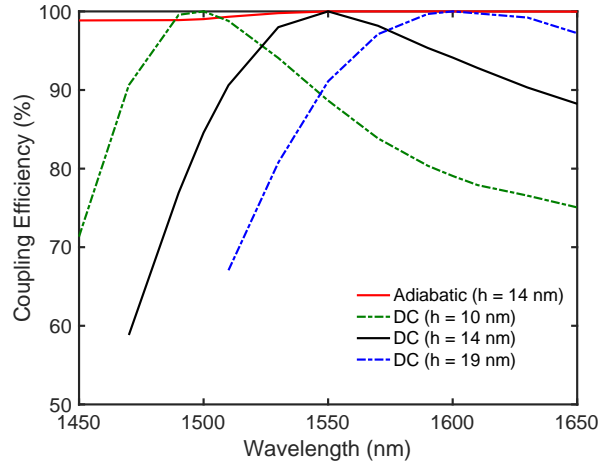


Fig. 2.7. Simulated wavelength dependence of nominal adiabatic and directional coupler (DC) type devices, and two illustrative examples of DCs with CD errors.

## 2.4 Fabrication of V-groove Waveguide

The V-groove geometry is amenable to fabrication by wet etching of crystalline (100) silicon, an approach which fosters low surface roughness and highly controlled critical dimensions. The outer dimensions of the original V-groove structure is 500 nm x 220 nm. We utilize a 200 nm nominal gap between the V-groove waveguide and strip waveguide. We assume a Si core cladded on all sides by SiO<sub>2</sub>. The V-groove geometry is constrained to a 54.7 deg facet angle, owing to the use of wet etching. To achieve this nanoscale feature size with adequate precision, we employ electron-beam lithography (EBL) technique. The fabrication process is done inside the cleanroom of Center for Nanophase Materials Sciences (CNMS) at Oak Ridge National Laboratories, TN. The fabrication process flow of V-groove waveguide is stated in the following subsection.

### 2.4.1 V-groove Waveguide Fabrication Process Flow

Overview of two primary ‘self-aligned’ processes under investigation for the realization of deeply subwavelength all-dielectric silicon waveguides are shown in Fig. 2.8. The first type of process utilizes dry etching through hardmask and silicon device layer followed by lateral wet etching v-grooves into silicon sidewalls, we can call this “Diabolo” structure. In the second process, dry etching through hardmask is followed by vertical wet etching of v-grooves into a silicon device layer. Reference waveguides (without grooves) can be prepared as shown in the bottom panels by using the appropriate process and/or mask design. Note that, two different SOI substrates are used while achieving the processes: 340 nm SOI for “Diabolo” and 220 nm SOI for “V-groove” architecture.

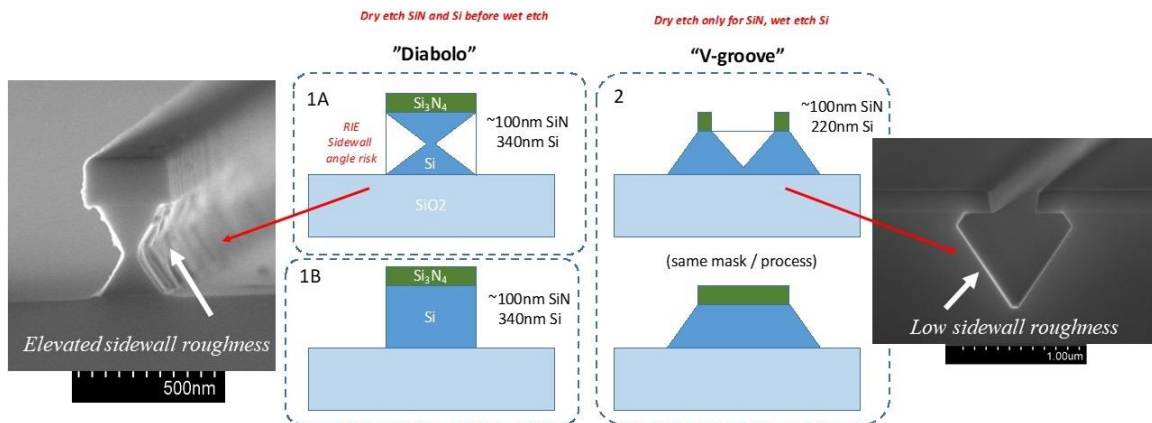


Fig. 2.8: Single layer process flow of “Diabolo” (left) and “V-groove” (right) structures

The fabrication recipe of both “Diabolo” and “V-groove” structures are developed through rigorous trial and error process in the cleanroom environment. Sample recipe for both structures are listed below.

#### A. Diabolo Sample Recipe (340 nm SOI)

1. Design: diabolo\_structure\_v22
2. Clean: Oxide cleaning, duration 1 minute
3. Nitride Deposition: Si Rich Low Stress, Duration: 15 min, Thickness: ~ 200 nm
4. Annealing: Anneal N2 350C, duration 1 min
5. Coat: Zep 520A at 6000rpm, program 6
6. Bake: 180C for 2 min
7. EBL: DSv1final.v30, DSv1Nov7.sdf, DSv1Nov7.jdf - around 6 hours
8. Develop: Xylene 35 sec and rinse with IPA
9. Nitride Etch (RIE): Recipe- Ivan SiN, duration 30 sec



10. Dry Etch (RIE): Recipe- Opt Si waveguide, duration 3min

11. Wet Etch: 30% KOH at 40C, duration 90 sec

12. Clean: NMP

*B. V-groove Sample Recipe (220 nm SOI)*

1. Clean: Oxide clean

2. Nitride Deposition: PECVD, Duration: 15 min, Thickness: ~ 200 nm

3. Descum

4. Coat: Zep 520A, 3000 rpm, duration 45 sec

5. Bake: 180C for 2 min

6. Patterning: EBL

7. Develop: Xylene, duration 45 sec and rinse with IPA

8. Descum

9. RIE Etch: Recipe- Ivan SiN, duration 30 sec

10. Wet Etch: 30% KOH at 40C, duration 45 sec

11. Clean: NMP

2.4.2 SEM Images of V-groove Waveguides

Scanning Electron Microscopy (SEM) images show the formation of the v-groove waveguides. On the mask design, there were an array of multiple waveguides with different groove widths and heights. Among those, the top three waveguides are presented in Fig. 2.9.

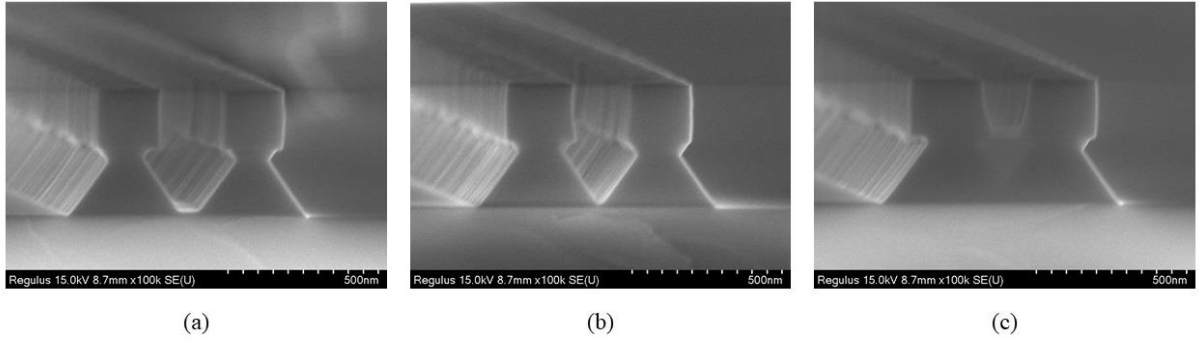


Fig. 2.9: SEM Images of all-dielectric V-groove waveguides with different groove widths and heights attained from single layer fabrication process

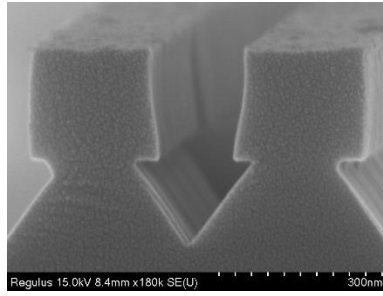


Fig. 2.10: SEM image of the waveguide in Fig. 2.9(c) from the other side

## 2.5 Experimental Verification of V-groove Waveguides

The v-groove waveguides shown have been tested at 1560 nm wavelength. Using generic waveguide setup we achieved waveguiding for each of the waveguides shown in Fig. 2.9. The results in terms of top view and side view for the corresponding waveguides are shown in Fig. 2.11.

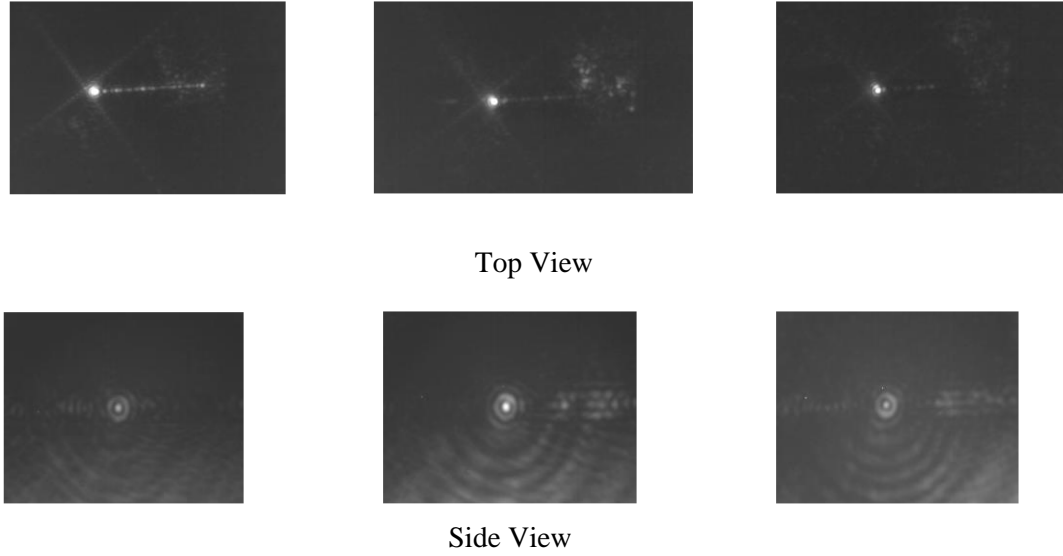


Fig. 2.11: Experimental verification of waveguiding (top view and side view) for the v-groove waveguides shown in Fig. 2.9

## 2.6 Summary

In this chapter, we theoretically investigated the coupling performance of a strip to V-groove waveguide coupler in both adiabatic and non-adiabatic regimes. We showed that both design types are theoretically capable of achieving low loss coupling into ultra-small mode area silicon V-groove waveguides. However, the adiabatic mode evolution based design provides better overall performance amidst realistic fabrication non-idealities alongside a wider operating bandwidth in comparison to the non-adiabatic design. Despite requiring a longer device length in general, the adiabatic coupler is favored since it is more robust yet remains simple to design. We expect many of the design principles utilized here can equally apply to other types of waveguide systems, particularly those which interface between conventional modes and dissimilar modes or those exhibiting strong sub-diffraction character.

We also developed a single layer fabrication technique of all-dielectric subdiffraction ultra-low mode area waveguides in the shape of v-groove and diabolos. Moreover, we experimentally demonstrated the waveguiding phenomena with the fabricated v-groove waveguides. We presented the directional coupler version of this work in IEEE Photonics Conference in the year 2019 [26] and later published a journal in Optics Continuum [27] on both the coupling techniques. These results illustrate a clear path to efficiently interfacing with novel types of all-dielectric subdiffraction waveguides, thus making them accessible in future experimental works that seek to harness their strong subwavelength field enhancement.

## References

1. N. Margalit, C. Xiang, S.M. Bowers, A. Bjorlin, R. Blum, and J.E. Bowers, "*Perspective on the future of silicon photonics and electronics*," *Appl. Phys. Lett.* **118**, 22 (2021).
2. S. TalebiFard, S. Schmidt, W. Shi, W. Wu, N.A.F. Jaeger, E. Kwok, D.M. Ratner, and L. Chrostowski, "*Optimized sensitivity of Silicon-on-Insulator (SOI) strip waveguide resonator sensor*," *Biomed. Opt. Express* **8**, 2 (2017).
3. C. Rogers, A.Y. Piggott, D.J. Thomson, R.F. Wiser, I.E. Opris, S.A. Fortune, A.J. Compston, A. Gondarenko, F. Meng, X. Chen, G.T. Reed, and R. Nicolaescu, "*A universal 3D imaging sensor on a silicon photonics platform*," *Nature* **590**, 7845 (2021).
4. D.N. Hutchison, J. Sun, J.K. Doylend, R. Kumar, J. Heck, W. Kim, C.T. Phare, A. Feshali, and H. Rong, "*High-resolution aliasing-free optical beam steering*," *Optica* **3**, 8 (2016).
5. S. Bramhavar, D. Kharas, and P. Juodawlkis, Integrated Photonic Inertial Sensors, in: OSA Adv. Photonics Congr. 2019 (IPR, Networks, NOMA, SPPCom, PVLED), Optical Society of America, Burlingame, California (2019), p. ITh3A.2.

6. A.H.J. Yang, S.D. Moore, B.S. Schmidt, M. Klug, M. Lipson, and D. Erickson, "*Optical manipulation of nanoparticles and biomolecules in sub-wavelength slot waveguides*," *Nature* **457**, 7225 (2009).
7. F. Bin Tarik, A. Famili, Y. Lao, and J.D. Ryckman, "*Robust optical physical unclonable function using disordered photonic integrated circuits*," *Nanophotonics* **9**, 9 (2020).
8. B.C. Grubel, B.T. Bosworth, M.R. Kossey, H. Sun, A.B. Cooper, M.A. Foster, and A.C. Foster, "*Silicon photonic physical unclonable function*," *Opt. Express* **25**, 11 (2017).
9. B.J. Shastri, A.N. Tait, T. Ferreira de Lima, W.H.P. Pernice, H. Bhaskaran, C.D. Wright, and P.R. Prucnal, "*Photonics for artificial intelligence and neuromorphic computing*," *Nat. Photonics* **15**, 2 (2021).
10. X. Qiang, X. Zhou, J. Wang, C.M. Wilkes, T. Loke, S. O’Gara, L. Kling, G.D. Marshall, R. Santagati, T.C. Ralph, J.B. Wang, J.L. O’Brien, M.G. Thompson, and J.C.F. Matthews, "*Large-scale silicon quantum photonics implementing arbitrary two-qubit processing*," *Nat. Photonics* **12**, 9 (2018).
11. V.R. Almeida, Q. Xu, C.A. Barrios, and M. Lipson, "*Guiding and confining light in void nanostructure*," *Opt. Lett.* **29**, 11 (2004).
12. Y. Bian, Q. Ren, L. Kang, T. Yue, P.L. Werner, and D.H. Werner, "*Deep-subwavelength light transmission in hybrid nanowire-loaded silicon nano-rib waveguides*," *Photonics Res.* **6**, 1 (2018).
13. S. Jahani and Z. Jacob, "*Transparent subdiffraction optics : nanoscale light confinement without metal*," *Optica* **1**, 2 (2014).
14. N. Sakib and J.D. Ryckman, "*Design of ultra-small mode area all-dielectric waveguides exploiting the vectorial nature of light*," *Opt. Lett.* **45**, 17 (2020).
15. S. Migita, Y. Morita, M. Masahara, and H. Ota, "*Fabrication and Demonstration of 3-*

*nm-Channel-Length Junctionless Field-Effect Transistors on Silicon-on-Insulator Substrates Using Anisotropic Wet Etching and Lateral Diffusion of Dopants*," *Jpn. J. Appl. Phys.* **52**, 4S (2013).

16. N.-N. Feng, R. Sun, L.C. Kimerling, and J. Michel, "Lossless strip-to-slot waveguide transformer," *Opt. Lett.* **32**, 10 (2007).

17. Z.C. Wang, N. Zhu, Y.B. Tang, L. Wosinski, D.X. Dai, and S.L. He, "Ultracompact low-loss coupler between strip and slot waveguides," *Opt. Lett.* **34**, 10 (2009).

18. C.T. Chen, X. Xu, A. Hosseini, Z. Pan, H. Subbaraman, X. Zhang, and R.T. Chen, "Design of highly efficient hybrid Si-Au taper for dielectric strip waveguide to plasmonic slot waveguide mode converter," *J. Light. Technol.* **33**, 2 (2015).

19. S.H. Badri and M.M. Gilarlue, "Coupling Between Silicon Waveguide and Metal-Dielectric-Metal Plasmonic Waveguide with Lens-Funnel Structure," *Plasmonics* **15**, 3 (2020).

20. A. Yariv, "Coupled-Mode Theory for Guided-Wave Optics," *IEEE J. Quantum Electron.* **9**, 9 (1973).

21. A. Hardy and W. Streifer, "Coupled Mode Theory of Parallel Waveguides," *J. Light. Technol.* **3**, 5 (1985).

22. A. Melikyan and P. Dong, "Adiabatic mode converters for silicon photonics: Power and polarization broadband manipulators," *APL Photonics* **4**, 3 (2019).

23. Z. Wang and D. Dai, "Ultrasmall Si-nanowire-based polarization rotator," *J. Opt. Soc. Am. B* **25**, 5 (2008).

24. H. Guan, A. Novack, M. Streshinsky, R. Shi, Q. Fang, A.E.-J. Lim, G.-Q. Lo, T. Baehr-Jones, and M. Hochberg, "CMOS-compatible highly efficient polarization splitter and rotator based on a double-etched directional coupler," *Opt. Express* **22**, 3 (2014).

25. P.-J. Chiang and T.-T. Shih, "Analysis of Leakage Loss in Silicon Photonics with Finite

*Gain Compensation," IEEE Photonics J. 9, 5 (2017).*

26. Farhan Bin Tarik, Nazmus Sakib and Judson D. Ryckman, "Efficient optical coupling to ultra-low mode area silicon v-groove waveguides," IEEE Photonics Conference (2019).

27. Farhan Bin Tarik and Judson D. Ryckman, "Fabrication tolerant coupling between silicon strip and subdiffraction V-groove waveguide," Optics Continuum, Vol 1, Issue 2, pp. 453-461 (2022).

# REALIZING ROBUST OPTICAL PHYSICAL UNCLONABLE FUNCTION FROM QUASICRYSTAL INTERFEROMETER

## 3.1 Introduction

Physical unclonable function (PUF) has emerged as a promising and important security primitive for use in modern systems and devices, due to their increasingly embedded, distributed, unsupervised, and physically exposed nature. Disorder and entropy are pervasive characteristics of nature and can be harnessed by physical unclonable functions (PUFs)<sup>1-4</sup> or random number generators<sup>5,6</sup>, to achieve significantly higher levels of hardware and/or information security than conventional methods. Manufacturing process variations are among the most technologically relevant forms of such randomness and are the primary means by which PUFs extract their chip-unique signatures<sup>1-3,7-9</sup>.

### 3.1.1 Physical Unclonable Function (PUF)

Physical unclonable function (PUF), sometimes also called physically unclonable function, is a physical entity that is embodied in a physical structure and is easy to evaluate but hard to predict. A physical unclonable function (sometimes also called physically unclonable function, which refers to a weaker security metric than a physical unclonable function), or PUF, refers to a physical object that for a given input and conditions (challenge), provides a physically defined "digital fingerprint" output (response) that serves as a unique identifier, most often for a semiconductor device such as a microprocessor. PUFs are most often based on unique physical



variations which occur naturally during semiconductor manufacturing. A PUF is a physical entity embodied in a physical structure. Today, PUFs are usually implemented in integrated circuits and are typically used in applications with high security requirements, more specifically cryptography. Recently, classical time-varying PUFs have been applied in secure communications<sup>10</sup> and in schemes obtaining perfect secrecy cryptography<sup>11</sup>. In another highly demanded application, PUFs have emerged as promising security primitives for authentication and identification throughout the untrusted supply chain.

### 3.1.2 Optical Physical Unclonable Function

Optical speckle patterns are famous for their complexity and uniqueness. Here, entropy is harvested and fabrication variations create a random, unclonable device fingerprint, popularly known as physical unclonable function or in short, PUF. It is important to realize that a PUF should be close to truly random in nature across different devices, known as ‘inter-chip’ variation; while operating in a robust manner over a wide range of environmental conditions called ‘intra-chip’ variation. Earlier, optical PUFs were proposed using light scattering off diffuse surfaces. At present, random and disordered photonic systems, or speckle patterns from multiple fibers are the more conventional physical unclonable functions as illustrated in Fig. 3.1.

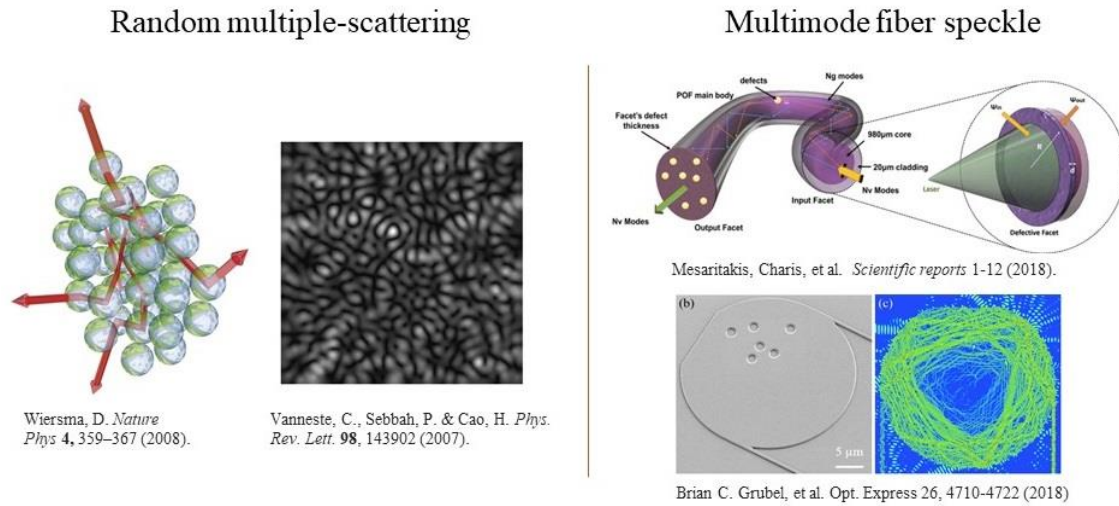


Fig. 3.1: Conventional optical PUF structures: realized from random multiple-scattering and multimode fiber speckle

Much of the technological progress in PUFs over the last fifteen plus years has come in complementary metal oxide semiconductor (CMOS) micro- and nanoelectronics<sup>12–16</sup>. However, interest in developing PUFs for hardware and information security applications has recently rapidly expanded to almost all areas of physical science including investigations based on chemical methods<sup>17</sup>, quantum tunneling<sup>18</sup>, disordered nanomaterials<sup>19–21</sup>, magnetic media<sup>22</sup>, and even biological species<sup>23</sup>. Attractively, the immense information capacity and rich physics of photonic systems offer the prospect of both passive or active security devices operating in classical and quantum regimes<sup>1,24,25</sup>. Moreover, highly complex and distributed multiple-scattering optical systems with high fabrication sensitivities can be very difficult to model or trim. Thus, the question remains open as to whether emerging technology could enable successful physical or machine learning attacks on emerging optical PUFs<sup>26</sup>, as has been demonstrated in specific types of non-optical silicon PUFs<sup>27–29</sup>.

### 3.2 Approach Towards Robust Optical PUF

In general, a PUF should be close to truly random in nature across different devices (so-called ‘inter-chip’ variation), while operating in a robust manner over a wide range of environmental

conditions (so-called ‘intra-chip’ variation). In the optical domain, speckle patterns are famous for their high complexity and uniqueness which arise from underlying photonic disorder, making them well suited for generating strong ‘inter-chip’ variation. However, as illustrated in Fig. 3.2(b), speckle phenomena from conventionally disordered photonic devices is notoriously sensitive to probing and environmental variations. Thus optical PUFs realized from laser speckle patterns suffer from high ‘intra-chip’ variation and are generally not robust nor widely considered to be a scalable technology, as they require precisely controlled optical alignment, tilt, polarization, temperature, and stable 2D spatially resolved optical imaging to measure and verify<sup>1,3,30</sup>. To realize a robust and scalable PUF technology, it remains imperative to enhance ‘inter-chip’ variation while simultaneously minimizing ‘intra-chip’ variation. Hence, emphasis must be placed on obtaining signatures which are highly visible, easy to measure in scale, computationally efficient to analyze, and robust over a range of measurement and/or environmental conditions.

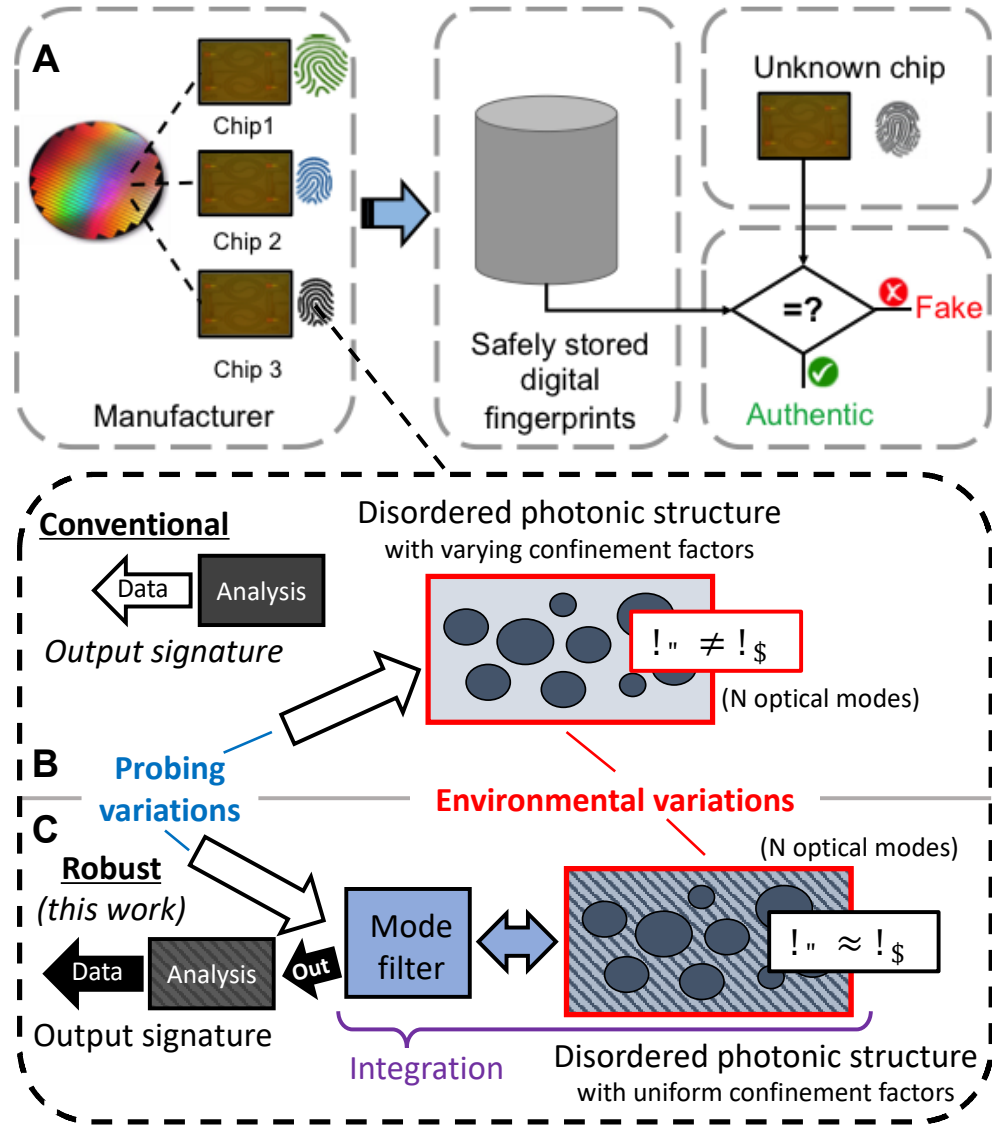


Fig. 3.2. High level overview. (A) A typical PUF authentication scheme, and overview of: (B) a conventional optical PUF, and (C) a robust optical PUF (the type introduced and demonstrated in this work). Here robustness refers to achieving immunity against probing and environmental variations

Confining light in a waveguide on the surface of a chip is an alternative method of probing spatial randomness, and could be performed in a highly integrated fashion without imaging or discrete sampling of arrayed devices, while storing an enormous amount of information in the frequency or impulse response. Along this vein, on-chip photonic PUFs have recently been investigated

using chaotic optical micro-resonators<sup>31,32</sup>. The optical chaos effect relies on extreme sensitivity to initial conditions, which dramatically alters the near field speckle patterns formed from a large number of spatial modes with varying  $Q/V$ . However, these modes also generally exhibit variable modal confinement factors  $\sqrt{\gamma_n}$  (matter-light interaction) with the constituent optical media, where the confinement factor may be defined as:

$$\gamma_n = \frac{\int_{active} \epsilon(\vec{r}) |E_n(\vec{r})|^2 dV}{\int \epsilon(\vec{r}) |E_n(\vec{r})|^2 dV} . \quad (3.0)$$

Hence, the various modes may be variably perturbed in frequency according to  $\Delta\omega_n/\omega_n = -(\Delta n/n_g)\gamma_n$ , where  $\Delta n$  is the index perturbation and  $n_g$  is the group index of the medium subject to perturbation. This renders such devices inherently very sensitive to all conditions, including both fabrication and environmental fluctuations such as temperature variations or non-linear effects<sup>31-33</sup>. On the other hand, Rayleigh backscatter from single-mode fiber or single-mode waveguide roughness naturally provides very stable and reliable random signatures. By supporting only a single-transverse mode with uniform confinement factor  $\sqrt{\gamma_n}$ , the random frequency response of such devices does not ‘evolve’ but rather is shifted deterministically in response to environmental stimuli such as temperature, strain, or aging<sup>34,35</sup>. Such backscatter signatures are however inherently very weak (poor visibility), requiring time domain or frequency domain backscatter interferometry to detect, and cannot be applied in transmission. Addressing all of these issues is critical to unlocking the promise of PUF technology and advancing both classical and quantum hardware security. Moreover, as integrated photonics continues to scale and become more intimately intertwined with both CMOS<sup>36</sup> and high volume datacom applications<sup>37</sup>, powerful new opportunities arise, such as the prospect for photonic security systems-on-a-chip or optical hardware enabled encryption of communication links.

Here we introduce and demonstrate a robust optical PUF constructed from silicon photonic circuitry which can readily be interrogated from industry standard wafer-scale fiber-optic probing and yields random, highly visible, and unclonable signatures with distinct features that are immune to probing and environmental variations. The robustness of our high level approach, illustrated in Fig. 3.2C, is realized through the combination of several unique aspects. First, co-integration of a mode-filter and disordered photonic structure is employed to suppress the effect of probing variations. Secondly, we developed a photonic design which achieves very high sensitivity toward ‘weak’ perturbations (see Approach); and in the photonic design all modes exhibit approximately the same confinement factor in silicon ( $\gamma_n \approx \gamma_m$ ). This preserves the PUF’s complex and non-deterministic signature in response to environmental thermo-optic variations as all spectral features shift together according to  $\Delta\omega_n/\omega_n = -(\Delta n/n_g)\gamma_n$ , where  $\Delta n$  is the thermo-optic index change and  $n_g$  is the group index of silicon (see Supplementary Information for additional detail). Lastly we demonstrate application of feature extraction using wavelet analysis<sup>38,39</sup>, to enable efficient and robust device authentication and identification. We also carry out conventional Hamming distance authentication of our PUFs in different settings and contrast our device with the random signatures of clonable (insecure) device designs manufactured in the same process.

### 3.2.1 Transfer matrix approach to disorder in a 1D multiple-scattering system

To describe 1D multiple scattering in a method which can include simulated randomness, we developed a modified form of the transfer matrix method<sup>61</sup>. The forward and backward propagating electric fields at the start ( $s = 0$ ) and end ( $s = l_m$ ) of a given waveguide segment,  $m$ , of length  $l_m$  are related to each other by the expression:

$$\begin{bmatrix} E_{m,0}^+ \\ E_{m,0}^- \end{bmatrix} = \mathbf{P}_m \begin{bmatrix} E_{m,l_m}^+ \\ E_{m,l_m}^- \end{bmatrix}, \quad (3.1)$$

where  $\mathbf{P}_m$  denotes the propagation matrix accounting for the accumulation of phase in the forward and backward directions:

$$\mathbf{P}_m = \begin{bmatrix} e^{-i\psi_m(\lambda)} & 0 \\ 0 & e^{i\psi_m(\lambda)} \end{bmatrix}. \quad (3.2)$$

The phasor argument,  $\psi_m(\lambda)$ , which describes propagation in the layer is importantly: (1) a complex quantity, (2) wavelength dependent, and (3) calculable from an integration of the local complex wave vector along the segment path as:

$$\psi_m(\lambda) = \frac{2\pi}{\lambda} \int n_{eff,m}(\lambda, s) ds + \frac{i}{2} \int \alpha_m(\lambda, s) ds. \quad (3.3)$$

Here  $n_{eff,m}(\lambda, s)$  is the waveguide's local effective index along the segment path and  $\alpha_m(\lambda, s)$  is the local attenuation coefficient (i.e. arising from sidewall roughness and Rayleigh scattering). The effective index is a function of waveguide width and is sensitive to fabrication variations on the nanometer scale,  $\frac{dn_{eff}}{dw} \sim 1.5 \times 10^{-3} [RIU/nm]$  @ 1550 nm (note: in the slow light regime, this sensitivity is further enhanced). Fabrication variations, distributed along the waveguide path, distort the local effective index away from the expected value for the segment (note: the expected value is assumed to account for the global, or average, critical dimension (CD) bias of a given process). The real part of  $\psi_m$ , which describes the local phase, can be re-expressed in terms of the expected value and the random deviation of effective index as:

$$Re[\psi_m(\lambda)] = l_m \frac{2\pi}{\lambda} (\langle n_{eff,m}(\lambda) \rangle + \delta n_m \cdot Rand_{1,m}) \quad (3.4)$$

where  $\delta n_m$  is the maximum possible effective index deviation for the segment and  $Rand_{1,m}$  is a random number over the interval  $[-1, 1]$  with probability distribution which is assumed to be uniform. This approach allows waveguide and material dispersion to be embedded within the model, rather than ignored as in alternative methods<sup>61</sup>. Similarly, the imaginary part of  $\psi_m$ , which describes the local attenuation coefficient, can be re-expressed as:

$$Im[\psi_m(\lambda)] = l_m \frac{i}{2} (\langle \alpha_m(\lambda) \rangle + \delta \alpha_m \cdot Rand_{2,m}) \quad (3.5)$$

where  $\delta \alpha_m$  is the maximum possible change in attenuation coefficient for the segment and  $Rand_2$  is a randomly generated number over the interval  $[0, 1]$  independent from  $Rand_1$ . Since the waveguide is theoretically lossless and losses are introduced by random backscatter, we choose to set  $\langle \alpha_m(\lambda) \rangle = 0$  and then define  $\delta \alpha_m$  such that an average attenuation coefficient  $\delta \alpha_m / 2$  corresponds to the experimentally measured average propagation loss.

In addition to affecting the characteristics of wave propagation, local fabrication variations also distort the Fresnel reflection and transmission coefficients at the interface between waveguide segments. The transmission and reflection of forward and backward propagating waves can be described by the expression:

$$\begin{bmatrix} E_{m-1}^+ \\ E_{m-1}^- \end{bmatrix} = \mathbf{I}_{m-1,m} \begin{bmatrix} E_m^+ \\ E_m^- \end{bmatrix}, \quad (3.6)$$

where  $\mathbf{I}_{m-1,m}$  is the interface matrix defined as

$$\mathbf{I}_{m-1,m} = \frac{1}{t_{m-1,m}} \begin{bmatrix} 1 & r_{m-1,m} \\ r_{m-1,m} & 1 \end{bmatrix}. \quad (3.7)$$



Here we define the Fresnel coefficients using the same random effective index variation embedded into Eq. (3.4):

$$r_{m-1,m}(\lambda) = \frac{\langle n_{eff,m-1}(\lambda) \rangle + \delta n_{m-1} \cdot Rand_{1,m-1} - (\langle n_{eff,m}(\lambda) \rangle - \delta n_m \cdot Rand_{1,m})}{\langle n_{eff,m-1}(\lambda) \rangle + \delta n_{m-1} \cdot Rand_{1,m-1} + (\langle n_{eff,m}(\lambda) \rangle + \delta n_m \cdot Rand_{1,m})}, \quad (3.8)$$

$$t_{m-1,m}(\lambda) = \frac{2(\langle n_{eff,m-1}(\lambda) \rangle + 2\delta n_{m-1} \cdot Rand_{1,m-1})}{\langle n_{eff,m-1}(\lambda) \rangle + \delta n_{m-1} \cdot Rand_{1,m-1} + (\langle n_{eff,m}(\lambda) \rangle + \delta n_m \cdot Rand_{1,m})}. \quad (3.9)$$

With these propagation and interface matrices so defined, a standard transfer-matrix method<sup>61</sup> can be used to model transmission and reflection for a multiple-scattering device of any nominal design. The complex s-parameters describing the reflection/transmission amplitude and phase are then extracted for both forward and reverse excitation of randomized spiral quasicrystals and fed into a scattering matrix simulator (Lumerical Interconnect) to simulate the entire quasicrystal interferometer (QCI).

### 3.2.2 The role of confinement factor in spectral signature stability over temperature

The frequency shift of the  $n^{th}$  optical mode in a given system, can be expressed using variational methods as<sup>62</sup>:

$$\frac{\Delta\omega_n}{\omega_n} = -\frac{\int \langle \Delta u_n \rangle dV}{\int \langle u_n \rangle dV} \quad (3.10)$$

where  $\langle u_n \rangle$  is the time averaged electromagnetic energy density,  $u_n$ , and  $\langle \Delta u_n \rangle$  is the time averaged perturbation in electromagnetic energy density. The electromagnetic energy density can be written as:

$$u_n = u_{E,n} + u_{H,n} = \frac{1}{2}[\mathbf{D} \cdot \mathbf{E} + \mathbf{H} \cdot \mathbf{B}] \quad (3.11)$$

For non-magnetic devices, environmental variations (matter-light interactions) perturb only the electric field energy density  $u_{E,n}$ , owing to the perturbations being isolated to the permittivity.

When integrated over all space and averaged in time we can replace the denominator of 3.1 with  $\int \langle u_n \rangle dV = 2 \int \langle u_{E,n} \rangle dV$ . The numerator meanwhile may be re-expressed as:

$$\int \langle \Delta u_n \rangle dV = \int \langle \Delta u_{E,n} \rangle dV \quad (3.12)$$

For a uniform refractive index perturbation applied only to some ‘active’ volume (e.g. a thermo-optic index change applied to the high index material) we may write:

$$\int \langle \Delta u_{E,n} \rangle dV = \frac{2\Delta n_{active}}{n_{g,active}} \int_{active} \langle u_{E,n} \rangle dV \quad (3.13)$$

Eq. 3.1 can thus be rewritten as:

$$\frac{\Delta \omega_n}{\omega_n} = -\frac{\Delta n_{active}}{n_{g,active}} \frac{\int \langle u_{E,n} \rangle dV}{\int \langle u_{E,n} \rangle dV} = -\frac{\Delta n_{active}}{n_{g,active}} \gamma_{active,n} \quad (3.14)$$

The fractional frequency shift of the  $n^{th}$  mode is therefore proportional to the change in refractive index and a “confinement factor”  $\gamma_{active,n}$ , which may be expressed as:

$$\gamma_{active,n} = \frac{\int_{active} \epsilon(\vec{r}) |E_n(\vec{r})|^2 dV}{\int \epsilon(\vec{r}) |E_n(\vec{r})|^2 dV} \quad (3.15)$$

It should be emphasized that thermo-optic stimuli can easily perturb a resonant frequency by a magnitude much larger than its full-width half maximum and much larger than the nearest mode to mode frequency spacing, i.e. in general it is likely that in practice  $|\Delta \omega_n| \gg \omega_{fwhm,n}$  and  $|\Delta \omega_n| \gg |\omega_{n+1} - \omega_n|$ . If an optical device has many resonant modes contributing features to its spectrum, then the optical spectrum will ‘evolve’ or be reconfigured (i.e. to generate a new signature) if  $\gamma_{active,n}$  is not a stable or very slowly varying function of the mode frequency. To ensure a stable spectrum pattern (which is allowed only to shift or stretch, but not to evolve), and therefore a stable PUF signature, it is therefore necessary to ensure  $\gamma_{active,n}$  is approximately constant or slowly and weakly varying across all modes.

For a 3D waveguide based device, the confinement factor could further be separated into longitudinal and transverse confinement factors. Therefore both the longitudinal and transverse confinement factors must be approximately constant or slowly and weakly varying to obtain a PUF signature which is stable over temperature. To ensure these requirements are met, we select a single transverse mode waveguide which is then very weakly modulated in its width along the longitudinal coordinate. A multi-mode waveguide would naturally have highly variable transverse confinement factors and could not satisfy the above requirement. Similarly, a strongly modulated index profile along the longitudinal coordinate (as in high index contrast photonic crystals) would result in large variations in the longitudinal confinement factor from mode to mode. Similarly, highly multimode microdisks and other types of on-chip resonators often naturally support many modes with a wide variation in their confinement factors. Such platforms are inherently unable to guarantee stable optical signatures in response to thermo-optic stimuli.

### 3.3 Modeling, Fabrication and Measurement

#### 3.3.1 Device Modelling

To model the potential characteristics of random silicon photonic PUFs, we developed a transfer matrix model incorporating random parameter variations to derive the complex s-parameters of randomized SBRs with varying degrees of disorder. These s-parameters (i.e. amplitude and phase spectra for forward and reverse excitation) are then embedded into a scattering matrix simulator (Lumerical Interconnect) which also accounts for the y-branches, routing waveguides, and loop mirrors.

#### 3.3.2 Fabrication and Measurement

Device fabrication and testing was carried out through the SiEPIC program<sup>60</sup>. Structures were fabricated using standard 220 nm SOI via 100keV electron beam lithography and reactive ion

etching at the University of Washington, while automated grating coupled device measurements were performed at The University of British Columbia. A tunable laser (Agilent 81600B) and optical power meter (Agilent 81635A) were used to capture device spectra over the range 1500-1600 nm in 10 pm steps.

### 3.4 The QCI PUF

#### 3.4.1 Device Architecture and Characteristics

Our integrated silicon photonic PUF is depicted in Fig. 3.3. Unlike free-space or multimode waveguide/fiber optical PUFs<sup>1,3,30</sup>, our PUFs interface with disorder in a stable fashion (i.e. Fig. 3.2C) through a co-integrated mode filter consisting of TE polarization grating couplers<sup>40</sup> and single-mode waveguides<sup>41</sup>. This design guarantees robust modal selectivity<sup>42</sup> and immunizes the devices against variations in polarization and spatial/angular alignment. The rest of the design is motivated to amplify the device's sensitivity to 'weak' disorder, while simultaneously suppressing the effect of environmental variations on device unique features. Here, we accomplish this through the introduction of a quasicrystal interferometer (QCI) with a weakly modulated index profile in a Michelson type configuration. Our QCI importantly breaks the translational symmetries exhibited in standard silicon photonic circuitry by using a multi-periodic grating with a slowly varying and non-uniform radius of curvature. This offers access to the unique physics and analyticity breaking offered by quasicrystals and 1D Aubry-André systems, including their distinct characteristics in response to disorder<sup>43–46</sup>. The weak index modulation meanwhile, ensures approximately constant or slowly varying confinement factor in silicon for all modes.

In our devices, fabrication variations are assumed to primarily stem from local nanoscale variations in waveguide width and surface roughness. To capture the effect of these variations

with high sensitivity and visibility, and to not allow them to average out into very few parameters (as in a simple interferometer) or manifest as an ultimately very weak signal (as in waveguide Rayleigh backscatter), it is desirable to create a structure which supports multiple-scattering through the use of many discrete waveguide segments. However, the arrangement of the segments should not have perfect translational symmetry as in a crystal or distributed Bragg reflector (DBR). The properties of a DBR are generally very robust against weak perturbations such as nanoscale disorder owing to destructive interference, with only two narrow windows of enhanced sensitivity near the band edges. The use of linear DBRs instead of our spiral QCs would effectively make the device function like a symmetric single etalon Michaelson Gires-Tournois interferometer (MGTI)<sup>47</sup>. Further, locally breaking the translational symmetry of a DBR in a limited number of locations would effectively yield photonic crystal cavities which only probe disorder in those discrete locations, thus severely limiting the device complexity. Thus, we observe that the use of a QC which entirely lacks translational symmetry (aside from allowed rotational symmetries), naturally arises as a powerful solution to sensitively probing spatially distributed fabrication variations while fostering enhanced complexity.

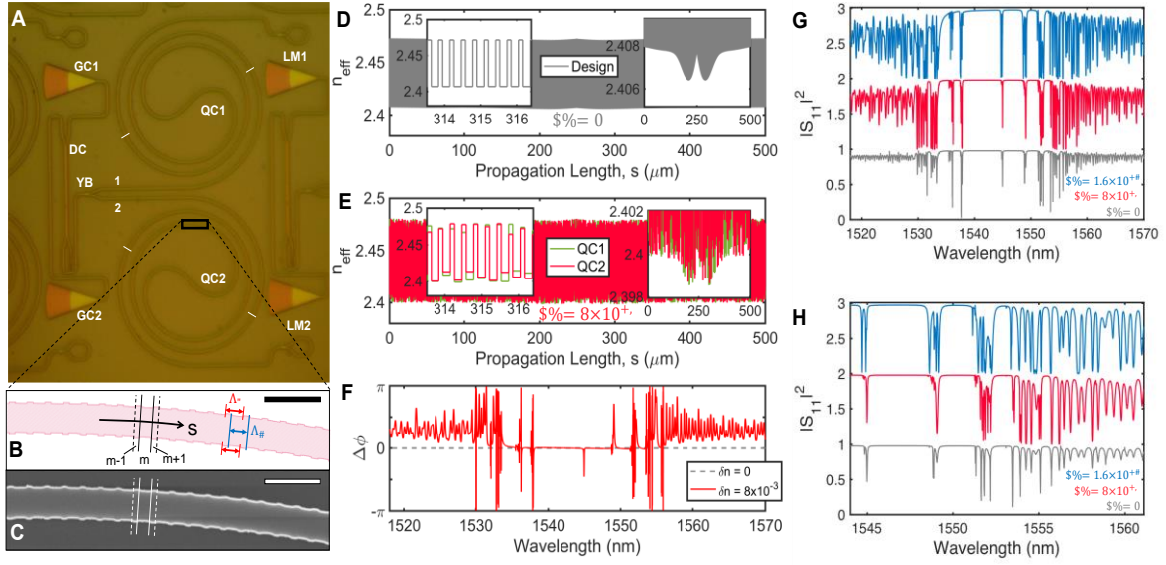


Fig. 3.3. Overview of photonic circuitry and quasicrystal interferometry. (A) Optical microscope image of the integrated silicon photonic QCI PUF architecture. Input/output grating couplers (GC1/GC2), single mode waveguides, and a 50:50 directional coupler (DC) enable pure mode filtering and stable QCI device measurement in transmission. A compact y-branch (YB) splits light into two symmetric arms, (1) and (2), routed to the spiral quasicrystal (QC) arms and loop mirrors (LM1/LM2). (B) Zoomed view of design and (C) SEM image of the curved QC and illustration of the  $m$ th segment considered in device modelling (scale bar = 1  $\mu\text{m}$ ). (D) Nominal QC effective index profile @ 1550 nm. (E) Example effective index profiles with random errors introduced, and (F) corresponding phase differences between the two arms. (G) Simulated QCI spectra (YB port reflectance) for nominal and random QCIs with varying disorder parameters, and (H) zoomed view of the same [66].

The arms of our QCI PUF consist of width modulated (500 nm  $\pm$  20 nm) single mode Si waveguides with nominal device thickness 220 nm cladded by  $\text{SiO}_2$ . The QCs each utilize a slowly varying radius of curvature spiral ( $R \approx 50\text{-}25 \mu\text{m}$ ), containing 500  $\mu\text{m}$  long multiperiod gratings formed by the superposition of gratings with periods  $\Lambda_1 = 316 \text{ nm}$  and  $\Lambda_2 = 317 \text{ nm}$ . Grating teeth (i.e. width equal to 520 nm) are placed at the intersection of  $\Lambda_1$  and  $\Lambda_2$  gratings by performing a Boolean *AND* function. When considered as a standalone component without disorder, the 1D QC forms longitudinal modes as a result of several effects, which are all related to breaking translational symmetry: (i) the low frequency band edge of the  $\Lambda_1$  grating forms a defect region within the overlapped band gap of the  $\Lambda_2$  grating, (ii) the high frequency band edge of the  $\Lambda_2$  grating forms a defect region within the overlapped band gap of the  $\Lambda_1$  grating, and (iii) additional defect modes are introduced owing to the weak gradual reduction of waveguide effective index with reducing radius of curvature<sup>48</sup>. The output of the QCs are routed to loop

mirrors which offer broadband reflectivity and supports the formation of higher order resonances owing to multi-pass effects. The initial onset of disorder is expected to introduce unique extended states fostering slow-light and resonantly enhanced transmission through the QC in the vicinity of the overlapping fundamental band gaps, while increasing disorder strength should foster the introduction of random localized states and optical resonances exhibiting unique spatial and spectral characteristics. In principle, the exact device design that is used can be flexible, but should ideally provide the following traits: (i) offer high complexity and require numerical methods to model even qualitatively, (ii) support the presence and formation of many spectrally and spatially isolated resonances, (iii) support regions of slow-light effects or high dispersion, (iv) be realized in a regime where fabrication variations constitute a non-negligible fraction of the critical dimensions, and (v) be comprised entirely of weakly modulated single transverse mode waveguides with approximately uniform confinement factors.

The predicted characteristics for QCIs with varying disorder,  $\delta n \geq 0$ , are shown in Fig. 3.3D-H. The designed width and radius of curvature modulation of the spiral quasicrystal arms yields a nominal effective index profile vs. propagation length (Fig. 3.3D) which is then locally and randomly distorted owing to spatially distributed fabrication variations (i.e. Fig. 3.3E). To model the potential effect of such fabrication variations, we apply a uniformly distributed random error of no more than  $\pm 5$  nm in waveguide width, corresponding to a maximum effective index error in any segment of  $\delta n = 8 \times 10^{-3}$ . These random fabrication variations are usually interpreted as ‘weak’ perturbations in the context of waveguide or photonic crystal backscatter<sup>49</sup>, and are indeed weak in the sense that they do not significantly perturb the transverse optical confinement factor in silicon. However, in our device where the effective index modulation is intentionally small,  $\Delta n \approx 6.5 \times 10^{-2}$ , and where there is a lack of perfect

translational symmetry, these ‘weak’ perturbations contribute significant disorder (i.e. >10% the effective index modulation of the unperturbed grating), both randomly perturbing existing states and introducing random extended and localized states into the spiral quasicrystal. This yields a highly complex and spectrally randomized phase difference between the arms (Fig. 3.3F) which can be converted into highly visible spectral fingerprints (Figs. 3.3G,H) using the Michelson configuration.

### 3.4.2 Approach towards Uniform Confinement

In a balanced and lossless interferometer with no phase errors, the reflection spectrum detected from the y-branch should theoretically measure as 100% across the entire spectrum. In our devices however, the waveguides have a finite propagation loss ( $\sim 2.4$  dB/cm) owing to sidewall roughness and bend loss, as well as passive insertion loss at the interfaces to/from the quasicrystals and loop-mirror y-branches. This loss is significantly enhanced in regions of optical resonance or band edges, becoming a form of coherent perfect loss when critically coupled to quasicrystal or higher order etalon modes<sup>50,51</sup>, and provides distinct features in the spectrum even for a perfectly symmetric and balanced QCI with no disorder,  $\delta n = 0$ . In effect, our QCI exploits randomization in both the amplitude and phase degrees of freedom to generate its unique signatures, while our photonic circuitry specifically constrains the transverse spatial-mode and polarization degrees of freedom to foster robustness.

Regarding environmental stability, it should be emphasized that thermo-optic stimuli can easily perturb a mode frequency  $\omega_n$  by a magnitude  $|\Delta\omega_n|$  much larger than its full-width half maximum and much larger than the nearest mode to mode frequency spacing – i.e. in general it’s likely that in practice  $|\Delta\omega_n| \gg \omega_{fwhm,n}$  and  $|\Delta\omega_n| \gg |\omega_{n\pm 1} - \omega_n|$ . If an optical device has



many resonant modes contributing features to its spectrum, then the optical spectrum will ‘evolve’ or be reconfigured to generate a different spectral fingerprint if the modal confinement factor in the thermo-optic medium,  $\overline{\gamma_n}$ , is not a uniform or very slowly varying function of the mode frequency  $\overline{\omega_r}$ . This can lead to extreme sensitivities to temperature, for example in certain multi-mode speckle devices where 50% decorrelation in the output speckle pattern has been observed in response to temperature variations of 0.16°C<sup>52</sup>. Unlike chaotic microcavity PUFs<sup>31,32</sup>, multi-mode speckle devices<sup>30,52</sup>, or strongly disordered photonic systems considered in other applications<sup>43,53,54</sup>, all of the modes in the QCI are engineered to exhibit nearly the exact same confinement factor in silicon via the single transverse mode that is supported and narrow +/- 20 nm waveguide width modulation that is utilized. This unique design ensures that thermo-optic effects fractionally perturb the frequency of all modes equally, thereby suppressing the effect of intra-chip variations and preserving the output device signature across temperature.

### 3.5 Results and Discussion

#### 3.5.1 Verification of Unclonability and Temperature Immunity

To experimentally demonstrate our devices, both QCI PUFs and single etalon DBR integrated MGTI reference devices were fabricated in a standard 220 nm device layer SOI platform (see Methods). Devices were then measured with a tunable laser under TE polarization using the fiber-to-chip grating couplers as illustrated in Fig. 3.3A. The double pass insertion loss of the directional coupler used to probe the QCI sets the minimum on-chip insertion loss to ~6 dB, rendering the devices easy to measure and align to in an automated testing environment, while the single mode waveguides and single polarization grating couplers render the devices immune to errors in spatial or angular alignment and polarization. To assess the impact of thermal/environmental variation, devices were measured at two temperature settings: setting

1) 23°C, and setting 2) 30°C (settings were measured ~48 hrs apart from one another). The +7°C temperature variation mimics the effect of a significant temperature drift which is expected to shift the wavelength for most of the PUF's spectral features by significantly more than their 3 dB linewidth.

Figs. 3.4A and 3.4C show the measured spectra of three triplicated integrated QCI PUFs (e.g. Fig. 3.3), fabricated in the same process and located next to each other on the same die. The designs of the triplicate structures are all exactly the same with no modifications. However, their optical spectra are entirely unique, effectively serving as a fingerprint for each device. The devices exhibit excellent visibility in grating-coupled transmission, with extinction ratios well in the ~5-30 dB range.

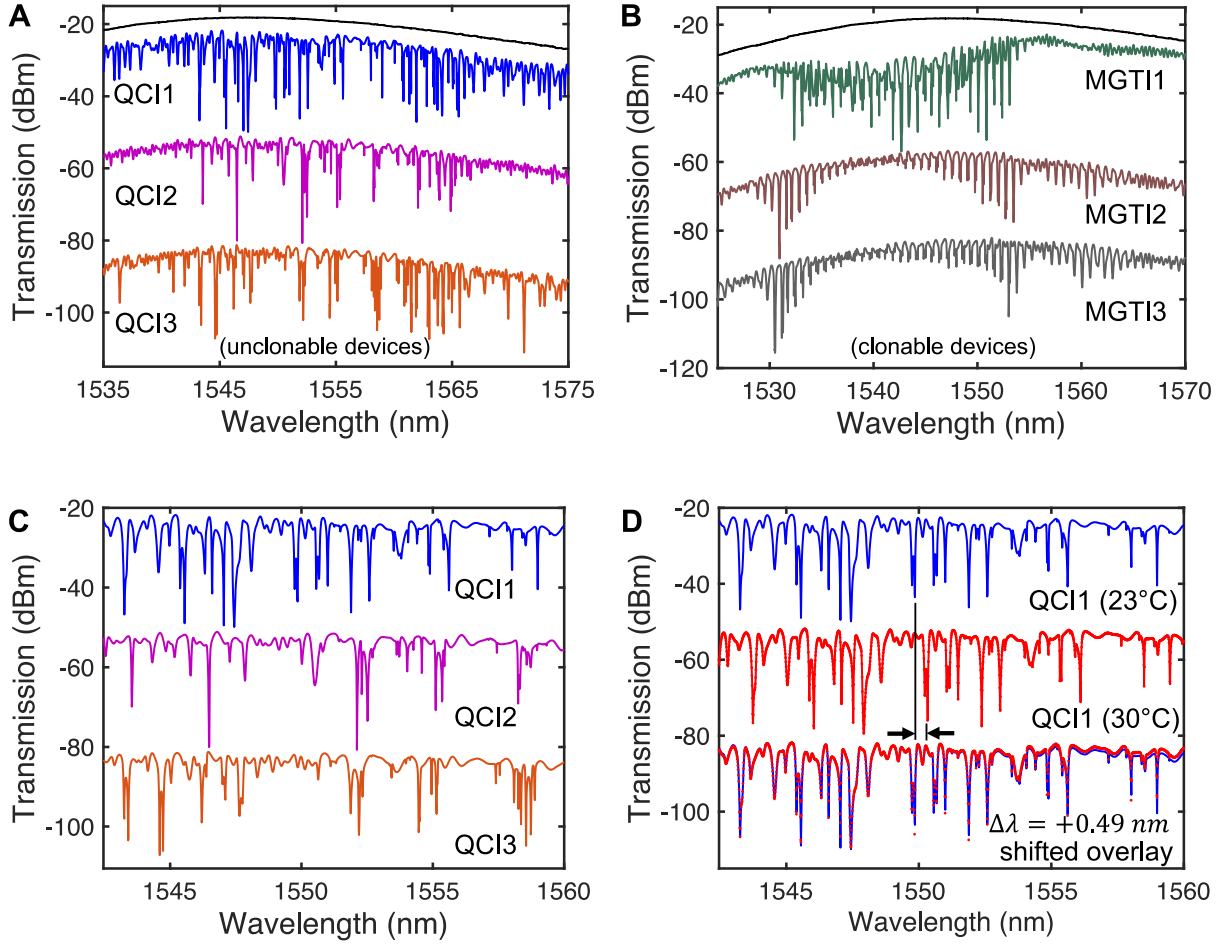


Fig. 3.4 Experimental transmission spectra for triplicated silicon photonic (A) QCI PUFs, and (B) single etalon DBR integrated MGTIs. Black curve corresponds to single pass directional coupler (DC) transmission. Probing of QCIs and MGTIs adds  $\sim 3$  dB insertion loss owing to double pass loss through the DC. Device 2/3 spectra are shifted on the y-axis for clarity. (C) Zoomed view of QCI PUF spectra showing device uniqueness. (D) Zoomed view of QCI1 spectra at both temperature settings, revealing a deterministic spectral shift [66].

In the same fabrication run, we also included triplicated single etalon MGTI designs wherein the spiral quasicrystals were replaced with a waveguide delay and simple DBR structure. The DBR length was  $\sim 23 \text{ }\mu\text{m}$  with a sidewall grating width modulation of  $500 \pm 80 \text{ nm}$ . The waveguide path length from the y-branch (YB) to the DBR was  $\sim 280 \text{ }\mu\text{m}$  and from the DBR to the loop mirror (LM) was  $\sim 340 \text{ }\mu\text{m}$ . Although the MGTI spectra are ‘randomized’ by fabrication induced phase errors, as visible by the difference in device-to-device spectrum variations from

Fig. 3.4B, the device spectra are not unclonable. In the single etalon MGTI devices, an analytical description and exact parameter fit of the device properties could be achieved since the distributed fabrication variations are simply averaged into very few device parameters (i.e. 2 values of DBR  $\kappa L$ , and 4 values of optical path lengths, effective/group indices, and optical losses). Over many process runs or iterations, the likelihood of repeating the same MGTI device signature twice (i.e. cloning) becomes very significant despite the randomness imparted into each device. In the QCI PUF device however, the distributed fabrication variations are locally captured in each unique segment of the 1D multiple-scattering waveguide which exponentially increases the device complexity and exponentially suppresses the probability of cloning.

Assuming fabrication errors in a given segment could be simply discretized to five values (i.e. width deviation of  $\pm 5$  nm in increments of 2.5 nm), the number of device permutations in an MGTI structure with 4 segments is only on the order of  $5^4 \approx 10^{2.8}$ , whereas our finite length QCI device has  $>6,000$  multiple-scattering segments resulting in more than  $5^{6000} \approx 10^{4193}$  possible unique physical device permutations. Hence, despite being qualitatively similar types of devices at an architectural level, the MGTI and QCI are exponentially different in terms of complexity.

Fig. 3.4D shows the transmission spectrum for an integrated QCI PUF measured at both temperature settings. All features in the spectral fingerprint of the device near 1550 nm are shifted in wavelength by  $\Delta\lambda \approx +0.49$  nm, in excellent agreement with the predicted thermo-optic sensitivity of the single-transverse mode silicon waveguides. This provides an experimental measurement of the confinement factor in silicon, determined to be  $\sim 0.884$ , and confirms that all modes of the QCI exhibit approximately the same confinement factor. Crucially, this provides evidence that the non-deterministic inter-chip characteristics are preserved and deterministically perturbed by temperature, as desired. Simulations suggest this deterministic spectral response to

temperature can be sustained for even larger temperature variations  $\Delta T = \pm 30^\circ\text{C}$ . However, if the modal confinement factors were not uniform, then randomized features corresponding to different modes would shift with different thermo-optic sensitivities and the spectrum would dynamically evolve in an unpredictable fashion, rather than simply shifting in response to temperature.

### 3.5.2 Waveguide loss data

An important parameter to consider in any silicon photonic structure is the waveguide loss. The loss can be classified as scattering loss (due to sidewall roughness), absorption loss (not present here), and radiative loss (in a bent waveguide). Both spiral and straight waveguide loss has been measured in our study. Fig. 3.5 shows a schematic representation of waveguide loss. As expected, the slope of power loss for spiral waveguide is steeper than that of straight waveguide owing to a combination of radiative and scattering loss. The spiral waveguide loss is therefore approximately  $\sim 2.4$  dB/cm.

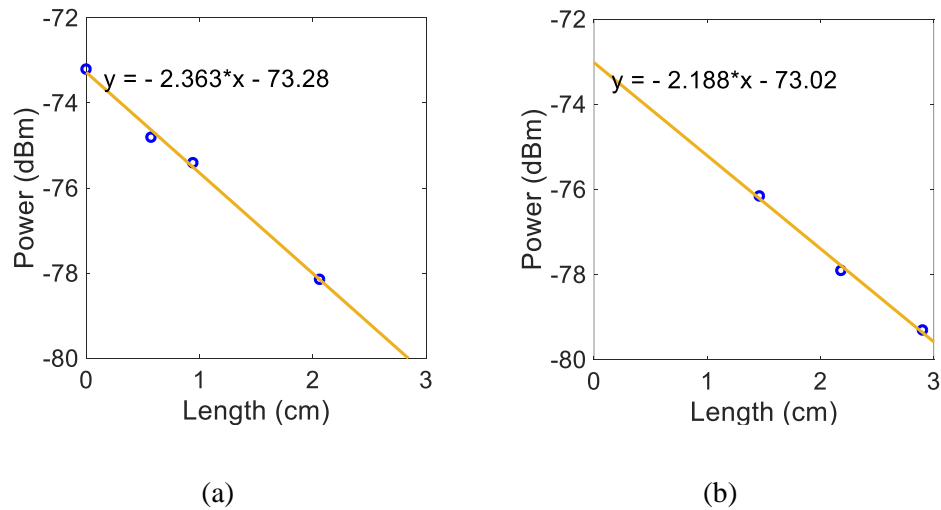


Fig.3.5 (a) Spiral and (b) straight waveguide loss determination via the cutback method

### 3.5.3 Hamming Distance Authentication Analysis

Over the years, Hamming analysis has been a state-of-the-art to verify secure authentication. As shown in Fig. 3.6, we first performed Hamming distance authentication analysis on the three QCI PUFs. In this computation, each raw spectrum is normalized to the directional coupler reference spectra and then converted to a binary sequence with  $>10,000$  bits. A central subset of 8,000 bits is then enrolled and computationally shifted relative to various test keys, at both temperature settings, to search for a match (i.e., Hamming distance  $< 0.3$ ), which is a strong indication of the authenticity. The results confirm the uniqueness of each PUF and validate authentication of each device at both temperature settings.

In general, directly using the raw output signals of the PUFs for authentication or

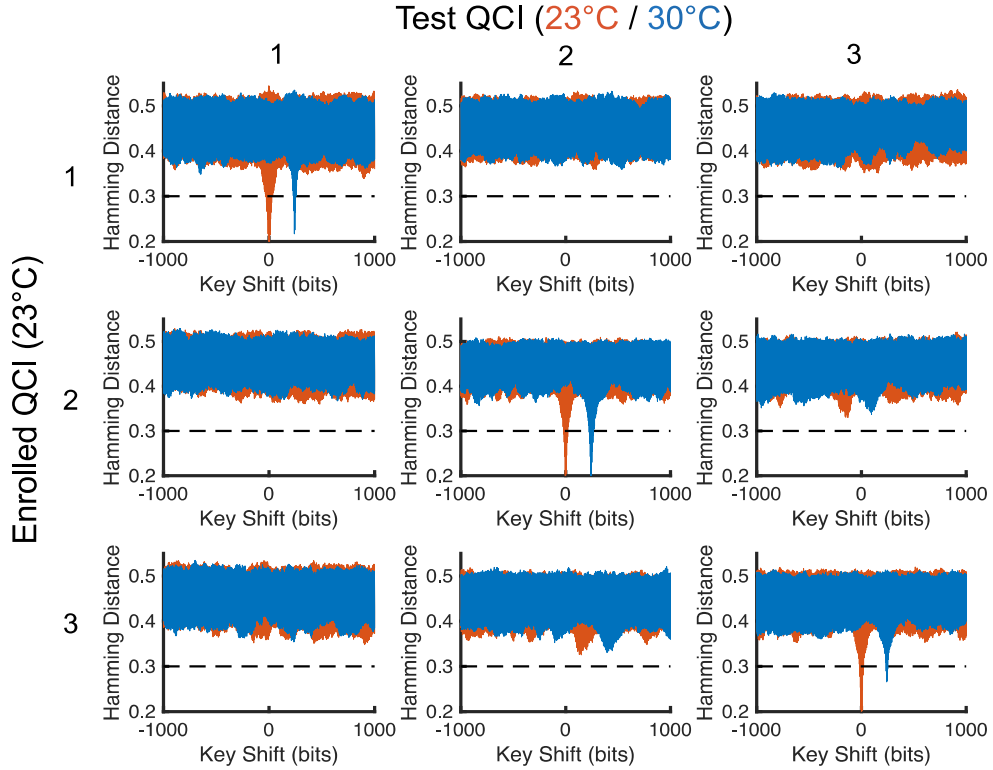


Fig. 3.6. Hamming distance authentication analysis for each silicon photonic QCI PUF at two temperature settings

identification is neither efficient nor robust. To this end, an entropy-harvesting method that can extract chip-unique features will significantly improve the overall performance and functionality of the proposed PUFs and enable scalable identification with large device libraries. The entropy of the spectra of the PUFs generally comes from two sources: inter-chip and intra-chip variations. Inter-chip variations are the intrinsic variations introduced during the fabrication, while intra-chip variations are caused by environmental changes or device aging<sup>8,55,56</sup>. Thus, in order to enhance both the uniqueness and reliability of the PUF signature, an ideal entropy-harvesting method should be able to leverage manufacturing process variations, while mitigating intra-chip variations<sup>8,55–58</sup>. This includes mitigating any residual probing and/or environmental variations in the grating coupler’s low frequency spectral envelope (Fig. 3.4A) or the PUF’s spectral fingerprint. In our experiments, we applied two types of techniques, i.e., feature extraction and correlation analysis, to illustrate the effectiveness of our integrated photonic PUFs.

#### 3.5.4 Device Identification through Feature Extraction and Wavelet Decomposition

For the feature extraction method, we use wavelets to decompose the signal. Fig. 3.7 shows an example of the wavelet decomposition of the raw output signal,  $s$ , for QCI1 along with part of the first level of decomposition for all three devices. The best results are observed when we use five-level decompositions (e.g.  $d_5$ ,  $d_4$ ,  $d_3$ ,  $d_2$ ,  $d_1$ ) with Fejer-Korovkin, Symlet, Reverse Biorthogonal wavelets<sup>59</sup>. The standard deviation and variance of corresponding sub-bands are then chosen as features. It can be clearly seen from both Fig. 3.7 and Table 3.1, which illustrates the Fejer-Korovkin derived features, that different devices yield distinct features. As indicated in Table 1, it is observed that the features of the QCI PUFs are stable, since the intra-chip variation is significantly less than the inter-chip variation.

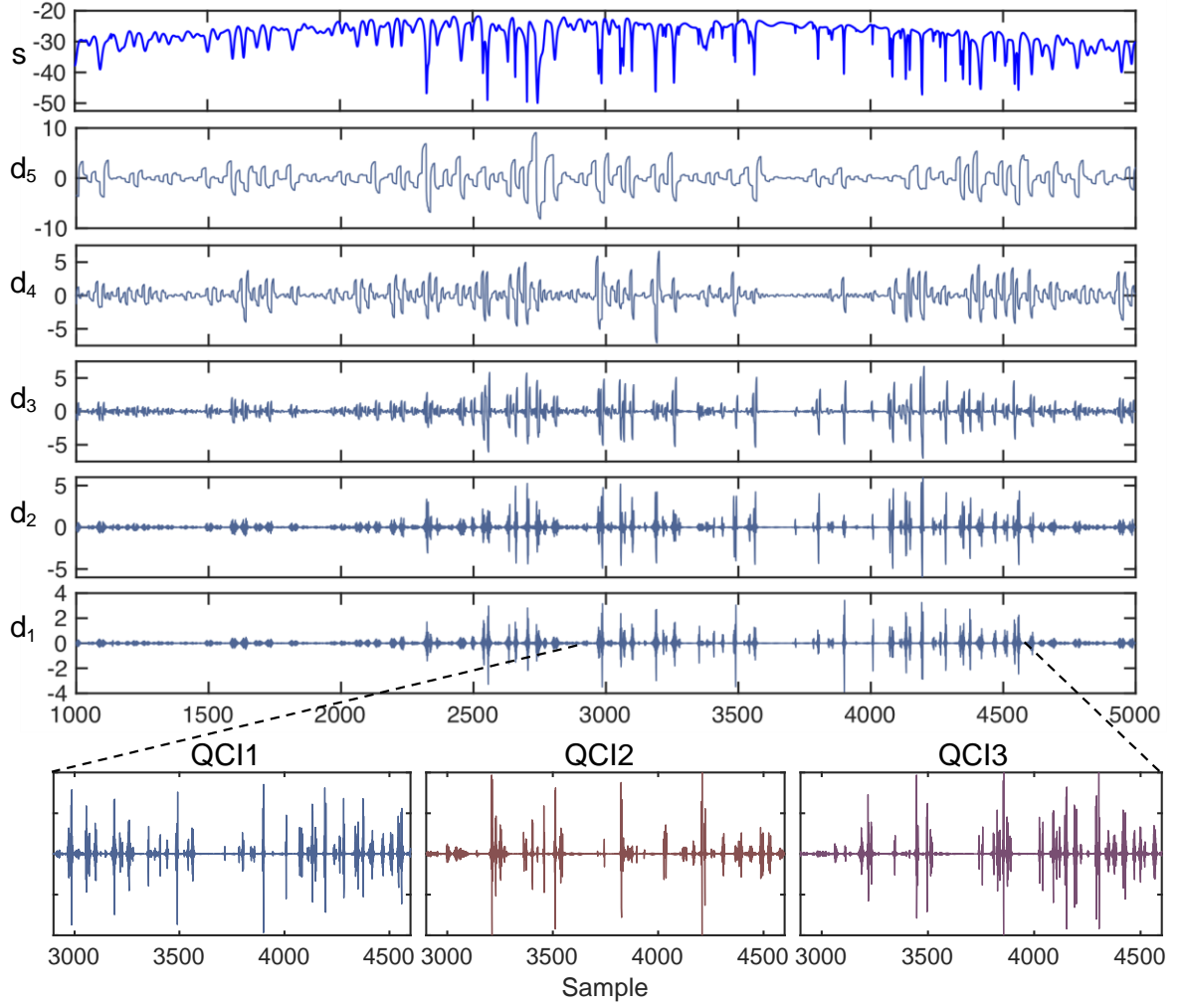


Fig. 3.7. Five-level decomposition of an output signal analyzed by Fejer-Korovkin wavelets. After decomposition, the devices can be distinguished effectively

Wavelets are special functions that have localized property with respect to both frequency and space variables. Wavelet transform basically decomposes the input signal in time and frequency plane. Equation below is the discrete wavelet transform (DWT) of input  $x(n)$ <sup>63,64</sup>:

$$y_i(n) = \sum_{k=-\infty}^{\infty} x(k) \times h_i(2^{i+1}n - k), \text{ for } 0 \leq i \leq m - 2, \quad (3.16)$$

$$y_{m-1}(n) = \sum_{k=-\infty}^{\infty} x(k) \times h_{m-i}(2^{m-1}n - k), \text{ for } i = m - 1, \quad (3.17)$$



The shifted and scaled version of “mother wavelet”  $h(n)$ ,  $\{h_i(2^{i+1}n - k) \text{ for } 0 \leq i \leq m - 1, -\infty < k < \infty\}$  are the basis functions, and  $y_i(n)$  are the wavelet coefficients<sup>63,64</sup>.

DWT periodically processes  $M$  input samples and generates  $M$  output samples at various frequency bands where  $M = 2^m$  and  $m$  is the number of wavelet levels. DWT is normally implemented in a tree structure. Each step contains two digital filters  $g(n)$  and  $h(n)$ , and two down-samplers with a factor of 2. The input sequence of  $s_{j-1}(n)$  is fed to both the high pass filter  $g(n)$  and the low pass filter  $h(n)$ . Let  $n$  and  $j$  be the sample index and the level index, the output signals can be computed as follows:

$$s_j(n) = \sum_k s_{j-1}(k)g(2n - k) = \sum_k g(k)s_{j-1}(2n - k), \quad (3.18)$$

$$w_j(n) = \sum_k s_{j-1}(k)h(2n - k) = \sum_k h(k)s_{j-1}(2n - k). \quad (3.19)$$

Device identification can be performed by enrolling the device under test’s features and carrying out an error analysis to identify the device features which yield the lowest mean squared error. Identification can be further strengthened by verifying agreement across different decompositions or complementary techniques such as a power spectral density derived signal correlation. Results for device identification are displayed in Table 3.2. Correct identification of our QCI PUFs are achieved in all cases, regardless of temperature setting, allowing us to conclude that each PUF will be distinguishable across temperature. For the clonable MGTI devices however, the features are not sufficiently unique and hence different wavelet decompositions mis-identify the enrolled device.

Device	Setting	Level1	Level2	Level3	Level4	Level5
QCI1	1 (23°C)	0.21	1.66	7.79	30.17	119.92
	2 (30°C)	0.25	1.53	7.98	30.07	106.47
QCI2	1 (23°C)	0.14	0.73	3.98	14.26	26.16
	2 (30°C)	0.10	0.84	3.57	13.30	32.24
QCI3	1 (23°C)	0.23	1.33	6.34	24.81	68.93
	2 (30°C)	0.24	1.36	6.20	24.00	54.79

Table 3.1. Example PUF features extracted from a five-level Fejer-Korovkin wavelet decomposition.

Device	Unclonable						Clonable					
	QCI1		QCI2		QCI3		MGTI 1		MGTI 2		MGTI 3	
Setting	1	2	1	2	1	2	1	2	1	2	1	2
Variance_fk ( $\times 10^2$ )	1.6	1.16	<b>0.01</b>	Enrolled	0.3	0.1	2.41	1.8	0.01	<b>~0.00</b>	0.2	Enrolled
Variance_rbio ( $\times 10^2$ )	0.8	1.59	<b>0</b>		0.1	0.2	0.41	<b>0.4</b>	1	0.76	0.5	
Variance_sym ( $\times 10^2$ )	1.5	2.04	<b>0.01</b>		0.2	0.3	0.96	2.1	11	0.63	<b>0.4</b>	
Correlation	0.8	0.76	<b>0.96</b>		0.7	0.7	0.65	0.7	0.78	<b>0.84</b>	0.8	

Table 3.2. Results of feature extraction and correlation analysis applied to device identification. The “unclonable” QCI PUFs achieve substantial inter-chip variations and are stable across different environmental conditions, while the inter-chip variations of the “clonable” design are not sufficient to identify the enrolled device.

### 3.6 Simulation / Analysis of a QCI PUF Over Temperature

To realize optical PUF authentication over temperature it’s imperative for a particular optical PUF to retain its inter-chip variation dominated signature over temperature. This requires achieving uniformity in the confinement factor of all modes. Here, we present numerical simulation of a random QCI PUF, herein called “sim1”, which is designed to achieve uniformity in both the longitudinal and transverse confinement factors, similar to the nominal experimental

design discussed in the previous section. In this simulation, we assume that the disordered waveguide effective index is thermo-optically perturbed according to the expression:

$$\Delta n_{eff} = \Delta n_{Si,TO} \frac{n_g}{n_{Si}} \gamma_{Si} \quad (S5.1)$$

where  $\Delta n_{Si,TO} = \Delta T \frac{\partial n_{Si}}{\partial T}$  is the thermo-optic index change of silicon, occurring with a thermo-optic coefficient  $\sim 1.84 \times 10^{-4}$  RIU/K;  $n_g$  is the nominal group index of a single-transverse mode 500 nm wide, 220 nm tall waveguide (i.e.  $\sim 4.2$ ), and  $n_{Si}$  the material refractive index (i.e.  $\sim 3.5$ ); and  $\gamma_{Si}$  is the confinement factor of the mode (i.e.  $\sim 0.9$  in our designs). The integrated optical PUF is simulated in three temperature settings, first at a reference temperature  $\Delta T = 0^\circ\text{C}$ , then over a wide  $\Delta T = \pm 30^\circ\text{C}$  temperature variation. Thus, an extensive  $60^\circ\text{C}$  temperature range is considered. To our knowledge this is the first time such a wide temperature range has been considered in an optical PUF.

Fig. 3.8 shows the spectra of our simulated PUF (“sim1”) for different temperature settings. This example is well into the regime of a ‘large’ response, i.e. where  $|\Delta\omega_n| \gg \omega_{fwhm,n}$  and  $|\Delta\omega_n| \gg |\omega_{n\pm 1} - \omega_n|$ . However, the spectral features of all modes are clearly observed to shift together, which is attributed to the approximately uniform confinement factor exhibited by all modes. In principle the spectra are not perfectly shifted along the x-axis but stretched (scaled) according to the relationship of Eq. 3.5. Thus a simple Hamming analysis which performs a binary key shift, is able to achieve authentication as shown in Fig. 3.8(c) – but is not nearly as robust as the wavelet based feature extraction method we demonstrate in Table 3.2 and highlight in Table 3.1.

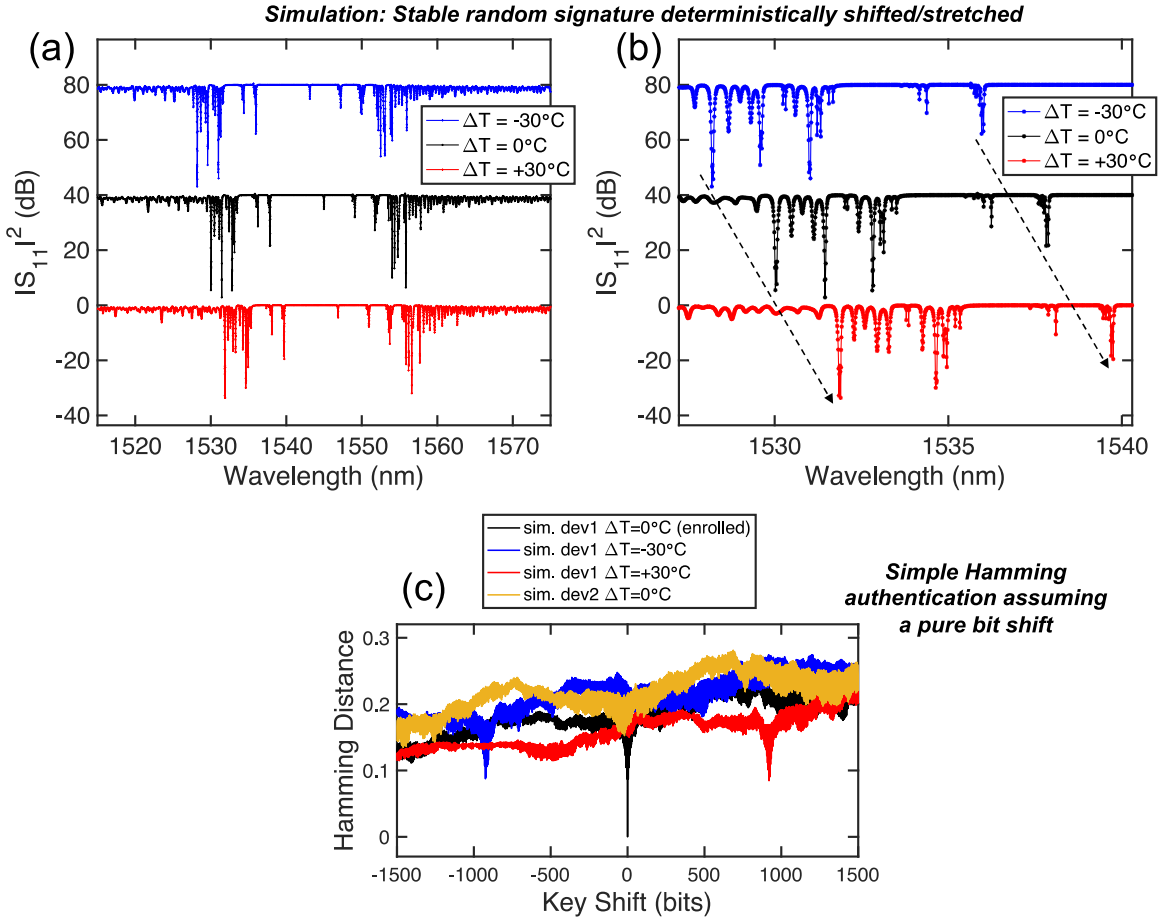


Fig. 3.8. (a) Simulated PUF spectra over  $\pm 30^\circ\text{C}$  temperature variation, (b) zoomed view which clearly shows all spectral features in wavelength shift together thereby retaining the overall PUF signature. Spectra are off-set on y-axis by 40 dB for clarity. (c) Simple Hamming analysis of binarized PUF spectra as a function of binary key shift. While not as robust as our signature analysis (Table 3.1), this Hamming analysis is able support device authentication

As noted in the main text and above, directly using the raw about signals for authentication or identification is not efficient nor robust. Here we apply our five level wavelet decomposition feature extraction method to the simulated PUF “sim1” spectra over temperature. Table 3.3 shows the resulting features and five level wavelet analysis. We also present the identification analysis in terms of mean squared error between the enrolled and test signals in Table 3.4. This shows the reliability of the device since the intra-chip variations are less than the inter-chip variations.

Device	Setting	Level1	Level2	Level3	Level4	Level5
“sim1”	0 C	0.20	0.94	3.64	14.88	34.35
	30 C	0.16	0.74	2.88	15.88	21.48
	-30 C	0.20	0.75	4.64	8.040	42.89

Table 3.3. The variance of “sim1” PUF’s output signals for each decomposition level.

Device	“sim1”		
Setting	-30	0	+30
Variance_fk ( $\times 10^3$ )	0.1	0.03	Enrolled
Variance_rbio ( $\times 10^3$ )	0.02	0.00	
Variance_sym ( $\times 10^3$ )	0.05	0.00	

Table 3.4. Mean squared error between enrolled signals and the other signals.

### 3.7 Summary

In this work, we introduced and demonstrated photonic circuitry employing single mode TE polarization mode filtering alongside a weakly modulated quasicrystal interferometer (QCI) as a means for realizing a robust physical unclonable function (PUF). Similar to the original vision of the first optical scattering PUFs, our device probes spatially distributed randomness but realizes it in a highly integrated fashion which is designed to be inherently stable against probing and environmental variations. By comparing our QCI to less complex interferometers, we also experimentally highlighted how randomness is a necessary but not sufficient criteria to achieve

unclonable device signatures. We further demonstrated feature extraction as a viable means for optical PUF identification. Since the main source of inter-chip variations are in waveguide width and surface roughness, by precisely analyzing each signal segment within a specific ‘frequency’ domain, and confined ‘time’ domain, it is ensured that these variations are captured during feature extraction and that the most unique features are chosen for the proposed PUFs. Unlike highly multi-mode devices based on chaos, which are extremely sensitive to all conditions, or single-mode optical backscatter which is environmentally stable but extremely weak, the signatures of our device are highly visible, random, and environmentally stable. As a result, our PUF architecture is fully compatible with automated wafer-scale measurement techniques and fosters scalable implementation within silicon photonic transceivers or photonic systems on a chip as an optical hardware security layer.

We first introduced the proof-of-concept architecture<sup>65</sup> in Conference on Lasers and Electro-Optics (CLEO) and later published an article<sup>66</sup> in “Nanophotonics” journal in the year 2020. This work also unveils a new means for amplifying and harnessing the effects of ‘weak’ disorder in photonics – while simultaneously harnessing or constraining specific degrees of freedom – and highlights a viable technological application of quasicrystals and Anderson localized and extended states. Applying the principles of degree of freedom constraints, modal selectivity, and confinement factor control principles, could support the realization of a new generation of disordered photonic systems. In the future, we envision opportunities to further enhance and utilize the functionality of integrated photonic PUFs by leveraging active devices, reconfigurability, multiplexing, far-field signaling, or quantum optics to realize entirely new levels of hardware and information security.

## References

1. Pappu, R., Recht, B., Taylor, J. & Gershenfeld, N. Physical One-Way Functions. *Science* **297**, 2026–2030 (2002).
2. Gassend, B., Clarke, D., Van Dijk, M. & Devadas, S. Silicon physical random functions. *Proc. ACM Conf. Comput. Commun. Secur.* 148–160 (2002).
3. Buchanan, J. D. R. *et al.* ‘Fingerprinting’ documents and packaging. *Nature* **436**, 475 (2005).
4. Rührmair, U., Hilgers, C. & Urban, S. Optical PUFs Reloaded. *IACR Cryptol.* (2013).
5. Uchida, A. *et al.* Fast physical random bit generation with chaotic semiconductor lasers. *Nat. Photonics* **2**, 728 (2008).
6. Pétrie, C. S. & Alvin Connelly, J. A noise-based ic random number generator for applications in Cryptography. *IEEE Trans. Circuits Syst. I Fundam. Theory Appl.* (2000). doi:10.1109/81.847868
7. Indeck, R. S. & Glavinas, E. Fingerprinting Magnetic Media. *IEEE Trans. Magn.* **29**, 4095–4097 (1993).
8. Lao, Y., Yuan, B., Kim, C. H. & Parhi, K. K. Reliable PUF-Based Local Authentication With Self-Correction. *IEEE Trans. Comput. Des. Integr. Circuits Syst.* (2017). doi:10.1109/TCAD.2016.2569581
9. Prabhu, P. *et al.* Extracting device fingerprints from flash memory by exploiting physical variations. in *Lecture Notes in Computer Science (including subseries Lecture Notes in Artificial Intelligence and Lecture Notes in Bioinformatics)* (2011). doi:10.1007/978-3-642-21599-5\_14
10. Grubel, B. C. *et al.* Secure communications using nonlinear silicon photonic keys. *Opt.*

*Express* **26**, 4710 (2018).

11. Di Falco, A., Mazzone, V., Cruz, A. & Fratalocchi, A. Perfect secrecy cryptography via mixing of chaotic waves in irreversible time-varying silicon chips. *Nat. Commun.* **10**, 5827 (2019).

12. McGrath, T., Bagci, I. E., Wang, Z. M., Roedig, U. & Young, R. J. A PUF taxonomy. *Appl. Phys. Rev.* **6**, (2019).

13. Chang, C., Zheng, Y. & Zhang, L. A Retrospective and a Look Forward: Fifteen Years of Physical Unclonable Function Advancement. *IEEE Circuits Syst. Mag.* **17**, 32–62 (2017).

14. Lao, Y. & Parhi, K. K. Statistical analysis of MUX-based physical unclonable functions. *IEEE Trans. Comput. Des. Integr. Circuits Syst.* (2014). doi:10.1109/TCAD.2013.2296525

15. Bhargava, M., Cakir, C. & Mai, K. Reliability enhancement of bi-stable PUFs in 65nm bulk CMOS. in *Proceedings of the 2012 IEEE International Symposium on Hardware-Oriented Security and Trust, HOST 2012* (2012). doi:10.1109/HST.2012.6224314

16. Cao, Y., Zhang, L., Zalivaka, S. S., Chang, C. H. & Chen, S. CMOS image sensor based physical unclonable function for coherent sensor-level authentication. *IEEE Trans. Circuits Syst. I Regul. Pap.* (2015). doi:10.1109/TCSI.2015.2476318

17. Arppe, R. & Sørensen, T. J. Physical unclonable functions generated through chemical methods for anti-counterfeiting. *Nat. Rev. Chem.* **1**, 31 (2017).

18. Roberts, J. *et al.* Using Quantum Confinement to Uniquely Identify Devices. *Sci. Rep.* **5**, 1–8 (2015).

19. Hu, Z. *et al.* Physically unclonable cryptographic primitives using self-Assembled carbon nanotubes. *Nat. Nanotechnol.* **11**, 559–565 (2016).



20. Alharbi, A., Armstrong, D., Alharbi, S. & Shahrjerdi, D. Physically Unclonable Cryptographic Primitives by Chemical Vapor Deposition of Layered MoS<sub>2</sub>. *ACS Nano* **11**, 12772–12779 (2017).
21. Smith, A. F., Patton, P. & Skrabalak, S. E. Plasmonic Nanoparticles as a Physically Unclonable Function for Responsive Anti-Counterfeit Nanofingerprints. *Adv. Funct. Mater.* **26**, 1315–1321 (2016).
22. Chen, H. *et al.* Highly Secure Physically Unclonable Cryptographic Primitives Based on Interfacial Magnetic Anisotropy. *Nano Lett.* **18**, 7211–7216 (2018).
23. Dodda, A. *et al.* Biological One-Way Functions for Secure Key Generation. *Adv. Theory Simulations* **2**, 1800154 (2019).
24. Wiersma, D. The smallest random laser. *Nature* **406**, 133–135 (2000).
25. Goorden, S. A., Horstmann, M., Mosk, A. P., Škorić, B. & Pinkse, P. W. H. Quantum-secure authentication of a physical unclonable key. *Optica* **1**, 421–424 (2014).
26. Bosworth, B. T. *et al.* Unclonable photonic keys hardened against machine learning attacks. *APL Photonics* **5**, 10803 (2020).
27. Helfmeier, C., Boit, C., Nedospasov, D. & Seifert, J.-P. Cloning physically unclonable functions. in *2013 IEEE International Symposium on Hardware-Oriented Security and Trust (HOST)* 1–6 (IEEE, 2013).
28. Rührmair, U. *et al.* PUF Modeling Attacks on Simulated and Silicon Data. *IEEE Trans. Inf. Forensics Secur.* **8**, 1876–1891 (2013).
29. Xu, Y. *et al.* Mathematical Modeling Analysis of Strong Physical Unclonable Functions. *IEEE Trans. Comput. Des. Integr. Circuits Syst.* 1 (2020). doi:10.1109/TCAD.2020.2969645

30. Mesaritakis, C. *et al.* Physical Unclonable Function based on a Multi-Mode Optical Waveguide. *Sci. Rep.* **8**, 1–12 (2018).
31. Grubel, B. C. *et al.* Silicon photonic physical unclonable function. *Opt. Express* **25**, 12710 (2017).
32. Grubel, B. C. *et al.* Light transport through ultrafast chaotic micro-cavities for photonic physical unclonable functions. *2017 51st Annu. Conf. Inf. Sci. Syst. CISS 2017* 1–6 (2017). doi:10.1109/CISS.2017.7926067
33. Wiersma, D. S. The physics and applications of random lasers. *Nat. Phys.* **4**, 359 (2008).
34. Kreger, S. T., Gifford, D. K., Froggatt, M. E., Soller, B. J. & Wolfe, M. S. High Resolution Distributed Strain or Temperature Measurements in Single-and Multi-mode Fiber Using Swept-Wavelength Interferometry. in *Optical Fiber Sensors ThE42* (Optical Society of America, 2006). doi:10.1364/OFS.2006.ThE42
35. Froggatt, M. E. & Gifford, D. K. Rayleigh backscattering signatures of optical fibers—Their properties and applications. in *2013 Optical Fiber Communication Conference and Exposition and the National Fiber Optic Engineers Conference (OFC/NFOEC)* 1–3 (2013).
36. Atabaki, A. H. *et al.* Integrating photonics with silicon nanoelectronics for the next generation of systems on a chip. *Nature* **556**, 349–354 (2018).
37. Jones, R. *et al.* Heterogeneously Integrated InP/Silicon Photonics: Fabricating Fully Functional Transceivers. *IEEE Nanotechnol. Mag.* **13**, 17–26 (2019).
38. Torrence, C. & Compo, G. P. A Practical Guide to Wavelet Analysis. *Bull. Am. Meteorol. Soc.* (1998). doi:10.1175/1520-0477(1998)079<0061:APGTWA>2.0.CO;2
39. Phinyomark, A., Limsakul, C. & Phukpattaranont, P. Application of wavelet analysis in

EMG feature extraction for pattern classification. *Meas. Sci. Rev.* (2011). doi:10.2478/v10048-011-0009-y

40. Wang, Y. *et al.* Focusing sub-wavelength grating couplers with low back reflections for rapid prototyping of silicon photonic circuits. *Opt. Express* **22**, 20652–20662 (2014).

41. Dulkeith, E., Xia, F. N., Schares, L., Green, W. M. J. & Vlasov, Y. A. Group index and group velocity dispersion in silicon-on-insulator photonic wires. *Opt. Express* **14**, 3853 (2006).

42. Davy, M. & Genack, A. Z. Selectively exciting quasi-normal modes in open disordered systems. *Nat. Commun.* **9**, 4714 (2018).

43. Segev, M., Silberberg, Y. & Christodoulides, D. N. Anderson localization of light. *Nat. Photonics* **7**, 197–204 (2013).

44. Roati, G. *et al.* Anderson localization of a non-interacting Bose–Einstein condensate. *Nature* **453**, 895–898 (2008).

45. Ghulinyan, M. *et al.* Light-pulse propagation in Fibonacci quasicrystals. *Phys. Rev. B - Condens. Matter Mater. Phys.* **71**, (2005).

46. Levi, L. *et al.* Disorder-Enhanced Transport in Photonic Quasicrystals. *Science* **332**, 1541 LP – 1544 (2011).

47. Dingel, B. B. & Izutsu, M. Multifunction optical filter with a Michelson–Gires–Tournois interferometer for wavelength-division-multiplexed network system applications. *Opt. Lett.* **23**, 1099–1101 (1998).

48. Simard, A. D., Painchaud, Y. & LaRochelle, S. Integrated Bragg gratings in spiral waveguides. *Opt. Express* **21**, 8953–8963 (2013).

49. Wang, B., Mazoyer, S., Hugonin, J. P. & Lalanne, P. Backscattering in monomode

periodic waveguides. *Phys. Rev. B* **78**, 245108 (2008).

50. Grote, R. R., Driscoll, J. B. & Osgood, R. M. Integrated optical modulators and switches using coherent perfect loss. **38**, 3001–3004 (2013).

51. Ryckman, J. D. Random Coherent Perfect Absorption with 2D Atomic Materials Mediated by Anderson Localization. *ACS Photonics* **5**, (2018).

52. Redding, B., Fatt Liew, S., Bromberg, Y., Sarma, R. & Cao, H. Evanescently coupled multimode spiral spectrometer. *Optica* **3**, 956 (2016).

53. Redding, B., Liew, S. F., Sarma, R. & Cao, H. Compact spectrometer based on a disordered photonic chip. *Nat. Photonics* **7**, 746 (2013).

54. Cao, H. Lasing in random media. *Waves in Random Media* **13**, R1–R39 (2003).

55. Suh, G. E. & Devadas, S. Physical unclonable functions for device authentication and secret key generation. in *Proceedings - Design Automation Conference* (2007). doi:10.1109/DAC.2007.375043

56. Herder, C., Yu, M. D., Koushanfar, F. & Devadas, S. Physical unclonable functions and applications: A tutorial. *Proceedings of the IEEE* (2014). doi:10.1109/JPROC.2014.2320516

57. Yin, C. E. & Qu, G. Temperature-aware cooperative ring oscillator puf. in *2009 IEEE International Workshop on Hardware-Oriented Security and Trust, HOST 2009* (2009). doi:10.1109/HST.2009.5225055

58. Yang, K., Dong, Q., Blaauw, D. & Sylvester, D. A physically unclonable function with BER  $<10^{-8}$  for robust chip authentication using oscillator collapse in 40nm CMOS. in *Digest of Technical Papers - IEEE International Solid-State Circuits Conference* (2015). doi:10.1109/ISSCC.2015.7063022

59. Graps, A. An Introduction to Wavelets. *IEEE Comput. Sci. Eng.* (1995).  
doi:10.1109/99.388960
60. Chrostowski, L. *et al.* Silicon Photonic Circuit Design Using Rapid Prototyping Foundry Process Design Kits. *IEEE J. Sel. Top. Quantum Electron.* **25**, 1–26 (2019).
61. M. C. Tropicovsky, A. S. Sabau, A. R. Lupini, and Z. Zhang. "Transfer-matrix formalism for the calculation of optical response in multilayer systems: from coherent to incoherent interference," *Opt. Express* 18, 24715-24721 (2010).
62. A. Berk. "Variational principles for electromagnetic resonators and waveguides," *IRE Transactions on Antennas and Propagation* 4(2), 104-111 (1956).
63. Charles K. Chui. *An introduction to wavelets*, Elsevier, (2016).
64. M. Nielsen. "On the construction and frequency localization of finite orthogonal quadrature filters," *Journal of Approximation Theory*, 108(1), 36–52 (2001).
65. Farhan Bin Tarik, Azadeh Famili, Yingjie Lao and Judson D. Ryckman, "Realization of robust optical physical unclonable function in a quasicrystal silicon photonic interferometer," Conference on Laser and Electro-Optics (2020).
66. Farhan Bin Tarik, Azadeh Famili, Yingjie Lao and Judson D. Ryckman, "Robust optical physical unclonable function using disordered photonic integrated circuits," *Nanophotonics* 9, 2817–2828 (2020).

# SCALABLE AND CMOS COMPATIBLE HARDWARE AUTHENTICATION OF 56 QCI PUFs

### 4.1 Introduction

As discussed in chapter 3, physical unclonable functions (PUFs) have garnered significant attention within the micro-electronics and hardware security communities due to their ability to provide chip-unique signatures which provide a foundation for performing many cryptographic applications<sup>1-3</sup>. As electronic-PUFs have continued to mature<sup>4</sup>, their prospective limitations and vulnerabilities have become increasingly important factors to address and/or circumnavigate. Along this vein, photonic-PUFs have witnessed renewed and increasing interests in recent years as they attractively offer an inherently non-electronic platform with rich underlying physics and large information capacity.

A variety of photonic-PUFs have now been demonstrated across both classical<sup>5-8</sup> and quantum regimes<sup>9,10</sup>, ranging from purely passive devices<sup>6-8</sup> to active non-linear devices<sup>11,12</sup>. Photonic-PUFs are also uniquely compatible with non-contact optical probing as well as optical communication links<sup>11,13</sup>, allowing them to provide increasingly distinct functionalities. These and future iterations of photonic-PUFs are expected to facilitate cryptographic applications such as secure authentication, identification, and communication through a variety of device formats, i.e., passive/active, all-optical, electronic-photonic, and quantum-optical. Moreover, with the recent maturation and successful commercialization of integrated silicon photonics, a variety of photonic-

PUFs can now be scalably realized in modern complementary metal–oxide–semiconductor (CMOS) fabrication processes. However, most photonic-PUFs reported to date have been realized and studied in very limited quantities, i.e., ranging from only a few devices<sup>5,8</sup> up to roughly one dozen<sup>12</sup>. As photonic-PUFs push from proof-of-concept devices toward practical and scalable security solutions, it is increasingly important to examine and validate their characteristics on larger scales.

## 4.2 Foreground

In the previous chapter, we have demonstrated a proof-of-concept photonic-PUF based on a silicon photonic moiré quasicrystal interferometer (QCI) which was instantiated  $N = 3$  times<sup>8</sup>. This replication allowed for  $N = 3$  unique device authentications and  $M = N(N - 1) = 6$  inter-device comparisons or false authentication attempts. In this report, we further extend our research to a substantial  $N = 56$  device instantiations realized in batches of 28 devices across two different fabrication facilities, with each instantiation and fab utilizing an exact copy of the same underlying QCI design. Semi-automated PUF measurements followed by digital key extraction enable  $N = 56$  unique authentications and  $M = N(N-1) = 3,080$  inter-device comparisons or false authentication attempts to be performed. These photonic-PUF characterizations enable estimation of the authentication error rate (AER), false authentication rate (FAR), and probability of cloning (POC) as a function of the analysis parameters and/or authentication technique (e.g. Hamming vs. correlation based). Our results provide strong evidence of device uniqueness and unclonability and highlight disordered integrated photonics as a promising and scalable paradigm for realizing hardware security solutions.

### 4.3 Approach

Fig. 4.1 illustrates our QCI based PUF and secure authentication framework. The QCI design is described in detail in Ref. <sup>8</sup>. Briefly, within each arm of the interferometer are waveguide spirals that contain identically designed silicon photonic quasicrystals which lack translational symmetry and support Aubry-André analyticity breaking<sup>14</sup> and a 1D localization/delocalization transition<sup>15</sup>. The randomized nature of each photonic-PUF's transmission spectrum is derived the QCI design being highly sensitized to distributed fabrication induced imperfections, such as nanoscale errors in waveguide width, which modulate the effective index profile of each quasicrystal and can induce transitions from delocalized waveguiding to localized resonant behavior. By designing our structures to include regions with narrow grating teeth and a small sidewall modulation depth of  $\pm 20\text{nm}$ , we intentionally maximize the relative impact that nanoscale imperfections and natural spatially distributed fabrication disorder impart onto the realized devices<sup>16</sup>. Meanwhile, the grating couplers and single-mode waveguides act as polarization and mode filters which ensure the PUF response is insensitive to drifts or variations in probing conditions (e.g. polarization, angular or spatial alignment). In addition to enabling compact footprint and CMOS compatibility, the integrated nature of the device provides inherent robustness or reliability advantages over free-space or fiber based optical PUFs which may be highly sensitized to probing or environmental conditions<sup>8</sup>.



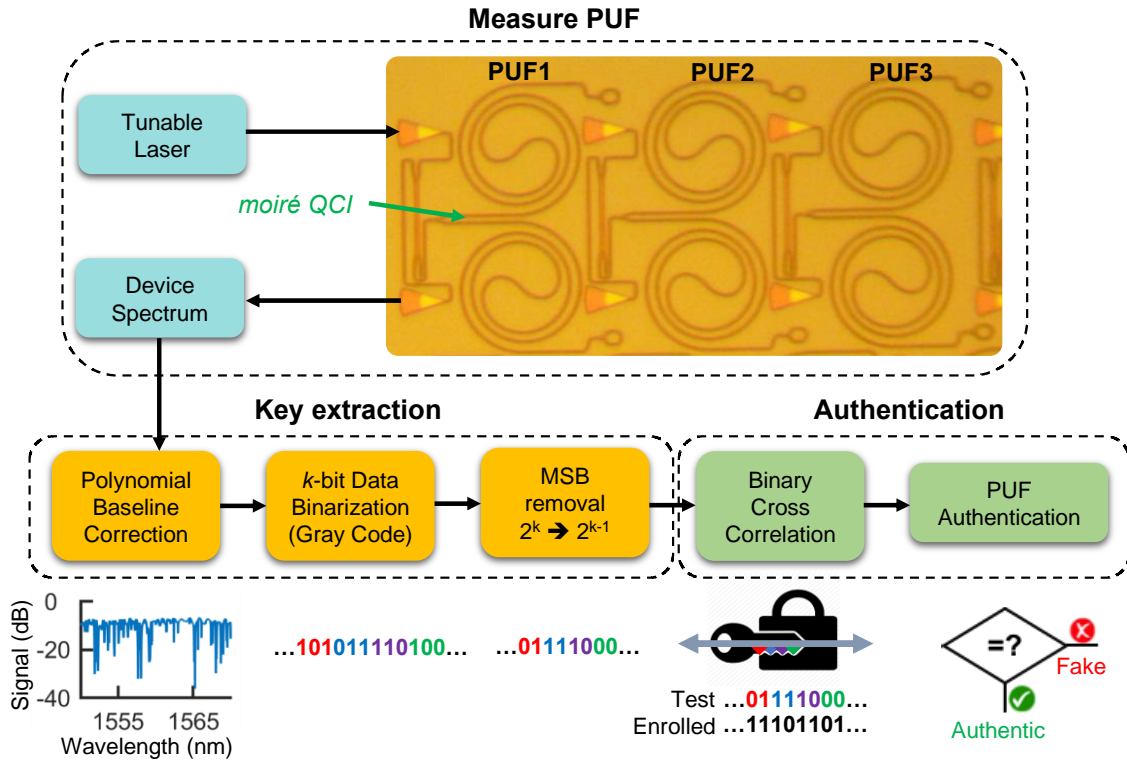


Fig. 4.1. QCI PUF architecture and authentication framework: post-processing technique is shown involving conversion of spectral response to binary sequence, followed by binary cross correlation analysis to achieve proper authentication

In this work, half, or  $N/2 = 28$ , of the identically designed PUF devices, were co-fabricated in two separate fabrication runs at (1) University of Washington Nanofabrication Facility and (2) Applied Nanotools fabrication facility, referred to here as “Fab 1” and “Fab 2” respectively (see Methods). As illustrated in Fig. 4.1, a digital key is extracted from each photonic-PUF through a series of steps. First, the device transmission spectra are collected with a tunable laser (Agilent 81600B) with a 10 pm resolution. The slowly varying spectral envelope associated with the grating couplers is then removed using a polynomial baseline correction. Note: spectra for all 56 devices are available in Fig 4.3. The spectral features remaining after baseline correction are then purely associated with the photonic-PUF under test. The spectra are then binarized in gray code by rescaling the log scale transmission loss into a range between 0 and  $2^k-1$ , where  $k$  is the number of bits for binarization. We then remove the most significant bit (MSB) so that the bit length per

sample is  $k - 1$ . The total bit length  $L$  of each photonic-PUF derived key is then  $L = K(k - 1)$  where  $K$  is the number of wavelength samples. In our case, a 35 nm spectral wavelength window (1540 nm – 1575 nm) with a resolution of 10 pm results in  $K = 3500$  and choosing  $k = 3$  produces a key length of  $L = 7000$  bits for each PUF.

## 4.4 Methods

### 4.4.1 Device fabrication and testing

For this work, device fabrication and measurement was performed through the edX UBCx Phot1x Silicon Photonics Design, Fabrication and Data Analysis course (organized by L. Chrostowski)<sup>19</sup>. Half, or  $N/2 = 28$ , of the identically designed PUF devices were co-fabricated in two separate fabrication runs at the University of Washington nanofabrication facility (WNF or ‘Fab 1’) and Applied Nanotools (ANT or ‘Fab 2’) fabrication facility.

#### *A. Applied Nanotools, Inc. NanoSOI process*

The NanoSOI MPW fabrication process by Applied Nanotools Inc. (<http://www.appliednt.com/nanosoi>; Edmonton, Canada) is based on direct-write 100 keV electron beam lithography technology. Silicon-on-insulator wafers of 200 mm diameter, 220 nm device thickness and 2  $\mu$ m buffer oxide thickness are used as the base material for the fabrication. After an initial wafer clean using piranha solution (3:1 H<sub>2</sub>SO<sub>4</sub>:H<sub>2</sub>O<sub>2</sub>) for 15 minutes and water/IPA rinse, hydrogen silsesquioxane (HSQ) resist was spin-coated onto the substrate and heated to evaporate the solvent. The photonic devices were patterned using a Raith EBPG 5000+ electron beam instrument using a raster step size of 5 nm. The exposure dosage of the design was corrected for proximity effects that result from the backscatter of electrons from exposure of nearby features. Shape writing order was optimized for efficient patterning and minimal beam drift. After the e-beam exposure and subsequent development with a tetramethylammonium sulfate (TMAH)

solution, the devices were inspected optically for residues and/or defects. The chips were then mounted on a 4" handle wafer and underwent an anisotropic ICP-RIE etch process using chlorine after qualification of the etch rate. The resist was removed from the surface of the devices using a 10:1 buffer oxide wet etch, and the devices were inspected using a scanning electron microscope (SEM) to verify patterning and etch quality. A 2.2  $\mu\text{m}$  oxide cladding was deposited using a plasma-enhanced chemical vapour deposition (PECVD) process based on tetraethyl orthosilicate (TEOS) at 300°C. Reflectometry measurements were performed throughout the process to verify the device layer, buffer oxide and cladding thicknesses before delivery.

#### *B. Washington Nanofabrication Facility (WNF) silicon photonics process*

The devices were fabricated using 100 keV Electron Beam Lithography<sup>20</sup>. The fabrication used silicon-on-insulator wafer with 220 nm thick silicon on 3  $\mu\text{m}$  thick silicon dioxide. After a solvent rinse and hot-plate dehydration bake, hydrogen silsesquioxane resist (HSQ, Dow-Corning XP-1541-006) was spin-coated at 4000 rpm, then hotplate baked at 80 °C for 4 minutes. Electron beam lithography was performed using a JEOL JBX-6300FS system operated at 100 keV energy, 8 nA beam current, and 500  $\mu\text{m}$  exposure field size. The machine grid used for shape placement was 1 nm, while the beam stepping grid, the spacing between dwell points during the shape writing, was 6 nm. An exposure dose of 2800  $\mu\text{C}/\text{cm}^2$  was used. The resist was developed by immersion in 25% tetramethylammonium hydroxide for 4 minutes, followed by a flowing deionized water rinse for 60 s, an isopropanol rinse for 10 s, and then blown dry with nitrogen. The silicon was removed from unexposed areas using inductively coupled plasma etching in an Oxford Plasmalab System 100, with a chlorine gas flow of 20 sccm, pressure of 12 mT, ICP power of 800 W, bias power of 40 W, and a platen temperature of 20 °C, resulting in a bias voltage of 185 V. During etching, chips were mounted on a 100 mm silicon carrier wafer using perfluoropolyether vacuum oil. Cladding oxide was deposited using plasma enhanced chemical vapor deposition (PECVD) in an Oxford

Plasmalab System 100 with a silane ( $\text{SiH}_4$ ) flow of 13.0 sccm, nitrous oxide ( $\text{N}_2\text{O}$ ) flow of 1000.0 sccm, high-purity nitrogen ( $\text{N}_2$ ) flow of 500.0 sccm, pressure at 1400mT, high-frequency RF power of 120W, and a platen temperature of 350C. During deposition, chips rest directly on a silicon carrier wafer and are buffered by silicon pieces on all sides to aid uniformity.

#### 4.4.2 Device measurement

Semi-automated grating coupled device measurements were performed at The University of British Columbia. A tunable laser (Agilent 81600B) and optical power meter (Agilent 81635A) were used to capture device spectra over the range 1500–1600 nm in 10 pm steps.

### 4.5 Results and Analysis

To investigate device authentication all devices were remeasured approximately two days after their initial room temperature measurement at a secondary temperature (30°C). A subset of the binary keys extracted for all 56 PUFs for  $k = 3$  at 25°C and 30°C are visualized in Fig. 4.2a & 4.2b respectively. It is imperative to mention that extensive analysis have been performed to realize the best ' $k$ ' value. The results of these analysis are discussed in the following portions of the chapter. Due to silicon's thermo-optic effect shifting the spectral response of each device in the wavelength domain over temperature, a corresponding shift in the bit sequence of each key is also observed. Experimentally we observe a shift of 70 bits (Fig. 4.2) indicating a thermo-optic wavelength shift of ~35 pm, which is in close agreement with prediction based on silicon's thermo-optic coefficient of  $1.86 \times 10^{-4}$  RIU/K<sup>17</sup> and a waveguide transverse confinement factor in silicon near ~0.88.

#### 4.5.1 Correlation Analysis

To evaluate authenticity or uniqueness between an enrolled key  $x(n)$  from the database and a new test key  $y(n)$ , we measure the similarity between the two keys while simultaneously mitigating the influence of thermo-optic effects. Previously we have reported one analysis approach based on

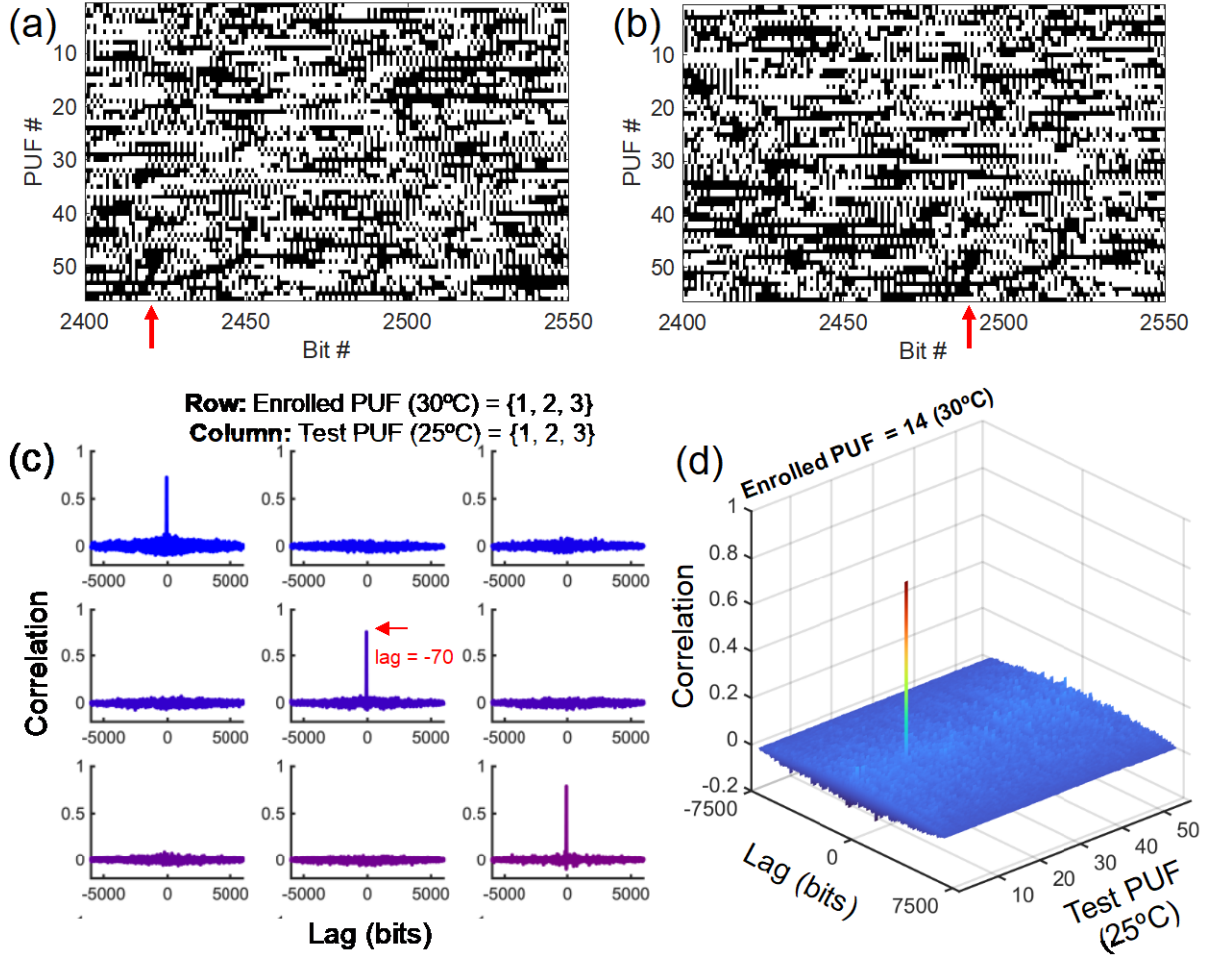


Fig. 4.2. Digital keys and cross-correlation analysis. Visualization of a 150 bit subset of the binary keys generated from all 56 PUFs extracted from measurements at (a) 25°C and (b) 30°C; the red arrow indicates the 70 bit lag observed due to the spectral shift over temperature. (c) Cross-correlation analysis depicting the normalized correlation coefficient between the enrolled PUF at 30°C and test PUF at 25°C vs. lag for selected PUFs 1-3. (d) Example cross-correlation analysis of enrolled PUF 14 vs. all 56 test PUFs verifying the uniqueness and authenticity of the enrolled device

a “sliding key” Hamming distance (HD) computation, wherein the fractional HD is computed while shifting the test key relative to the enrolled key, with the output HD reported as the minimum fractional HD value obtained across all key lags<sup>8</sup>. A second and more standardized approach, evaluated here, would be to simply compute the normalized cross-correlation between the enrolled key,  $x(n)$ , and the test key,  $y(n)$ , and to record the maximum normalized cross-correlation value  $C_{xy}$  according to<sup>18</sup>:

$$C_{xy} = \max \left\{ \frac{R_{xy}(m)}{\sqrt{R_{xx}(0)R_{yy}(0)}} \right\}$$

where the unnormalized cross-correlation  $R_{xy}(m)$  as a function of lag  $m$  is defined according to:

$$R_{xy}(m) = \begin{cases} \sum_{n=1}^{L-m} x(n+m)y(n), & m \geq 0 \\ \sum_{n=1}^{L+m} y(n-m)x(n), & m < 0 \end{cases}$$

Unlike a single HD or correlation computation, this cross-correlation based analysis naturally mitigates for any bit shifts that arise from the thermo-optic drift of the PUF's spectral signature.

Fig. 4.2c & 4.2d illustrate the cross-correlation results for selected PUFs and confirm that distinct PUF keys are both uncorrelated and aperiodic. To facilitate arithmetic computation of the cross-correlation from a logical bit sequence, we assign logical '1' to a positive variable  $a$  and logical '0' to its negative,  $-a$ . For an ideally unbiased sequence with equiprobability of '0' or '1', this approach naturally removes the DC component of the signals. Note: a resulting correlation value  $C_{xy}$  near 1 or -1 indicates strong correlation or anti-correlation respectively, while  $C_{xy}$  near 0 indicates signals that are uncorrelated. The aperiodic vs. periodic nature of a given key is evaluated by identifying either only one spike or multiple spikes respectively from the cross-correlation or cross-autocorrelation.

#### 4.5.2 Hamming Distance Authentication Method

Next, we expand our analysis to all 56 PUFs and test for device authenticity by enrolling each key measured at 25°C and comparing against all 56 test keys measured at 30°C, allowing us to examine  $N = 56$  'intra-chip' authentication attempts and  $N(N-1) = 3080$  'inter-chip' false

authentication attempts. The measured spectra for all 56 PUFs at two temperatures are shown in Fig. 4.3. To explore potential trade-offs between PUF key size and the reliability of each analysis technique (e.g. HD or correlation), we examined results for  $k$  values from 2 to 5 resulting in key sizes ranging from  $L = 1750$  to 14,000 (Fig. 4.6). A summary of the correlation and HD based authentication results for  $k = 3$  and 5 are reported in Fig. 4.4. As shown in Fig. 4.4a & 4.4b, the cross-correlation technique effectively distinguishes between fake and authentic devices for both key lengths as the inter-chip and intra-chip distributions are well isolated. For example, a correlation decision threshold near  $\sim 0.25$  could be used to confidently distinguish between authentic vs. fake devices with an experimentally observed false authentication rate (FAR) of 0% and authentication error rate (AER) of 0%. The HD technique also works effectively for  $k = 3$ , but exhibits a degradation in AER performance for  $k = 5$  as indicated in Fig. 4.4c & 4.4d. These results suggest the HD method is more sensitive than the cross-correlation to bit errors which increase as the PUF spectra are digitized with higher resolution.

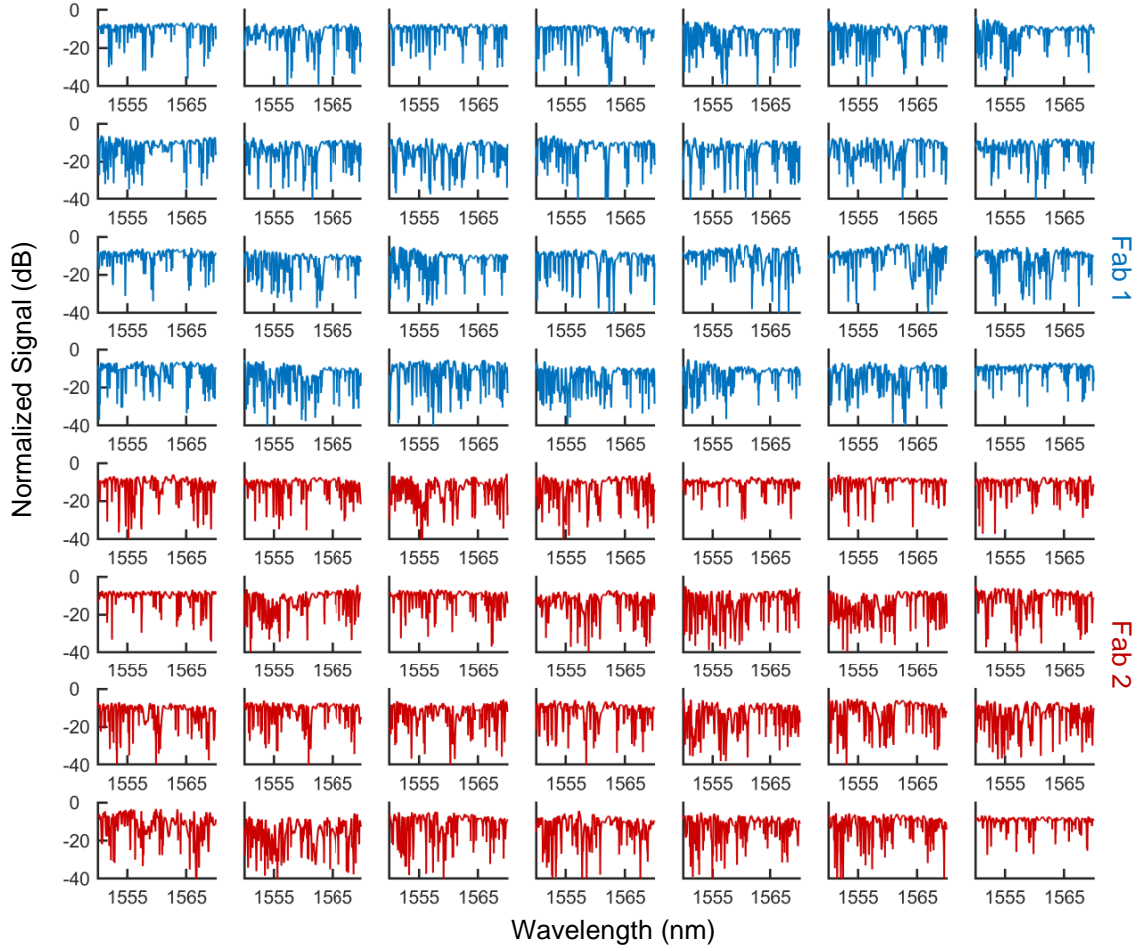


Fig. 4.3. Measured spectra shown after baseline correction for all 56 PUFs. (PUF1 in top left corner and PUF 56 in bottom right corner)

From the measured inter-chip and intra-chip probability density functions (pdfs), we then estimate the probabilities of false authentication (FA) and authentication error (AE) as a function of the decision threshold by computing the corresponding cumulative distribution functions (cdf) as reported in Fig. 4.4e & 4.4f. The probability of false authentication effectively provides an estimate of the PUF cloning probability. In the case where our PUF keys are authenticated using cross-correlation with  $k = 3$  and 5, a decision threshold of 0.25 corresponds to estimated POC values below  $10^{-30}$  and  $10^{-40}$  respectively. The HD based analysis indicates a similar degree of unclonability, which suggests the primary benefits of the cross-correlation technique are its



straightforward implementation, computational efficiency<sup>18</sup>, and improved intra-chip reliability, particularly for larger  $k$ .

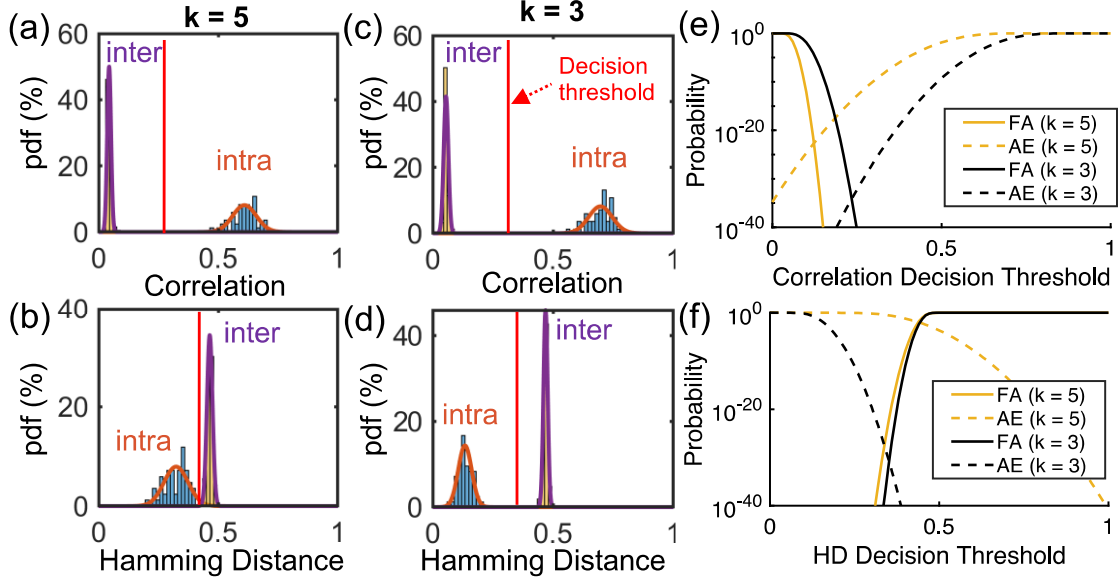


Fig. 4.4. (a) Correlation-based authentication with  $k = 5$ , (b) HD based authentication with  $k = 5$ , (c) correlation-based authentication with  $k = 3$ , (d) HD based authentication with  $k = 3$ . Cumulative distribution functions indicating the probabilities of false authentication (FA) or authentication error (AE) as a function of decision threshold for (e) correlation based and (f) HD based authentication

#### 4.5.3 Cross-fab Analysis and Comprehension on Correlation and HD Methods

Lastly, we summarize and breakdown our results according to the originating fabrication facility, with PUFs 1-28 corresponding to ‘Fab 1’ and PUFs 29-56 corresponding to ‘Fab 2’. As indicated by inspecting QCI PUF spectra from each fab (Fig. 4.5a & 4.5b and Fig. 4.3), all QCIs provide randomized spectral features in the same working spectral window with similar extinction ratios. This indicates the processes are approximately matched in terms of propagation loss and the nominal waveguide dimensions which affect the nominal effective index and Bragg wavelengths of the constituent moiré sub-lattices used to construct the QCI. The results also qualitatively suggest a similar degree of nanoscale fabrication induced disorder is naturally present in each process. Despite these similarities, we found all 56 PUFs to be unique and uncorrelated to one-another as noted in results from Fig. 4.4 and summarized in Fig. 4.5c. Moreover, the uncorrelated

nature of each distinct PUF is not found to exhibit any dependence on the fabrication facility, as the mean inter-chip correlation coefficient (maximum cross-correlation) is unchanged when comparing devices from the same fab ( $\mu = 0.07$ ) vs. comparing devices across fabs ( $\mu = 0.07$ ) as shown in Fig. 4.5c. In other words, devices from both fabs were measured to be equally unclonable. The mean intra-chip correlation coefficient, however, does exhibit a small dependence on the fabrication facility, with devices originating from Fab 1 being authenticated with a higher mean correlation coefficient ( $\mu = 0.78$ ) than devices originating from Fab 2 ( $\mu = 0.74$ ). This however does not impact the empirically measured AER, which is observed to be 0% for devices from each fabrication facility.

The comprehensive analysis of correlation and HD approaches have been reported in Fig. 4.6 with varying ' $k$ ' values. The figure also contains a summary table of measured mean and standard deviations from the methods.

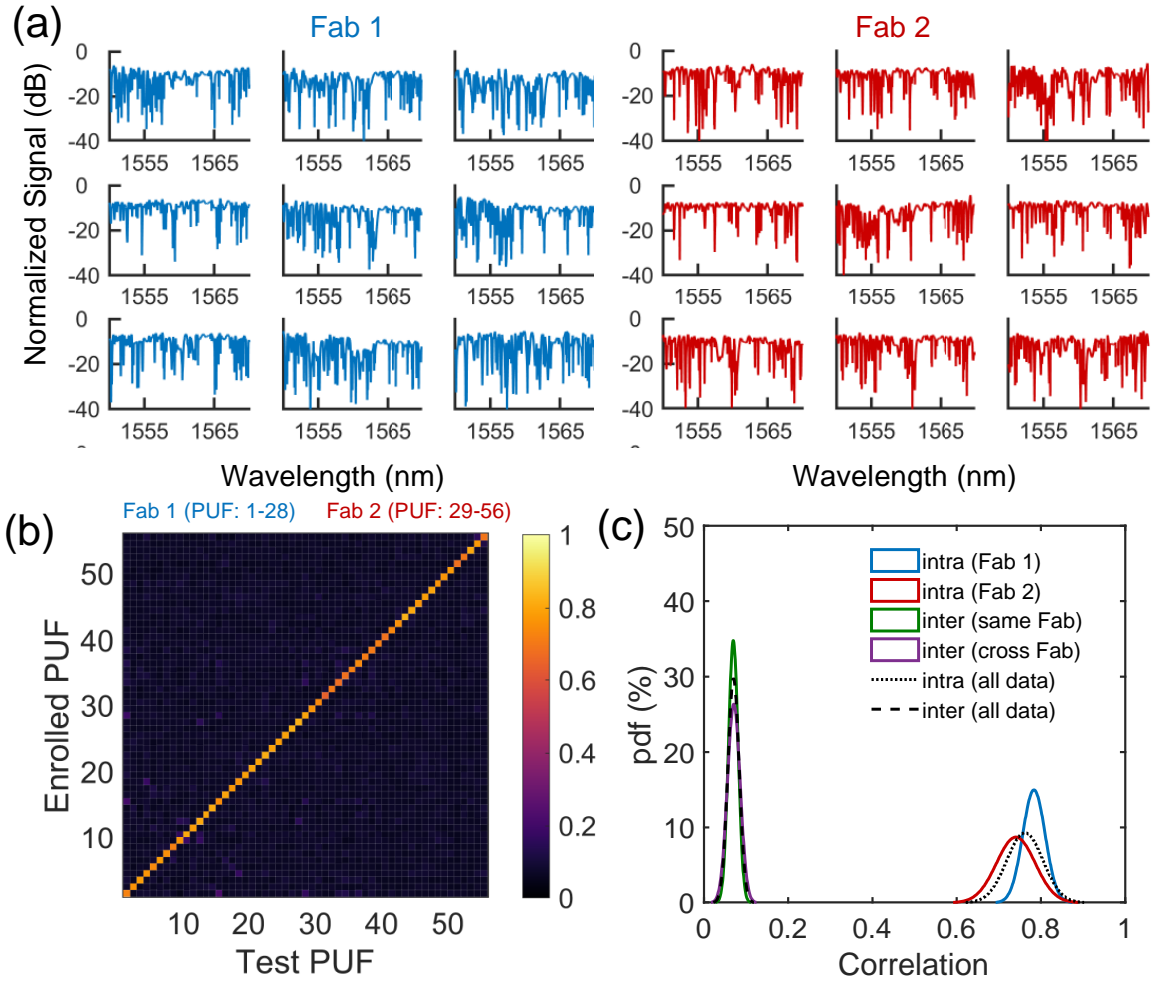
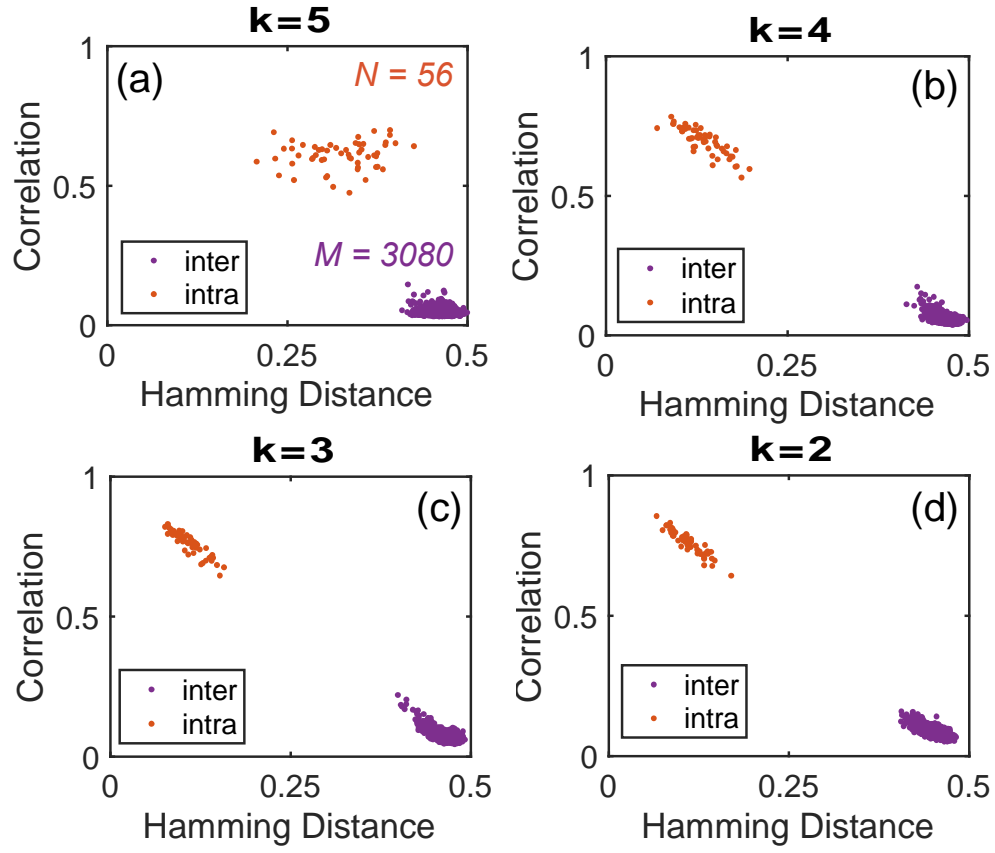


Fig. 4.5. Cross-fab analysis: (a) QCI PUF spectra for a selected subset of 9 out of 28 PUFs from each Fab; (b) summary of cross-correlation based authentication results ( $k = 3$ ) for all 56 PUFs; and (c) intra-chip and inter-chip distributions obtained when comparing PUF keys across or within each Fab



	Intra (Correlation)		Inter (Correlation)		Intra (Hamming)		Inter (Hamming)	
	$\mu$	$\sigma$	$\mu$	$\sigma$	$\mu$	$\sigma$	$\mu$	$\sigma$
<b>k = 5</b>	0.60968	0.049232	0.04372	0.00797	0.32364	0.05024	0.46438	0.0115
<b>k = 4</b>	0.69678	0.048932	0.05521	0.00962	0.13392	0.02782	0.46888	0.0086
<b>k = 3</b>	0.762	0.043006	0.07008	0.01340	0.1093	0.02087	0.46543	0.00977
<b>k = 2</b>	0.76113	0.043201	0.08804	0.01362	0.11035	0.02196	0.44944	0.0104

Fig 4.6. (Top) Correlation vs. HD results for (a)  $k = 5$ , (b)  $k = 4$ , (c)  $k = 3$ , and (d)  $k = 2$ . The correlation coefficient approaches 1 (or 0) as HD approaches 0 (or 0.5). A clear decision threshold cannot be drawn for HD method with  $k = 5$ , whereas one can be drawn using the correlation method. (Bottom) summary table of measured means and standard deviations

## 4.6 Conclusion

We can conclude the chapter by stating that QCI based silicon photonic-PUFs are a scalable solution for secure authentication in the untrusted supply chain and our study supports the statement quite well. Compared to prior works typically comparing on the order of 10 inter-chip PUF signatures, this work compares  $>10^3$  inter-chip PUF signatures. We observe zero authentication errors (out of  $N = 56$  attempts) and zero false authentications (out of  $M = 3,088$  attempts). These results are achieved from devices replicated from the exact same PUF photonic circuit design across two different fabrication facilities. The size of this dataset allows us to empirically test the unclonability of our photonic-PUFs and to estimate the probability of cloning at less than  $10^{-30}$ . As such, this work provides an important step toward scalable implementation of photonic-PUFs in practical hardware authentication applications. These photonic-PUFs are also attractive for chip identification applications since they provide chip-unique signatures which could be used to identify and track parts from front-end wafer processing through to packaging and/or deployment within the untrusted supply chain, effectively serving as unforgeable and tamper-proof lot, wafer, and/or die identifiers. Furthermore, we anticipate related types of photonic-PUF structures, based on integrated photonics, can be scalably employed in active optoelectronic, all-optical, or quantum readout schemes to facilitate applications such as remote authentication and secure communication.

## References

- (1) Pappu, R.; Recht, B.; Taylor, J.; Gershenfeld, N. Physical One-Way Functions. *Science* **2002**, 297 (5589), 2026–2030. <https://doi.org/10.1126/science.1074376>.
- (2) Gao, Y.; Al-Sarawi, S. F.; Abbott, D. Physical Unclonable Functions. *Nat. Electron.* **2020**, 3 (2), 81–91. <https://doi.org/10.1038/s41928-020-0372-5>.

- (3) McGrath, T.; Bagci, I. E.; Wang, Z. M.; Roedig, U.; Young, R. J. A PUF Taxonomy. *Appl. Phys. Rev.* **2019**, *6* (1). <https://doi.org/10.1063/1.5079407>.
- (4) Chang, C.; Zheng, Y.; Zhang, L. A Retrospective and a Look Forward: Fifteen Years of Physical Unclonable Function Advancement. *IEEE Circuits Syst. Mag.* **2017**, *17* (3), 32–62.
- (5) Grubel, B. C.; Bosworth, B. T.; Kossey, M. R.; Sun, H.; Cooper, A. B.; Foster, M. A.; Foster, A. C. Silicon Photonic Physical Unclonable Function. *Opt. Express* **2017**, *25* (11), 12710. <https://doi.org/10.1364/oe.25.012710>.
- (6) Du, Y.; Jothibas, S.; Zhuang, Y.; Zhu, C.; Huang, J. Unclonable Optical Fiber Identification Based on Rayleigh Backscattering Signatures. *J. Light. Technol.* **2017**, *35* (21), 4634–4640.
- (7) Mesaritakis, C.; Akriotou, M.; Kapsalis, A.; Grivas, E.; Chaintoutis, C.; Nikas, T.; Syvridis, D. Physical Unclonable Function Based on a Multi-Mode Optical Waveguide. *Sci. Rep.* **2018**, *8* (1), 1–12. <https://doi.org/10.1038/s41598-018-28008-6>.
- (8) Bin Tarik, F.; Famili, A.; Lao, Y.; Ryckman, J. D. Robust Optical Physical Unclonable Function Using Disordered Photonic Integrated Circuits. *Nanophotonics* **2020**, *9* (9), 2817–2828. <https://doi.org/https://doi.org/10.1515/nanoph-2020-0049>.
- (9) Goorden, S. A.; Horstmann, M.; Mosk, A. P.; Škorić, B.; Pinkse, P. W. H. Quantum-Secure Authentication of a Physical Unclonable Key. *Optica* **2014**, *1* (6), 421–424. <https://doi.org/10.1364/OPTICA.1.000421>.
- (10) Jacinto, H. S.; Smith, A. M.; Rafla, N. I. Utilizing a Fully Optical and Reconfigurable PUF as a Quantum Authentication Mechanism. *OSA Contin.* **2021**, *4* (2), 739. <https://doi.org/10.1364/osac.399294>.

- (11) Grubel, B. C.; Bosworth, B. T.; Kossey, M. R.; Cooper, A. B.; Foster, M. A.; Foster, A. C. Secure Communications Using Nonlinear Silicon Photonic Keys. *Opt. Express* **2018**, *26* (4), 4710. <https://doi.org/10.1364/oe.26.004710>.
- (12) Bosworth, B. T.; Atakhodjaev, I. A.; Kossey, M. R.; Grubel, B. C.; Vresilovic, D. S.; Stroud, J. R.; Macfarlane, N.; Villalba, J.; Dehak, N.; Cooper, A. B.; Foster, M. A.; Foster, A. C. Unclonable Photonic Keys Hardened against Machine Learning Attacks. *APL Photonics* **2020**, *5* (1). <https://doi.org/10.1063/1.5100178>.
- (13) Di Falco, A.; Mazzone, V.; Cruz, A.; Fratalocchi, A. Perfect Secrecy Cryptography via Mixing of Chaotic Waves in Irreversible Time-Varying Silicon Chips. *Nat. Commun.* **2019**, *10* (1), 5827. <https://doi.org/10.1038/s41467-019-13740-y>.
- (14) Aubry, S.; Andre, G. Analyticity Breaking and Anderson Localization in Incommensurate Lattices. *Ann. Isr. Phys. Soc.* **1980**, *3*, 133–140.
- (15) Wang, P.; Zheng, Y.; Chen, X.; Huang, C.; Kartashov, Y. V.; Torner, L.; Konotop, V. V.; Ye, F. Localization and Delocalization of Light in Photonic Moiré Lattices. *Nature* **2020**, *577* (7788), 42–46. <https://doi.org/10.1038/s41586-019-1851-6>.
- (16) Talukdar, T. H.; Hardison, A. L.; Ryckman, J. D. Moiré Effects in Silicon Photonic Nanowires. *ACS Photonics* **2022**, *9* (4), 1286–1294. <https://doi.org/10.1021/acsp Photonics.1c01800>.
- (17) Komma, J.; Schwarz, C.; Hofmann, G.; Heinert, D.; Nawrodt, R. Thermo-Optic Coefficient of Silicon at 1550 Nm and Cryogenic Temperatures. *Appl. Phys. Lett.* **2012**, *101* (4), 41905. <https://doi.org/10.1063/1.4738989>.
- (18) Kaso, A. Computation of the Normalized Cross-Correlation by Fast Fourier Transform. *PLoS One* **2018**, *13* (9), e0203434.

- (19) Chrostowski, L.; Shoman, H.; Hammood, M.; Yun, H.; Jhoja, J.; Luan, E.; Lin, S.; Mistry, A.; Witt, D.; Jaeger, N. A. F.; Shekhar, S.; Jayatilleka, H.; Jean, P.; Villers, S. B.-.; Cauchon, J.; Shi, W.; Horvath, C.; Westwood-Bachman, J. N.; Setzer, K.; Aktary, M.; Patrick, N. S.; Bojko, R. J.; Khavasi, A.; Wang, X.; Lima, T. F. de; Tait, A. N.; Prucnal, P. R.; Hagan, D. E.; Stevanovic, D.; Knights, A. P. Silicon Photonic Circuit Design Using Rapid Prototyping Foundry Process Design Kits. *IEEE J. Sel. Top. Quantum Electron.* **2019**, 25 (5), 1–26. <https://doi.org/10.1109/JSTQE.2019.2917501>.
- (20) Bojko, R. J.; Li, J.; He, L.; Baehr-Jones, T.; Hochberg, M.; Aida, Y. Electron Beam Lithography Writing Strategies for Low Loss, High Confinement Silicon Optical Waveguides. *J. Vac. Sci. Technol. B, Nanotechnol. Microelectron. Mater. Process. Meas. Phenom.* **2011**, 29 (6), 06F309. <https://doi.org/10.1116/1.3653266>.



# ELECTRICALLY RECONFIGURABLE PUF BASED ON MOIRÉ QCI

### 5.1 Introduction

In the earlier chapters, we introduced a passive version of a silicon photonic PUF, realized through the development of a quasicrystal interferometer (QCI) [1]. This structure is motivated to simultaneously harvest entropy by enhancing sensitivity to nanoscale fabrication disorder and to suppress adverse environmental and/or probing effects which may impact robustness or reliability in confirming the cryptographic signature. We later reported the extension of this research in terms of secure authentication of 56 moiré QCI PUFs. In this report, we demonstrate an active version of the same type PUF by integrating micro-heaters above each arm of the QCI. The addition of the micro-heaters provides an electrical stimulus which can be used to reconfigure the device's unclonable optical response, thus fostering enhanced reliability or security to be derived from the same device footprint.

### 5.2 Approach

Enhancing complexity of both the device itself and/or its output response characteristics is crucial to assuring unclonability and security. In our QCIs, this is achieved by employing within each arm of the Michelson type interferometer identically designed moiré quasicrystals which superimpose two sub-lattices with periodicities of 324.5 nm and 325.5 nm, for a Bragg wavelength

near  $\sim 1610$  nm. Traditionally, such a moiré lattice would be considered super-periodic, however in our structures the periodic translational symmetry of the waveguide effective index is broken by the variable radius of curvature in each waveguide spiral. This yields a quasi-crystalline structure which exhibits Aubry-André analyticity breaking and supports a 1D localization-delocalization transition [2]. This aids the formation of localized states and resonant modes in response to weak nanoscaled fabrication disorder, whereas a conventional disordered system with finite length would require a longer device structure and/or a larger critical disorder strength to achieve Anderson localization<sup>[10]</sup>.

### 5.3 Device Fabrication

Our devices were fabricated in a multi-project wafer (MPW) 220 nm device layer silicon photonics process at Applied Nanotools Inc. Fig. 5.1(a) shows a microscope image of a QCI PUF with two integrated micro-heaters. The heaters are created via tri-layer metallization with titanium-

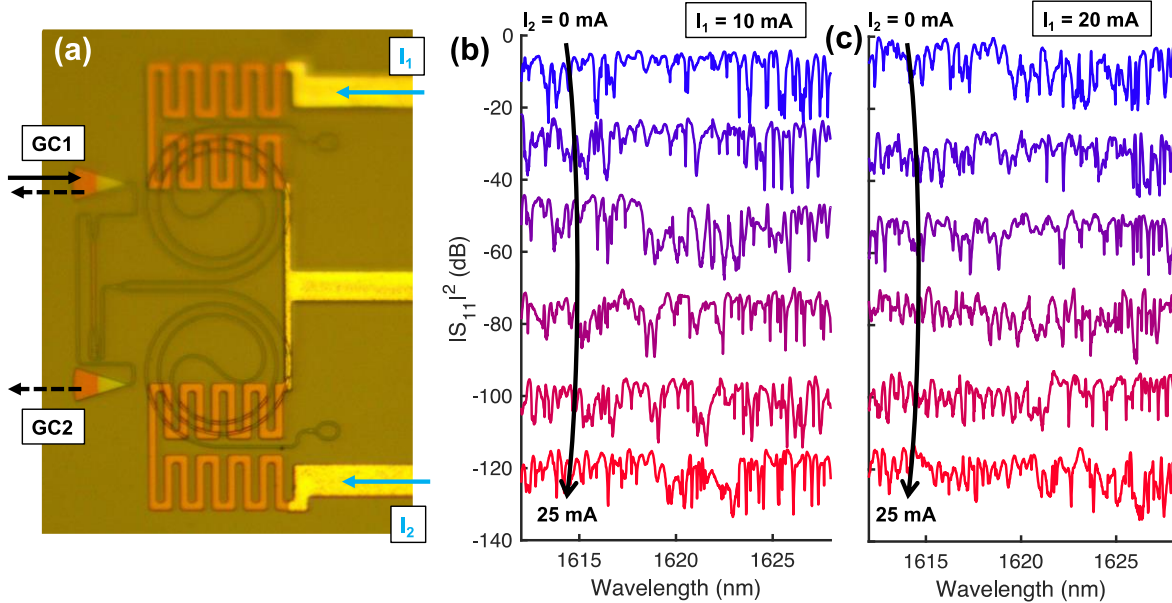


Fig. 5.1. (a) Microscope image of a silicon photonic moiré quasicrystal interferometer (QCI) with two grating couplers (GC1/GC2) and two integrated Ti/W micro-heaters. [Right] Experimentally measured QCI spectra in response to tuning micro-heater  $I_2$  from 0 to 25 mA (5mA steps shown) while: (b)  $I_1 = 10$  mA, and (c)  $I_1 = 20$  mA

tungsten (Ti/W) as the heating element; an established technique that allows the construction of active thermo-optic devices such as phase shifters and active filters/switches [3]. These devices contain two layers of metal, titanium-tungsten (Ti/W) and Aluminum. The final layer is an oxide passivation layer that is used to protect the heaters from damage due to oxidation effects.

In the device depicted in Fig. 5.1(a) we intentionally offset the micro-heaters from the center of each quasicrystal waveguide spiral. This offset produces a thermal gradient and non-uniform heating of each arm of the QCI, which is expected to aid in preserving the complexity and uniqueness of the output spectral signature.

#### 5.4 Instrumentation and Measurement Technique

We employed reflection mode grating coupler measurement to characterize the active PUFs. Fig. 5.1(a) shows a microscopic image of a QCI PUF with two integrated micro-heaters. Devices were characterized by measuring the reflectance spectra, or  $|S_{11}|^2$ , for TE polarized light coupled to GC1 depicted in Fig. 5.1(a). Fig. 5.2 portrays complete instrumentation diagram with microscopic image of electrical connections. A tunable laser source (Santec TSL-510) is used to provide steady wavelength sweeps from a fixed range: 1560nm to 1680nm across the grating coupler. Light is transmitted from the source through a single mode optical fiber to the polarization controller which is connected to an optical circulator. The grating couplers here are designed for TE polarization. The circulator consists of a single input fiber and two output fibers. The first output fiber is directly connected to the fiber focuser which shines the infrared light into the grating couplers of the PUF while simultaneously accepting the reflection power. The reflection power captured from the fiber focuser transmits back into the circulator and exits the second output fiber. The second output fiber is attached to a power detector which digitizes the reflection signal received from the PUF. Electrical probes attached to the dual channel current source (Keithley 2602B) were delicately

placed on aluminum electrical contacts connected to the heaters to facilitate electrothermal tuning of the QCI.

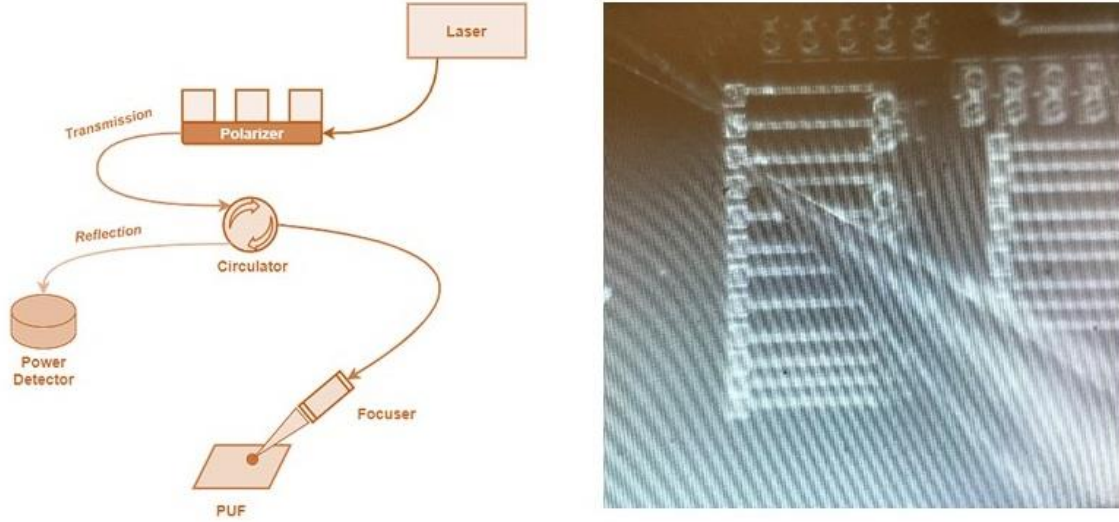


Fig. 5.2. Instrumentation diagram. (Left) Tunable semiconductor laser connected to a polarization controller, optical circulator, fiber focuser, and power meter. (Right) Image of electrical probes contacting electrical pads to the PUF

Precise focuser alignment on the PUF is a critical component of the measuring process. The focuser tip was placed at a  $27^\circ$  angle, determined by the following phase matching condition for grating coupling from free-space to on-chip where the waveguide is characterized to have an effective index,  $n_{eff}$ , and the grating couplers have a grating period,  $P$ .

$$\lambda = P(\sin\theta + n_{eff})$$

To test the PUFs, a series of wavelength sweeps were performed with the source meter conducting 0 to 30 mA current. A visible periodicity is observed from the output plots of both arms of each PUF which is shown in Fig. 5.1(b) and 1(c). As we increase the current, the resistive heater increases the temperature of the neighboring waveguides. Silicon's refractive index increases at a rate  $\frac{dn}{dT}$  of approximately  $1.8 \times 10^{-4}$  refractive index units (RIU) per  $^\circ\text{C}$ . The average phase variation acquired in the arm (due to resonance) is equal to:

$$\Delta\Phi = \frac{2\pi}{\lambda} * dn * (2L)$$

where,  $\Delta\Phi$  is average phase variation of one arm and L is the length of the arm.

## 5.5 Results and Analysis

As temperature and thermo-optic index change increases,  $\Delta\Phi_1$  will eventually approximate to  $\pi$  (destructive interference with the opposite arm where  $\Delta\Phi_2 = 0$ ). However, with continuous heating,  $\Delta\Phi_1$  being  $2\pi$ , it becomes constructive with the opposite arm since  $2\pi = 0$  and this repeats through  $3\pi, 4\pi, 5\pi, \dots$  yielding to the cyclical nature of the periodicity of the output structure. For example, in Fig. 5.1(b) and 5.1(c), the 10mA plot retained the general spectrum of the passive PUF output, particularly in the range: 1610-1630nm. However, once 20mA is applied, the curve is almost completely consolidated. A linear trend would expect similar results for the 30mA plot but instead, the original curvature in the spectrum is beginning to reappear.

Device measurements confirmed the presence of a unique, fingerprint like, and reconfigurable optical spectrum for each device tested. Experimental results corresponding to the device depicted in Fig. 5.1(a) are reported Fig. 5.1(b,c). Here we show reconfiguration of the device spectra using the micro-heater current delivered via either I1 and/or I2. For the 5 mA steps depicted in Fig. 5.1(b,c), each spectrum is visibly uncorrelated. Using the above-mentioned two-channel current source, current is swept from 0 mA to 30 mA with 1 mA step size at one channel while the other is fixed at a certain value. Sample measured spectra are displayed in Fig. 5.3. Note that, the similar technique used in Chapter 4 is also used to analyze the data in this section. Here, feature for every current value works as a distinct PUF similar to the 56 PUFs we studied in the previous chapter. Better correlation results for 0.2 mA finer sweeps at 15 mA to 20 mA currents, and way more

significant correlation data for 0.1 mA step size at 9 mA to 11 mA currents. The correlation results are illustrated in Fig. 5.4.

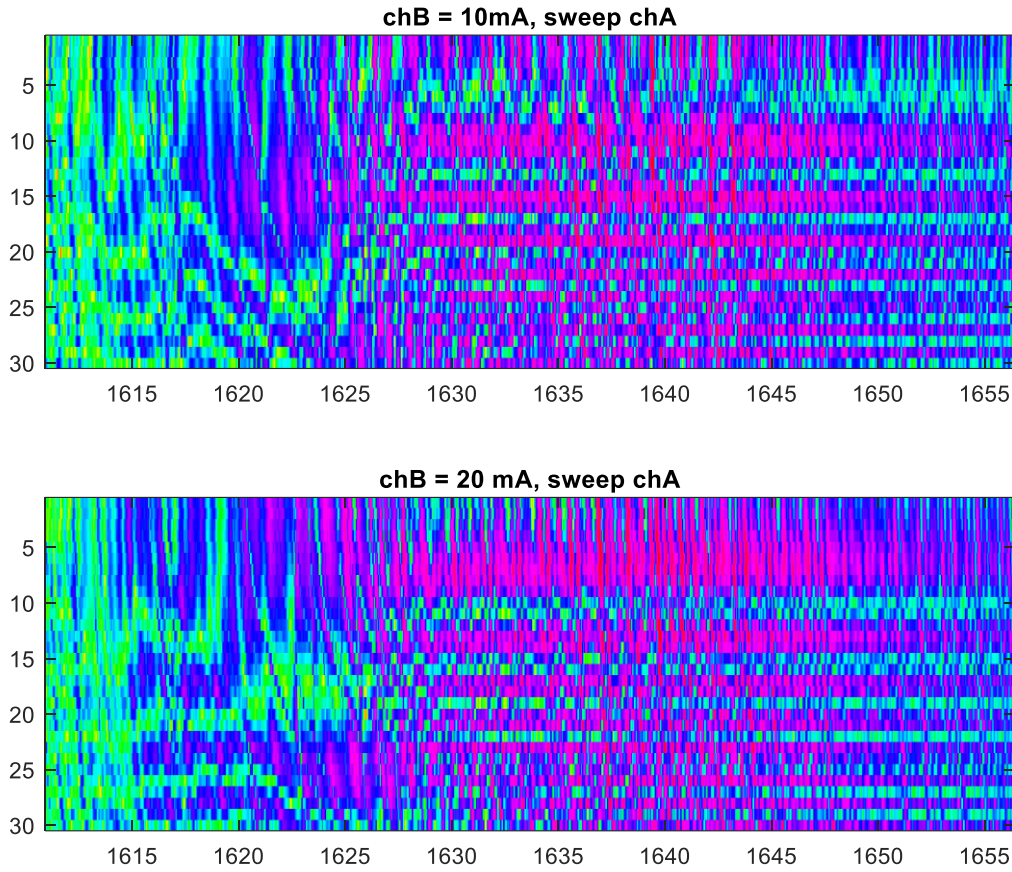


Fig. 5.3. Measured device spectra. (Top) Channel B is fixed at 10 mA, Channel A is swept from 0 mA to 30 mA. (Bottom) Channel B is fixed at 20 mA, Channel A is swept from 0 mA to 30 mA

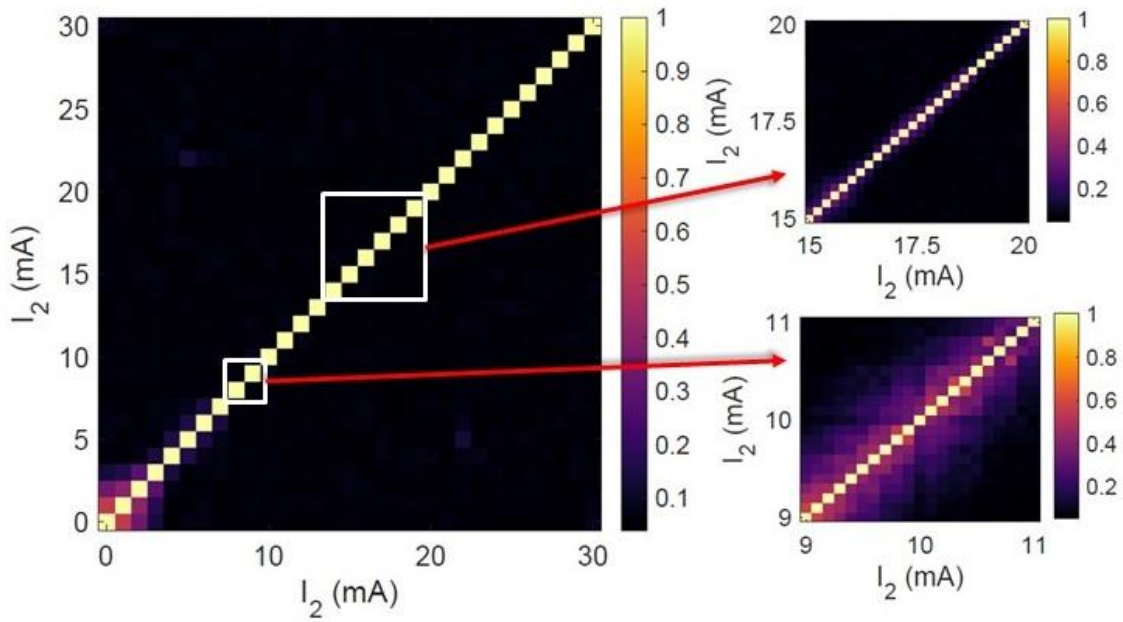


Fig. 5.4. Correlation analysis results of the electrically reconfigurable PUFs for 1 mA (left), 0.2 mA (top right) and 0.1 mA (bottom right) sweeps

Moreover, as stated above, a visible periodicity is observed in the optical spectra at both arms of each PUF (Fig. 5.5), thus confirming the electrically reconfigurable nature of the device. Whereas the optical signature of our prior passive PUF may provide a cryptographic key roughly ten thousand bits in length, active reconfiguration of the device demonstrably enhances the key length. Conservatively estimating the number of reconfigurable states to 100, results in a more than two order of magnitude enhancement to the size of the PUF's unique key, corresponding to an information density on the order of  $\sim 5$  GB/in<sup>2</sup>.

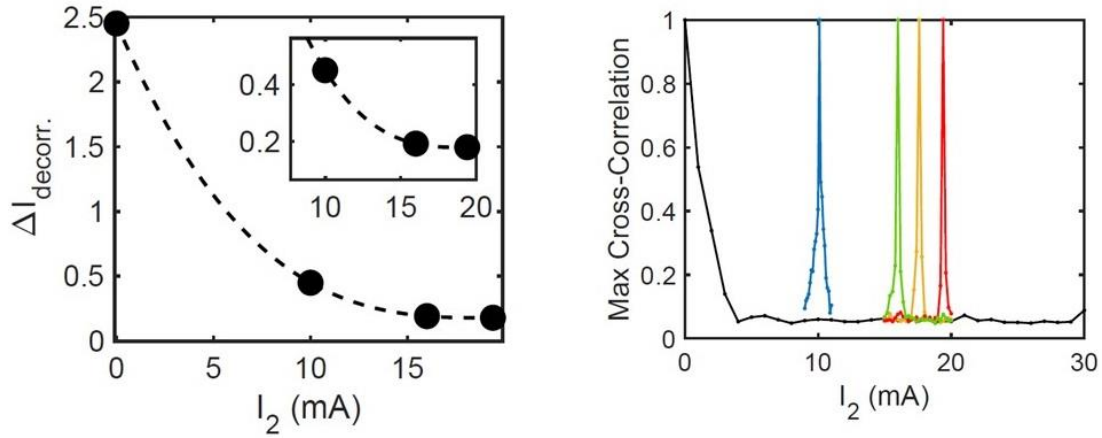


Fig. 5.5. Optical spectra at both arms of each PUF: confirms visible periodicity, yielding to electrically reconfigurable nature of QCI PUF

## 5.6 Outlook

The active version of the QCI PUF has already shown promising nature as demonstrated in this chapter. However, there are a plenty of scopes to explore other parameters that can be used to strengthen the active PUF's overall effectiveness. The benefit of QCI PUF is its robustness against external factors such as optical angular/spatial alignment and polarization. However, these factors remain a large influence on the output of the current PUF. Additional future work revolves around improving the QCI structure and expanding its ability to probe disorder. The standard QCI design has a signature spiral structure and adding additional loops or perhaps additional spirals beyond the two already present could alter the output significantly. Replacing the fiber focuser with a fiber array will allow for multiple fibers to be pointed at the PUF simultaneously. Thus, the fiber that transmits the laser can now be separate from the one that absorbs the reflection power. Lastly, upon improving the PUF and increasing robustness against external factors, power loss is a persistent limitation to which these devices can function properly. Disorder due to fabrication errors are proportional to the amount of loss experienced and devising methods of minimizing loss while increasing disorder is a critical component of impending work in the field.



We presented the preliminary version of this work at Conference on Laser and Electro-Optics in 2022 [4]. In the future, we anticipate compact photonic PUF structures exploiting additional stimuli and/or degrees of freedom (e.g. polarization, mode, nonlinear effects) can increase this information density to  $>10$  TB/in<sup>2</sup>, thus fostering even greater security and reliability.

## References

1. Bin Tarik, F.; Famili, A.; Lao, Y.; Ryckman, J. D. Robust Optical Physical Unclonable Function Using Disordered Photonic Integrated Circuits. *Nanophotonics* 2020, 9 (9), 2817–2828. <https://doi.org/https://doi.org/10.1515/nanoph-2020-0049>
2. Aubry, S.; Andre, G. Analyticity Breaking and Anderson Localization in Incommensurate Lattices. *Ann. Isr. Phys. Soc.* 1980, 3, 133–140
3. NanoSOI Fabrication Service: Applied Nanotools Inc. Applied Nanotools Inc. | X-Ray Optics and Integrated Photonics. (2022, June 22). <https://www.appliednt.com/nanosoi-fabrication-service/#1515088441507-05b0d74f-11d79b1b-5b54>
4. Bin Tarik, F.; Joyce Jr., D.; Lao, Y.; and Ryckman, J. D. Electronically reconfigurable photonic PUF based on a moiré quasicrystal interferometer. Conference on Laser and Electro-Optics (2022)

## SUMMARY AND OUTLOOK

Silicon offers us immense possibilities and allows us to perform all of the key optical functions at a reasonably competitive performance level. Electronic-photonic circuits will play a ubiquitous role globally and silicon photonics is going to the heart of it. As they keep on impacting such areas as high-speed communications for mobile devices (smartphones, tablets), optical communications within computers and within data centers, sensor systems, medical applications etc, attaining hardware and information security will always remain as a major concern. At the same time, coupling light between the chip and optical fibers, and achieving this in a packaging method that is cost effective, is still one of the long-lasting hindrances of silicon photonics. This work addresses two of the big issues of this foundries and provides feasible solutions through subwavelength engineering of silicon photonic waveguides.

In this dissertation, we demonstrated evanescent coupling technique to access the ultra-low mode area of a novel V-groove waveguide in both non-adiabatic directional coupling and adiabatic mode evolution configurations. We achieved >99% coupling efficiency through adiabatic mode evolution that too within a broadband region. We developed fabrication recipe for all-dielectric subwavelength novel structures in terms of v-groove and diabolos and experimentally verified waveguiding phenomenon of v-groove waveguide. This could turn out to be a breakthrough innovation as it will open so many new directions and dimensions of enhancing light matter interactions.

We expect many of the design principles utilized here can equally apply to other types of waveguide systems, particularly those which interface between conventional modes and dissimilar modes or those exhibiting strong sub-diffraction character. One such concept is optical anapoles due to its rich physics in a diabolo type shape. Beyond our primary objective, we have fabricated and characterized anapole supporting sub-wavelength engineered all-dielectric silicon nanodisk structures. Measurements were taken in both visible and near infrared region using reflection spectroscopy.

Optical anapole has become a subject of growing interest due to its intriguing physics and prospective applications. The anapole state emerges at a certain frequency where the fields radiated by the co-located electric and toroidal dipoles cancel each other in the far-field through destructive interference in a special type of Fano resonance [1]. It has been reported that the field enhancement is maximized not necessarily at the anapole frequency, but rather in its vicinity at the frequency corresponding to the higher quality factor mode contributing to the Fano resonance [2]. Previously, anapole states have been implemented in low-aspect ratio nanodisks where the disk height might be on the order of  $\sim 50\text{-}100$  nm. Slotted nanodisks supporting anapole modes have also been proposed as a means to locally enhance the electric field in the slotted region by a factor  $\epsilon h/\epsilon l$ , where  $\epsilon h$  and  $\epsilon l$  are the permittivity values for the high and low index materials respectively. There it was predicted that the incident electric field  $E_0$  could be enhanced by a factor on the order of  $\sim 10^3$  within the slot region of a single high index nanodisk [3].

We theoretically and experimentally characterize our anapole supporting sub-wavelength engineered all-dielectric silicon nanodisk structure. Devices are fabricated using electron beam lithography in a 220 nm silicon on insulator (SOI) wafer – a platform common to silicon photonics technology. For this device thickness, a nanodisk radius on the order of  $\sim 200\text{-}300$  nm alongside etched square dimensions on the order of  $\sim 100$  nm x  $100$  nm are predicted to place the anapole

mode in the near infra-red region. For this geometry, simulations predict the presence of a resonant anapole like mode with perfect extinction (zero reflectance) and very large field enhancement,  $\sim 104$ , near  $\sim 1070$  nm as depicted in Fig. 6.1(c & d).

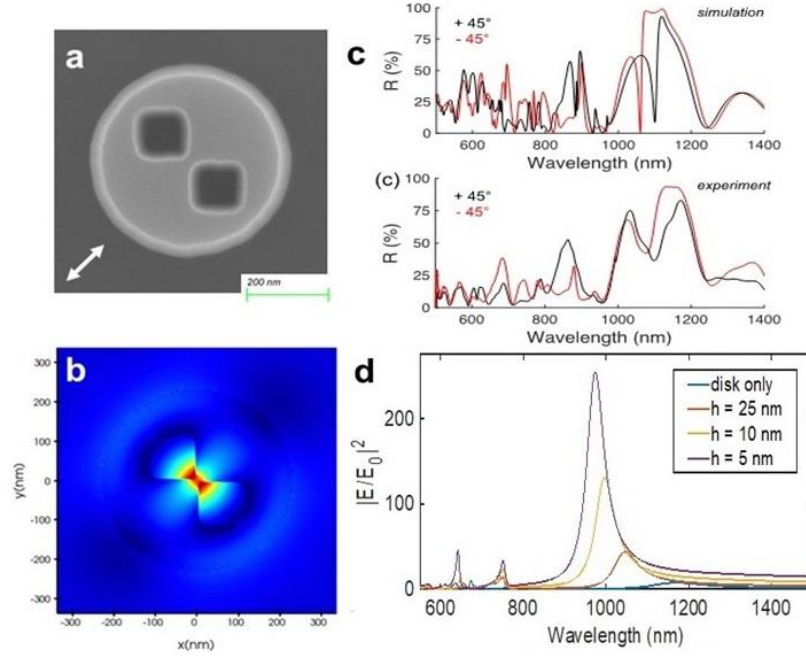


Fig. 6.1. (a) SEM image of a typical fabricated sub-wavelength engineered silicon nanodisk (top view). (b) Electrical field profile of the resonant nanodisk. (c) Simulated and measured reflection spectra by the nanodisk arrays at normal incidence. The resonance is visible at  $\sim 1074$  nm wavelength. (d) Corresponding enhancement of the incident electric field  $E_0$  as measured in silicon at the center of the nanodisk with different disk heights

To characterize our structure and verify the presence of the resonant mode, we performed polarization resolved reflectance measurements in an optical microscope ( $NA = 0.4$ ) using visible and near-infrared spectrometers (OceanOptics). The experimental spectra obtained for a  $45^\circ$  polarizer angle show good overall agreement with the device simulation. We also performed experiments on devices where specific design parameters such as  $d$ , the square dimensions, and  $P$  are systematically skewed (not shown), to further map the characteristics of this geometry. The placement of the resonant frequency makes this structure especially attractive for probing the

strongly enhanced light-matter interactions via Raman scattering at  $\sim 1064$  nm. Alternative designs can also achieve high order anapole states with similar properties in the visible region.

Our results suggest this structure is an excellent platform for tailoring light-matter interactions in silicon or other high index media, and for harnessing anapole physics in the visible and infrared regions. Primary work on this topic was presented in Conference on Laser and Electro-Optics in 2021 [4]. More progress on this topic is currently being made by the members of Ryckman group.

We also established a proof-of-concept physical unclonable function from silicon photonic moiré quasicrystal interferometers. We verified its unclonability and immunity towards environmental variations. We characterized 56 identically designed QCI PUFs and proved their scalability, CMOS compatibility and suitability for secure hardware authentication. This work represents, to our knowledge, the largest experimental sample size of physically distinct photonic-PUFs reported to date. Moreover, we took one step further from the passive PUF structures towards electrically reconfigurable active QCI PUFs. Motivated by cryptographic applications seeking enhanced reliability and/or security, we experimentally validated physically unclonable photonic circuits based on active moiré quasicrystal interferometers with integrated micro-heaters.

We addressed the issues related to conventional digital fingerprint techniques and provided our solution by means of QCI PUF with significant verification of authentication. The architecture is wafer scale compatible and can be characterized with automated probing equipment, which is now a mature technique in silicon photonics and packaging industry. The unique traits of these devices originate from their lack of translational symmetry and an optical design which ensures high sensitivity toward natural nanoscale fabrication imperfections. This could enable chip IDs that inherently tag the lot, wafer, die information with unclonable fingerprint. Envisioning related types of active or passive silicon photonic structures, can be scalably employed in active or quantum

readout schemes to facilitate applications such as anti-counterfitting tag, remote authentication and secure communication. Future direction of this work can be exploring various interferometric configurations, such as, Mach-Zehnder interferometer configuration, to achieve silicon photonic physical unclonable function. Moreover, adding more reconfigurable states should reduce the size of the device while increasing information density to a large extent. More complex and multiplexed challenge-response system can be added and analyzed while transforming the QCI PUF to a silicon photonic quantum PUF.

Silicon photonics is set to be the next big thing in the realm of science and innovation. And silicon waveguide is the core building block of modern integrated photonic system. Subwavelength engineering of silicon photonic waveguides opens new doors of research and development. Therefore, prospects of this sector cannot be valued any less at the moment. In this dissertation, we tried to focus on two crucial avenues of this spectacular field of study to improve human lives. With the ever-accelerating technological advancement, we expect our research will give mankind speed, security and reliability. These results illustrate a clear path to efficiently interfacing with novel types of all-dielectric sub-diffraction waveguides, thus making them accessible in future experimental works that seek to harness their strong subwavelength field enhancement.

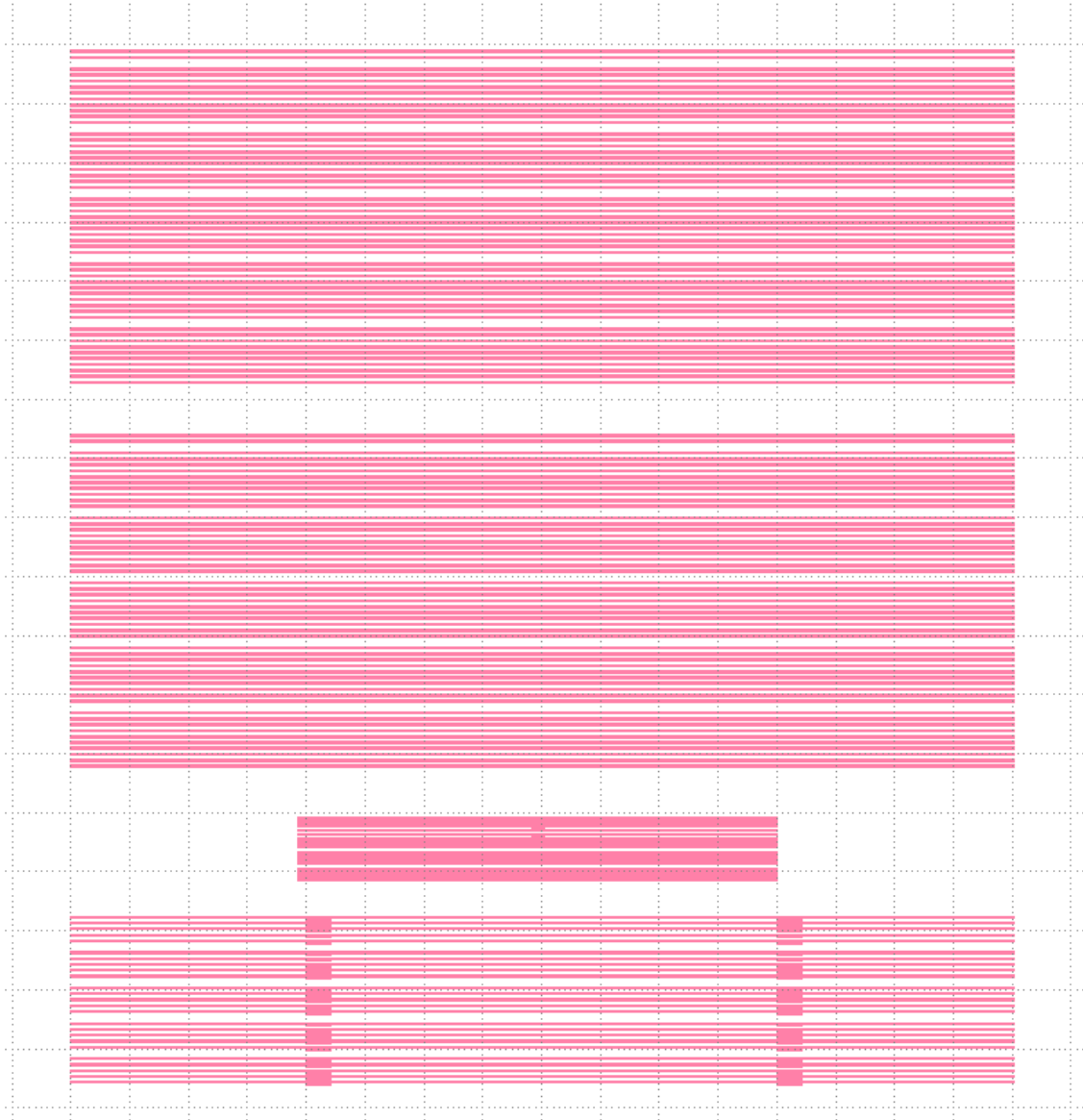
## References

1. Miroshnichenko, A. E., Evlyukhin, A. B., Yu, Y. F., Bakker, R. M., Chipouline, A., Kuznetsov, A. I., Luk'yanchuk, B., Chichkov, B. N., and Kivshar, Y. S. "Nonradiating Anapole Modes in Dielectric Nanoparticles," *Nat. Commun.* 6, 1–8 (2015).
2. Colom, R., McPhedran, R., Stout, B., and Bonod, N. "Modal Analysis of Anapoles, Internal Fields, and Fano Resonances in Dielectric Particles," *J. Opt. Soc. Am. B* 36, 2052 (2019).

3. Yang, Y., Zenin, V. A., and Bozhevolnyi, S. I. "Anapole-Assisted Strong Field Enhancement in Individual All-Dielectric Nanostructures," ACS Photonics acsphotronics.7b01440 (2018).
4. Farhan Bin Tarik, Saddam Gafsi, Cody T. Nelson and Judson D. Ryckman, "Localized field enhancements and anapoles in subwavelength-engineered silicon nanodisks," Conference on Laser and Electro-Optics (2021).

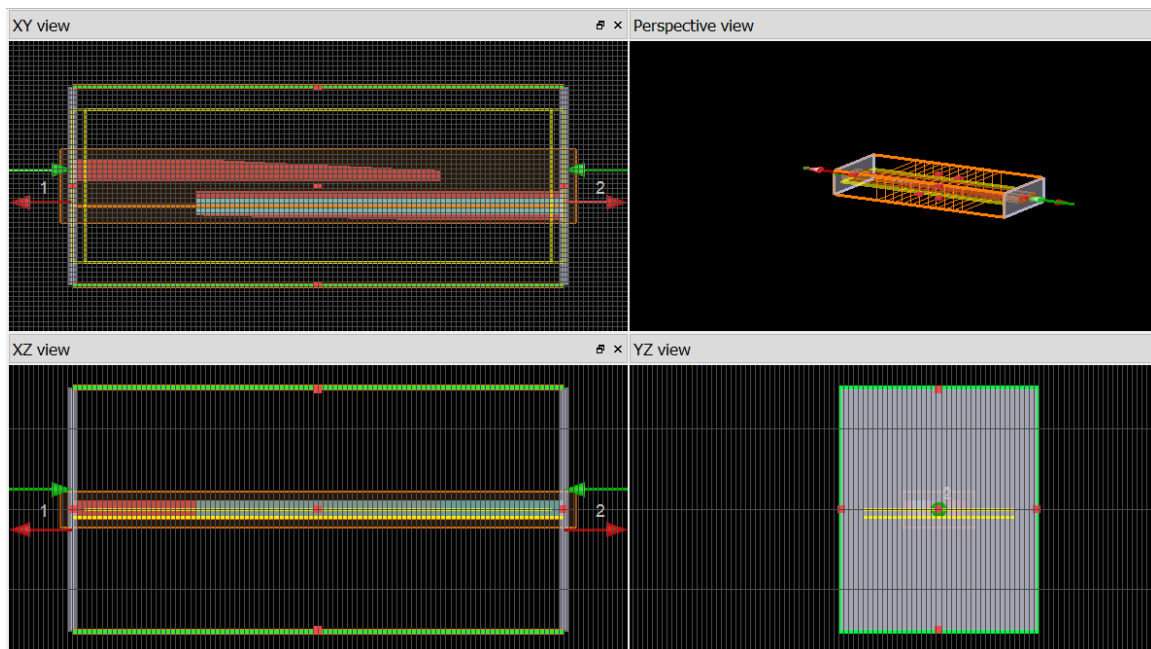
## APPENDIX A: V-GROOVE DESIGN AND MODELLING

### A.1 Mask Design of V-groove Waveguide in K-Layout



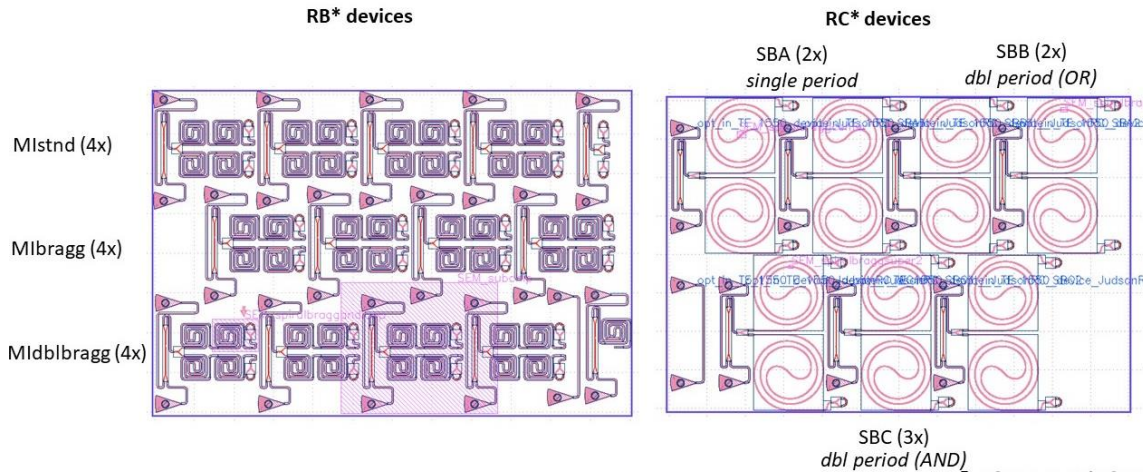


## A.2 Sample Lumerical Design of V-groove Adiabatic Coupler

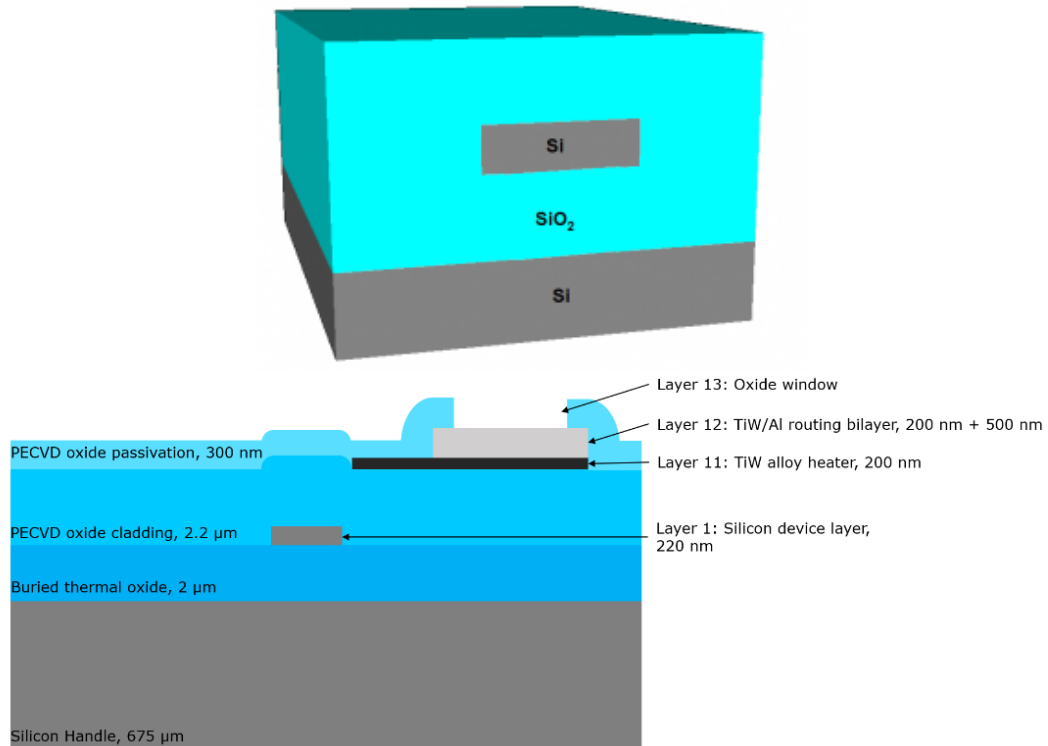


## APPENDIX B: QCI PUF DESIGN

### B.1 Design Overview of Silicon Photonic QCI PUF



### B.2 Tri-Layer Metallization Process to Fabrication Micro-Heaters on Silicon Platform



*The End*